AFRPL-TR-79-60

Plume Characterization of a One-Millipound Solid Teflon Pulsed Plasma Thruster

L. K. Rudolph
K. G. Harstad
L. C. Pless
R. M. Jones

Prepared by

Jet Propulsion Laboratory
California Institute of Technology
Pasadena, California
(JPL PUBLICATION 79-105)

September 1979

Phase II Final Report

Approved for Public Release
Distribution Unlimited

Prepared for:

Air Force Rocket Propulsion Laboratory
Director of Science and Technology
Air Force Systems Command
Edwards AFB, CA 93523

TABLE OF CONTENTS

LIST OF ILLUSTRATIONS

LIST OF TABLES

1.0 INTRODUCTION

Pulsed plasma thrusters (PPT) using solid teflon propellant have a flight demonstrated simplicity and reliability,[1] and are of increasing interest for future flight applications. Earlier versions of these thrusters had total impulses of less than 3000 lb-sec and impulse bits of less than 100 μlb-sec, and hence, were limited to applications such as east-west stationkeeping and fine attitude control of small spacecraft.[2] A one-millipound average thrust PPT is currently under development to extend the capabilities of the pulsed plasma thruster to applications on larger spacecraft with longer mission duration.[3] This thruster has an impulse bit roughly 50 times larger, and a total impulse roughly 10 times larger, than the earlier versions. In addition, its specific impulse, propellant flow rate, efficiency and power are also significantly higher. Envisioned applications for this millipound thruster include north-south stationkeeping, satellite orbit acquisition and maneuvering, and large structure attitude control.

The flight experience of the smaller pulsed plasma thrusters has shown that the exhaust plume of these thrusters has a negligible effect on spacecraft surfaces.[4] The exhaust plume of the one-millipound thruster is of potentially greater concern, primarily due to its higher energy and mass. In addition, longer duration missions with ever more sensitive instrumentation will aggravate any plume contamination problem that may exist. Previous studies[5] have been conducted to assess the effect of the one-millipound PPT plume on spacecraft surfaces by directly measuring the plume flux towards a spacecraft upstream of

the thruster exhaust plane. Unfortunately, accurate results have been masked by a backscattered flux of particles reflected and eroded from the test facility vacuum chamber walls. In order to minimize this effect and to develop a more accurate measure of the plume-spacecraft interaction, a study was carried out at the Jet Propulsion Laboratory using the Molecular Sink Vacuum Facility (MOLSINK). This facility has a gaseous helium cooled anechoic-type liner (MOLTRAP) especially designed to minimize any plume-wall backscatter, thus providing an environment in which accurate plume-spacecraft interaction measurements may be made.

The JPL plume study has been divided into two phases:

Phase I: An evaluation of the PPT plume-wall backscatter characteristics of the MOLSINK facility, a conceptual design for a PPT backflow measurement technique, and the development of a low temperature quartz crystal microbalance (QCM) design to be used in measuring this backflow.

Phase II: A study of the plume-spacecraft interaction utilizing the MOLSINK facility, including a direct measurement of the plume backflow mass flux into the thruster nozzle exit plane at various distances from the thruster axis and a measure of the PPT primary plume mass flux profile downstream of the thruster nozzle.

The experiments and analyses of Phase I have been completed and are detailed in a previous report.[6] Included is a description of the MOLSINK facility as modified for use with the pulsed plasma thruster, and of the Solar Electric Propulsion (SEP) vacuum facility, used for the PPT primary plume studies and

preliminary QCM testing. The QCM circuit design and calibration at liquid nitrogen temperatures is also discussed. Backscatter from the MOLTRAP anechoic surface was measured in total, and at two specific locations, using QCM test arrays designed for this purpose. The results indicate that the plume wall backscatter is highest at the wall areas closest to the thruster axis and falls to negligible values at the plume boundary-wall intersection, ~ 40° off this axis. The total backscatter from the entire MOLTRAP wall area was found to be almost 5% of the PPT plume mass. Based on these wall backscatter measurements, a conceptual method was developed for measuring the PPT plume backflow. Because of the relatively large plume-wall backscatter in the MOLSINK over the wall area directly in the PPT primary plume, an indirect method of measuring the backflow is required which avoids measuring the wall backscatter. Figure 1 shows the conceptual technique, which uses a collimated QCM to make the plume backflow measurement. This collimated QCM is rotated around a fixed point at the entrance to the collimator. The collimator aperture "dip" angle is finite, therefore the QCM signal originates from a small segment of the PPT plume and a segment of the MOLTRAP wall. The insert in Figure 1 indicates the kind of data expected from such a measurement. The greatest backflow would be expected at a dip angle of 0° - decreasing to lower values in the downstream direction. Once the view angle begins to intercept the plume boundary-wall intersection, the wall backscatter will begin to dominate the signal. By considering only the data for small dip angles, the net total plume backflow can be calculated by summing the data over the dip angle distribution. Using a collimator with a conical aperture as shown in Figure 2 would require observations over various

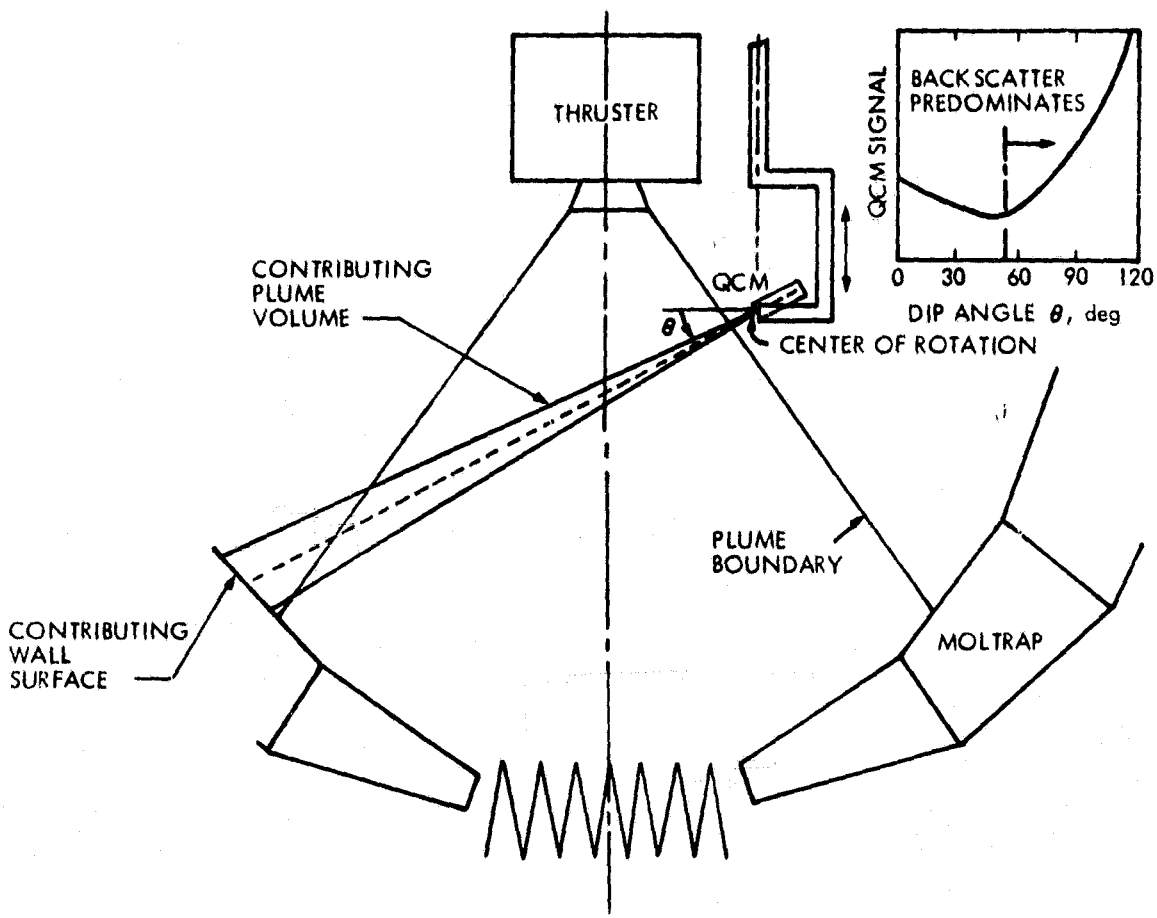

Figure 1. Backflow Measuring Technique

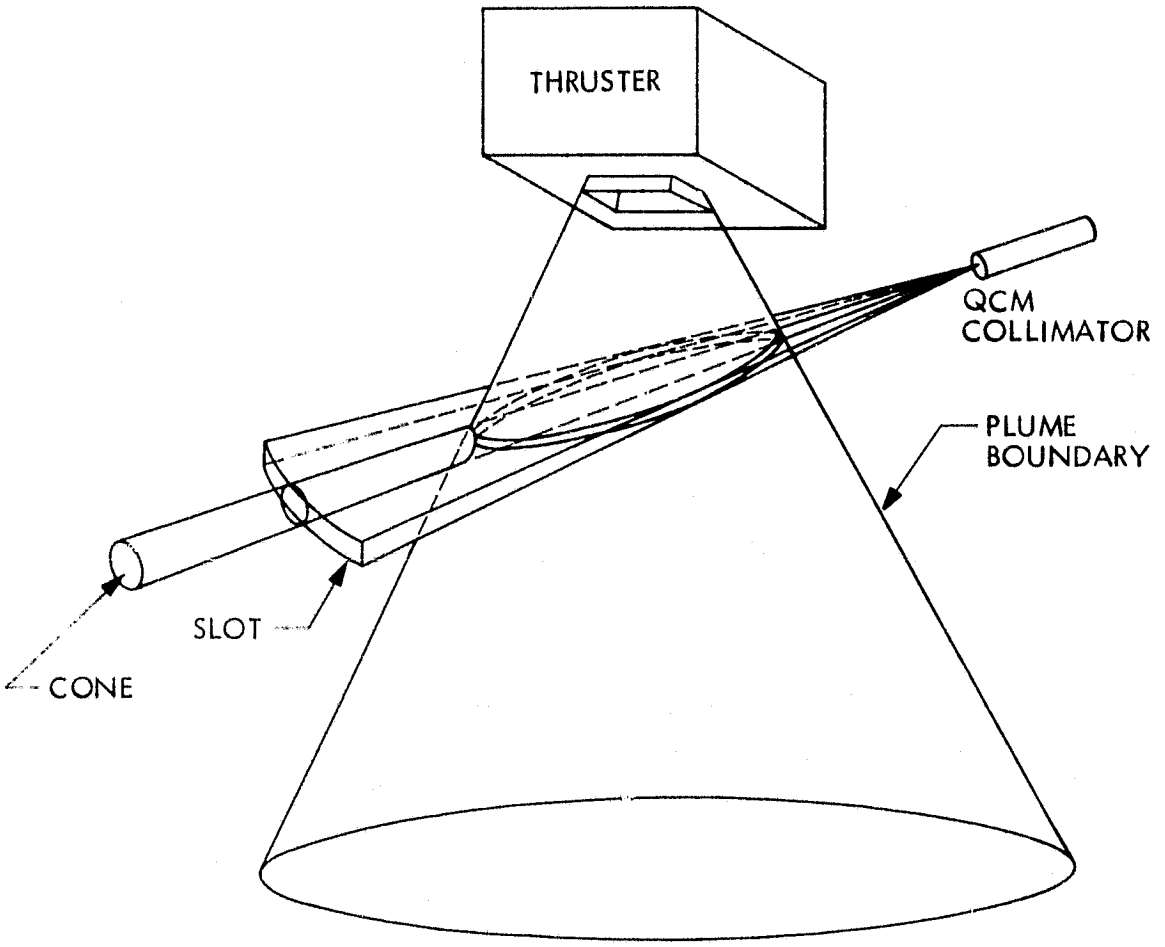

Figure 2. Collimator Apertures

dip angles both parallel and perpendicular to the thruster axis in order to observe the entire plume volume. To avoid the experimental complexity associated with such an aperture, a slotted aperture was chosen for the collimator design, as also shown in Figure 2.

Building upon the previous Phase I efforts, the Phase II investigations of the PPT primary plume and plume backflow have been completed, and are detailed in this report. A discussion of the primary plume measurements and their impact on the plume backflow testing is followed by a description of the design of the QCM backflow test apparatus. After these sections, the collimated QCM measurements taken in the MOLSINK facility are described and used in a detailed analysis of the PPT plume backflow level and distribution. Finally, an additional section is included which describes a small follow-on measurement of the plume backflow from the PPT with a radically modified nozzle geometry, to determine the backflow sensitivity to nozzle design.

2.0 PRIMARY PLUME STUDIES

The source of the backflow from the pulsed plasma thruster is the primary plume downstream of the thruster nozzle. The backflow mass flux magnitude and its distribution away from and around the thruster axis both depend on the primary plume mass flux, velocity, and chemical structure. In order to develop an accurate picture of the PPT backflow, and, more practically, to assist in the design of an acceptable backflow measurement technique, a basic understanding of these characteristics of the PPT primary plume is necessary. To develop this understanding, various tests have been carried out and are described in the following paragraphs. The major fraction of these tests was performed in the SEP vacuum facility due to its greater operating convenience and lower cost.[6] The remaining tests require a thruster environment more similar to actual space flight conditions, and, hence, were performed in the MOLSINK facility.[6,7]

2.1 Mylar Target Deposition The exit orifice of the PPT exhaust nozzle is a 11.5 by 16.5 cm rectangle with a resulting aspect ratio of 1.4. This azimuthally nonsymmetric shape implies that the exhaust plume, and hence the plume backflow, may also be non-axisymmetric around the thruster axis. In addition, any plume-wall backscatter would be non-axisymmetric. This would require any primary or backflow plume measurement to be made at various azimuthal as well as radial and axial locations, and, thus, would considerably complicate the experimental testing. Recent observations at the Fairchild Republic Co.[8] indicate that 40 cm downstream of the nozzle exit plane, the PPT plume is elliptical in cross-section with its major axis parallel to the nozzle longer dimension, and with an aspect ratio of only 1.2. These results suggest that at greater downstream axial locations, the plume may approach azimuthal symmetry.

When installed in the MOLSINK facility for the plume backflow measurements, the PPT was placed approximately in the center of the enclosed volume so to

provide maximum thermal isolation from the MOLSINK walls.[6] In this position, the thruster plume will collide with the MOLSINK walls approximately 80 cm downstream of the PPT nozzle exit plane (assuming a plume expansion angle of about 40°[5]). To check the primary plume symmetry, and hence the plume-wall backscatter symmetry at this axial location, a technique developed for plume studies of the 8 cm ion bombardment thruster was used.[9] A 1.2 meter square sheet of 1 mil thick Mylar coated with a 700 Å thick layer of aluminum was placed 76 cm downstream of the PPT nozzle exit plane, on a frame supporting its top and bottom edges. A 38 cm diameter hole was cut in the center of this sheet to permit the central core of the PPT plume to escape without damaging the fragile Mylar. A photograph of this aluminized Mylar target is shown in Figure 3, as installed in the SEP vacuum facility prior to the test.

During the test, the target could be seen to oscillate after each thruster discharge due to the plume impingement. The target was exposed to approximately 12,000 discharge pulses over a three day period, and then removed from the tank for analysis. A photograph of the target after the test is shown in Figure 4. A series of concentric rings can be observed in this black and white reproduction which, in fact, are multicolored, in a manner similar to the bands of light seen in quarter-wave diffraction plates. Such plates consist of a highly reflective surface, such as aluminum, covered with a layer of transparent material with a thickness equal to an odd multiple of a quarter of a wavelength of the absorbed light. Thus, the presence of these concentric rings on the aluminized target indicates that material has been deposited.

The primary reason for performing the plume target test was to determine the azimuthal symmetry of the PPT plume, 70-80 cm downstream of the nozzle. The shape of the concentric rings seen on the plume target provides an accurate measure of this symmetry. The center of these rings is displaced upward

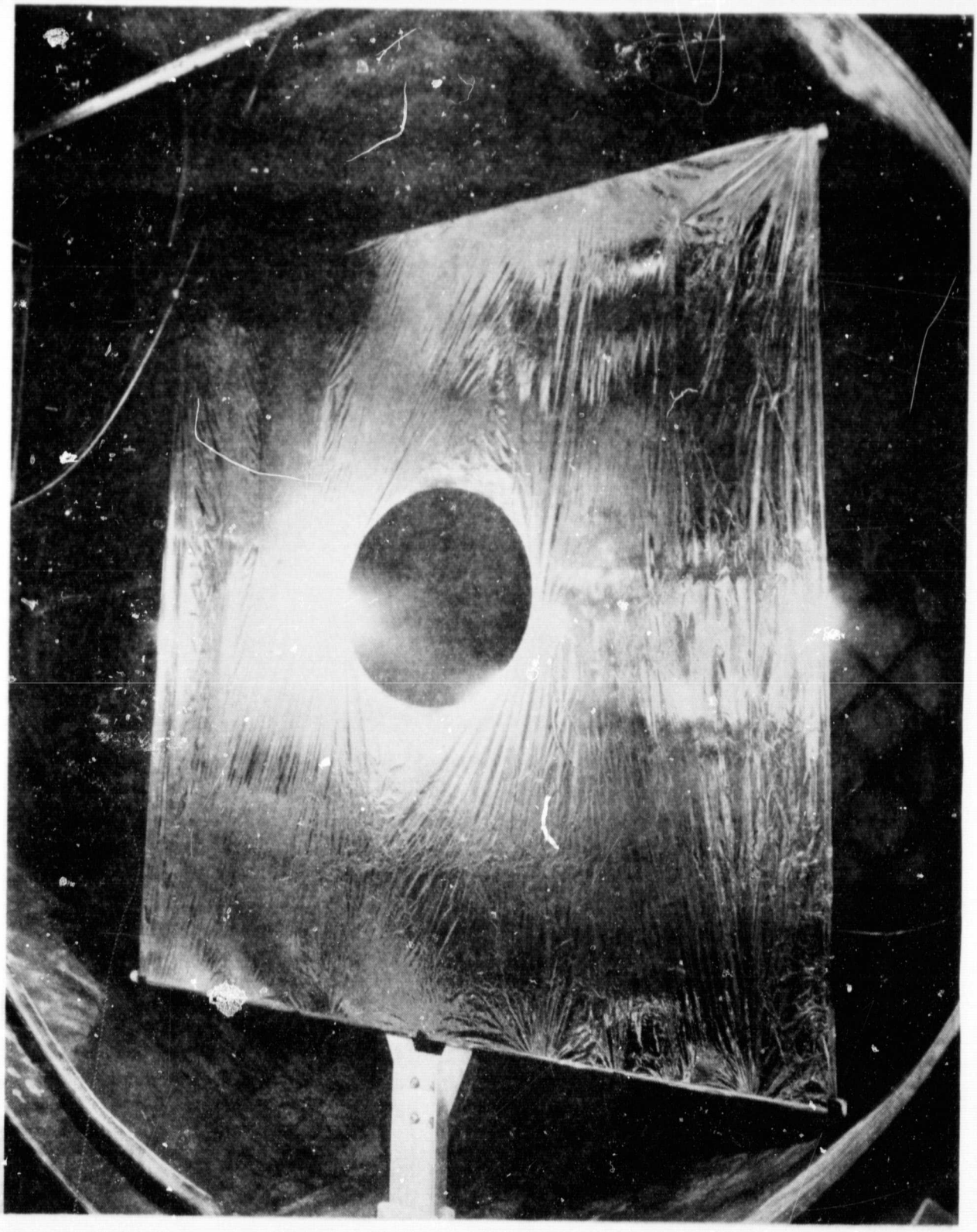

Figure 3. Aluminized Mylar Plume Target

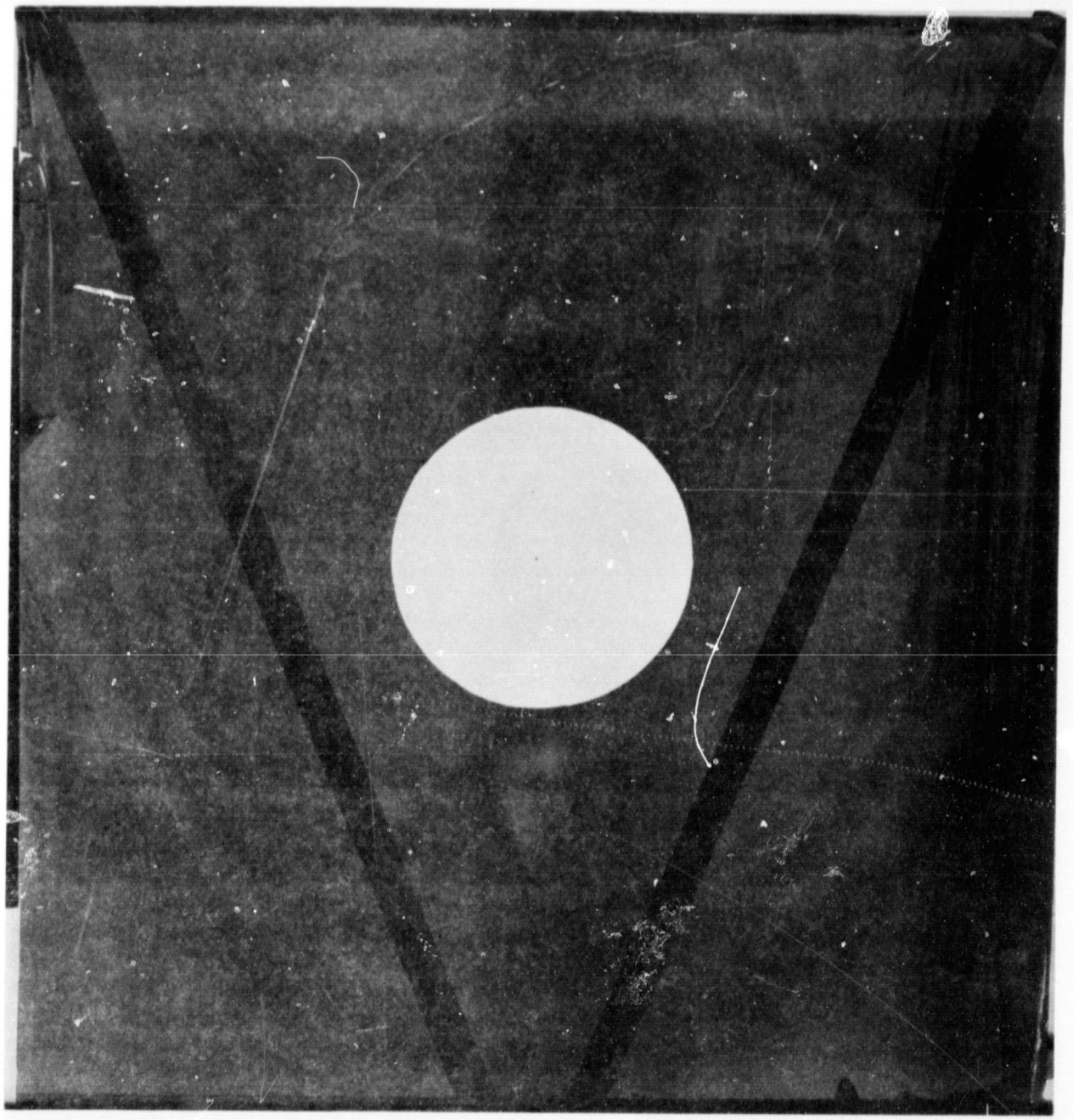

Figure 4. Plume Target Test Pattern

approximately 9 cm from the center of the plume target, indicating a slight misalignment in either the plume discharge or the thruster mounting. The concentric rings are circular, except for flat spots at the 10 o'clock and 2 o'clock positions. The top of the target (12 o'clock) corresponds to the location of the cathode electrode and the spark plug trigger; hence these flat spots may be associated with the difference between the cathode and the anode discharge physics. In any case, these flat spots represent a deviation from the circular ring mean radius of less than 5%; thus for practical purposes the primary plume can be taken to be azimuthally uniform. A further test to check the backflow plume axisymmetry is described in section 4.2 and confirms that the backflow is also azimuthally uniform.

In order to obtain more detailed information on the plume deposit, three different methods of measuring the actual thickness of the deposit on the plume target were attempted. The first method, utilizing a laser ellipsometer, failed due to the flexibility of the plume target Mylar substrate. This flexibility prevented the target from resting evenly on the sensing platform, which led to large inaccuracies. The second method utilized a Sloan DEKTAK Surface Profile Measuring System which senses the position of a scribe as it moves along the sample surface. This method was also unable to measure the absolute thickness of the deposition, again because of the flexibility of the Mylar substrate; however it did indicate that the existing micropores in the aluminum layer were smoothed over towards the target center. This could happen either by the deposit filling the micropores or by the plume eroding the surrounding aluminum. Finally, the transmittivity of the target was measured to see if any

qualitative evidence could be found to determine the deposit thickness. The transmission coefficient was found to drop from 2.7% at the outer edge of the target to 2.0% at the edge of the hole in the center of the target. This change in transmittivity is relatively small and indicates that either the deposit thickness increases towards the target center or that the target surface features change with decreasing radius to increase the reflectivity. In the light of the smoothed over micropores found with the surface profile measurement, it is more probable that the target surface features changed. None of the previous methods were able to determine the difference between erosion or deposition on the target, and hence, provide little improvement over the previous quarter wave plate analysis, in the understanding of the plume target results.

2.2 Double QCM Probe Mass Flux Previous investigators [5,10,11] have studied PPT plumes using such various diagnostics as Langmuir and B-field probes, calorimetric disks, high speed photography, glass capture caps, Faraday cups, microwave interferometry and single QCMs. When combined with the known performance of the PPT, these studies indicate that a significant fraction of the plume mass flux consists of low energy (probably neutral) particles. Thus, in order to measure the radial distribution of the PPT primary plume mass flux, a method is needed which is sensitive to both the neutral and ionized components of the plume. In addition, the method must provide adequate spatial resolution and an in situ, real time output to minimize error.

To satisfy the above requirements, a QCM measurement would seem to provide an adequate solution; however, as previously mentioned, earlier attempts [5]

to determine the radial distribution of the plume mass flux with a single QCM have met with little success because the plume erodes the QCM collecting surface rather than depositing on it. In order to alleviate this difficulty and still maintain the advantages of a QCM measurement, a special double QCM probe was developed, and is sketched in Figure 5. It consists of a shielded container with an aperture designed to direct the incoming mass flux to QCM 1, placed at an angle of 45° with respect to the incoming axis. The material which reflects or erodes from QCM 1 is partially captured by QCM 2, placed normal to the incoming axis and on the optical path from QCM 1.

The net signal output, S_1, of QCM 1, facing the PPT plume is equal to the rate of material deposited on the crystal sensor. This rate is equal to the axial component of the local plume mass flux, $\dot{m}$, less the amounts reflected and ablated, $\dot{m}_r$, from the QCM surface:

$$S_1 = \dot{m} \cos 45^\circ - \dot{m}_r \qquad (1)$$

The cos 45° is required to correct for the angle between the incoming axis and the QCM collecting surface normal. The reflected and ablated mass flux leaves the surface of QCM 1 in some unknown distribution about the QCM surface normal. Some fraction, K, of this mass flux impinges on and is collected by QCM 2. Thus, the signal output, S_2, of QCM 2 is:

$$S_2 = K\dot{m}_r \qquad (2)$$

The fraction, K, not only accounts for the fraction of reflected and ablated material from QCM 1 that impinges on QCM 2, but also for that fraction of impinging material that actually sticks to the collecting surface of QCM 2,

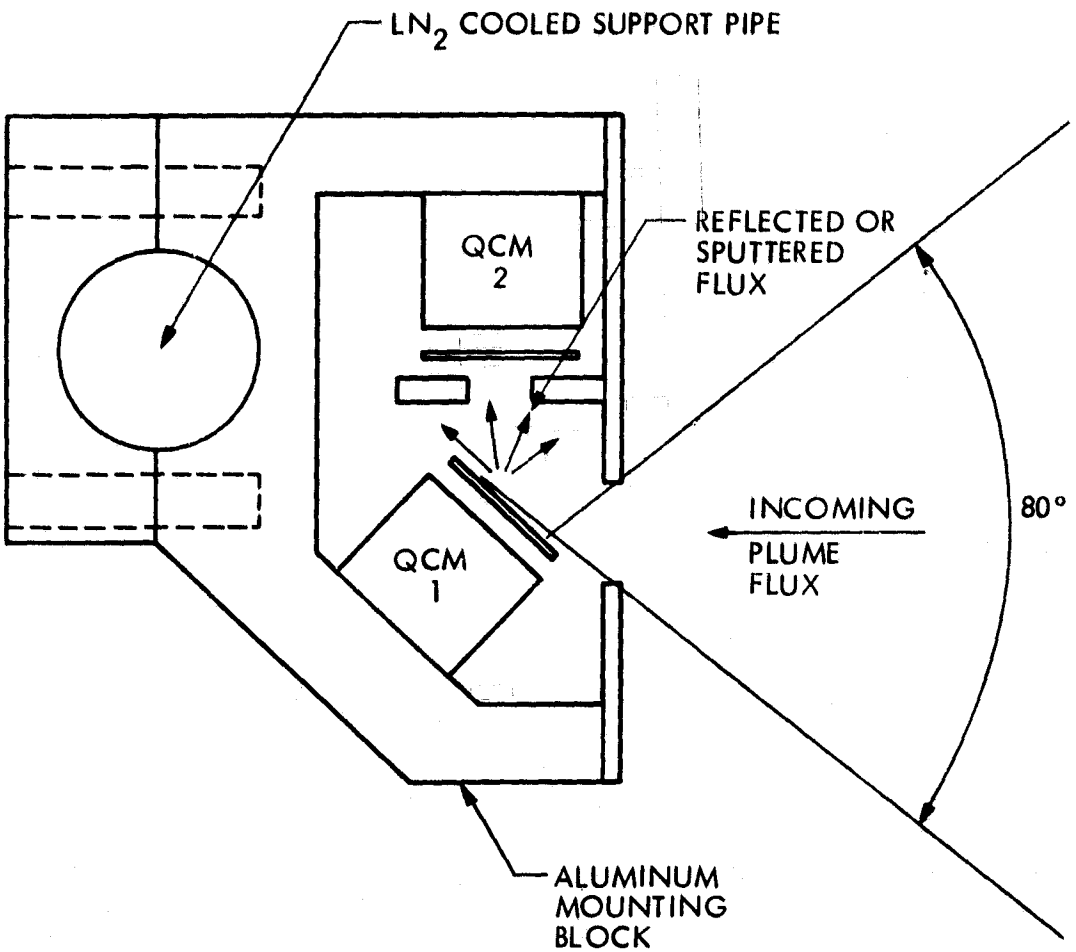

Figure 5. Double QCM Probe Schematic

rather than ablating and reflecting from it.

The axial plume mass flux, $\dot{m}$, can be found by eliminating the reflected and ablated mass flux, $\dot{m}_r$, from Equations (1) and (2):

$$\dot{m} = \left(S_1 + \frac{S_2}{K}\right) \frac{1}{\cos 45^\circ} \qquad (3)$$

The values of S_1 and S_2 can be measured locally to give a local value of $\dot{m}$, provided the constant, K, is known. This constant can be found through a calculation of the total mass flow rate, $\dot{m}_T$, from the thruster discharge as follows.

The total mass flux over the entire plume cross section is given by:

$$\dot{m}_T = \int_A \dot{m}\, dA \qquad (4)$$

where dA is a differential cross-section area element, normal to the thruster axis. Substituting into equation (3):

$$\dot{m}_T = \left\{ \int_A S_1 dA + \int_A \frac{S_2}{K} dA \right\} \frac{1}{\cos 45^\circ} \qquad (5)$$

Under the assumption that the constant, K, is independent of radius, equation (5) can be solved for K:

$$K = \frac{\dot{m}_T \cos 45^\circ - \int S_1\, dA}{\int S_2 dA} \qquad (6)$$

The total mass flow rate, $\dot{m}_T$, is known to be 1.56 mg/pulse; thus measurements of S_1 and S_2 versus radius can be used to experimentally evaluate the constant, K. Once known, K can be substituted along with

local values of S_1 and S_2 into equation (3) to give the local axial plume mass flux, $\dot{m}$.

The double QCM probe used in the testing is shown in Figure 6 with and without its cover plate. The quartz blank of QCM 1 with both its collecting and reference electrodes can be seen. QCM 2 has a separate cover plate to insure that the mass collected on QCM 2 is only from that eroded and reflected from the QCM 1 collecting electrode, and not from any spurious internal scattering. The circular shaft shown in the photographs is a mounting fixture used for assembly that simulates the required liquid nitrogen (LN_2) cooling line. When installed in the SEP vacuum facility, the LN_2 cooling line consisted of a 1.5 inch diameter flexible stainless steel tube fed through the top of the vacuum tank and down to the double QCM probe where its end was plugged. This cooling line was filled with LN_2 from outside the vacuum tank, while gravity acted to keep the LN_2 down at the end of the tube at the probe. The 1.5 inch diameter was necessary to prevent a vapor lock from forming and preventing the LN_2 from reaching the double QCM probe.

The double QCM probe was mounted on a movable support that was capable of sweeping the probe radially outward from the thruster axis to a radius of roughly 75 cm. A complicating factor in the construction of this support was the requirement that the probe remain tied to the LN_2 feed line. Although made of flexible steel tubing, at LN_2 temperatures this line is relatively stiff, requiring that the support be sturdy enough to move the probe against the drag of this LN_2 line. Two design options were considered: 1) a support rack which pivots about a point in the PPT nozzle exit plane at the thruster

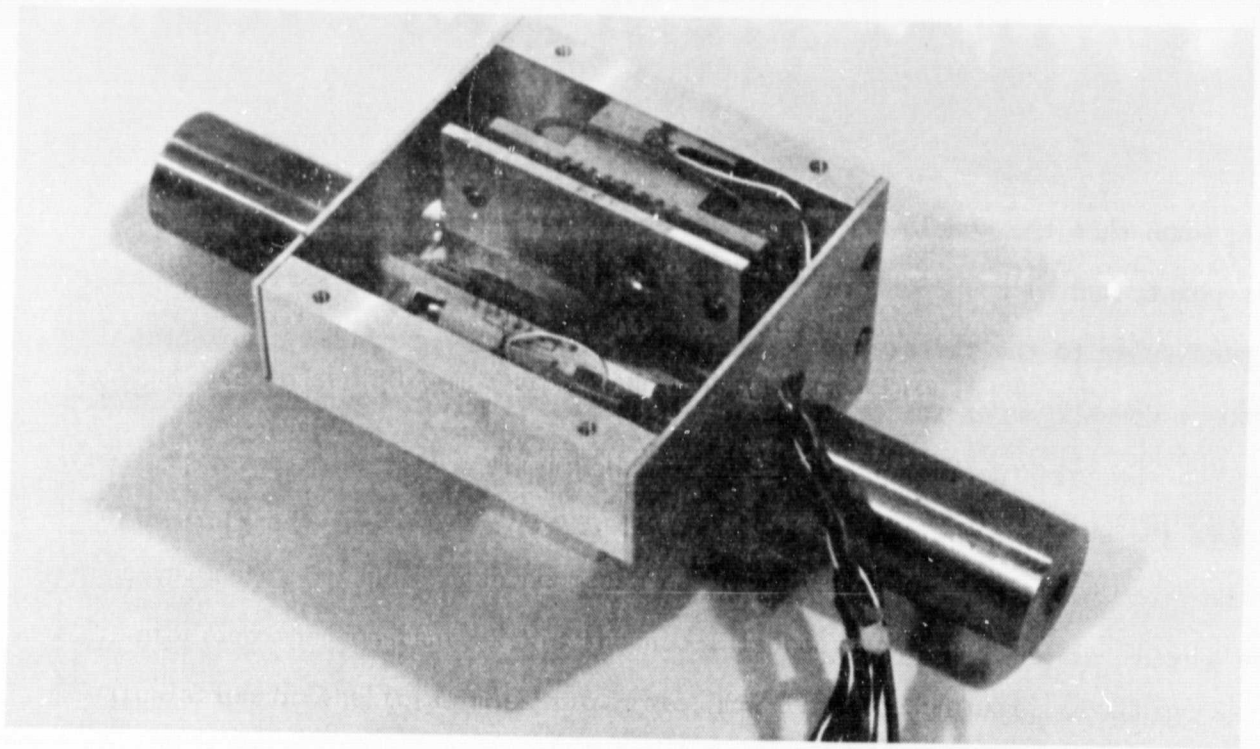

a) COVER PLATE REMOVED

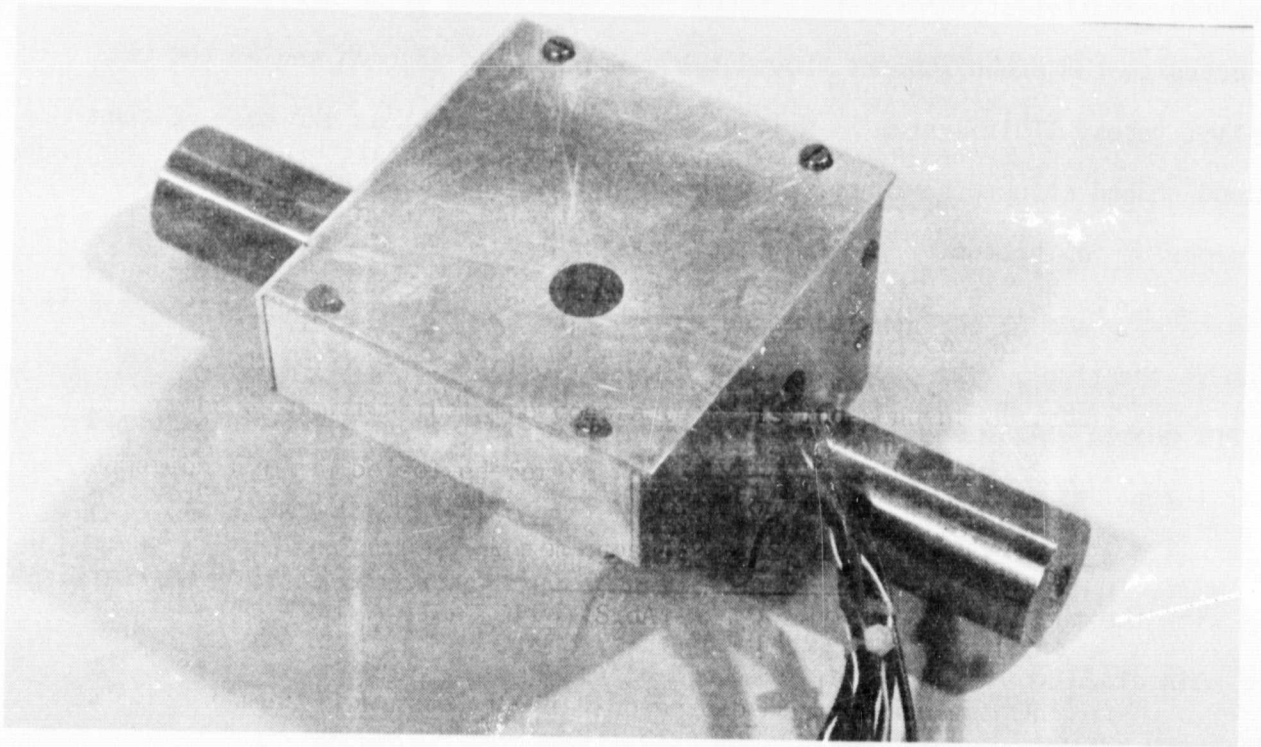

b) COVER PLATE IN PLACE

Figure 6. Double QCM Probe Photographs

axis, such that the double QCM probe was always at a constant distance from this point; and 2) a support rack which moves radially along a straight line perpendicular to the thruster axis, such that the probe remained a constant distance downstream of the PPT nozzle exit plane. The first option would have required the construction of a strong, curved track and a complex motor assembly to move the support along this track. In addition, maintaining the alignment of the probe would have been difficult. Because the second option is mechanically more simple, it was chosen for the support design.

Figure 7 shows a photograph of the final installation in the SEP vacuum facility. The probe is mounted in a support which slides on Teflon bearings along two parallel stainless steel tubes. A cable-chain drive system is connected to the probe support around two pulleys, seen at each end of the two parallel tubes. This system is driven by an electric motor at the base of the diamond shaped structural frame. The LN_2 feed line can be seen curving from the probe up to the top of the vacuum tank. With this system, the double QCM probe can be positioned anywhere between 30 cm to the left of the thruster axis to 75 cm to the right. The probe cover plate was positioned 74 cm downstream of the PPT nozzle exit plane, approximately at the same location as the aluminized Mylar target discussed in the previous section.

Using the double QCM probe, measurements were made over a period of several days with the thruster firing once every 17 seconds. The SEP facility walls were maintained at LN_2 temperature to minimize the wall-plume backscatter. The data taken during this test were reduced to the mass flux values, S_1 and S_2, for both QCMs in the probe. These are shown in Figure 8, plotted versus radius

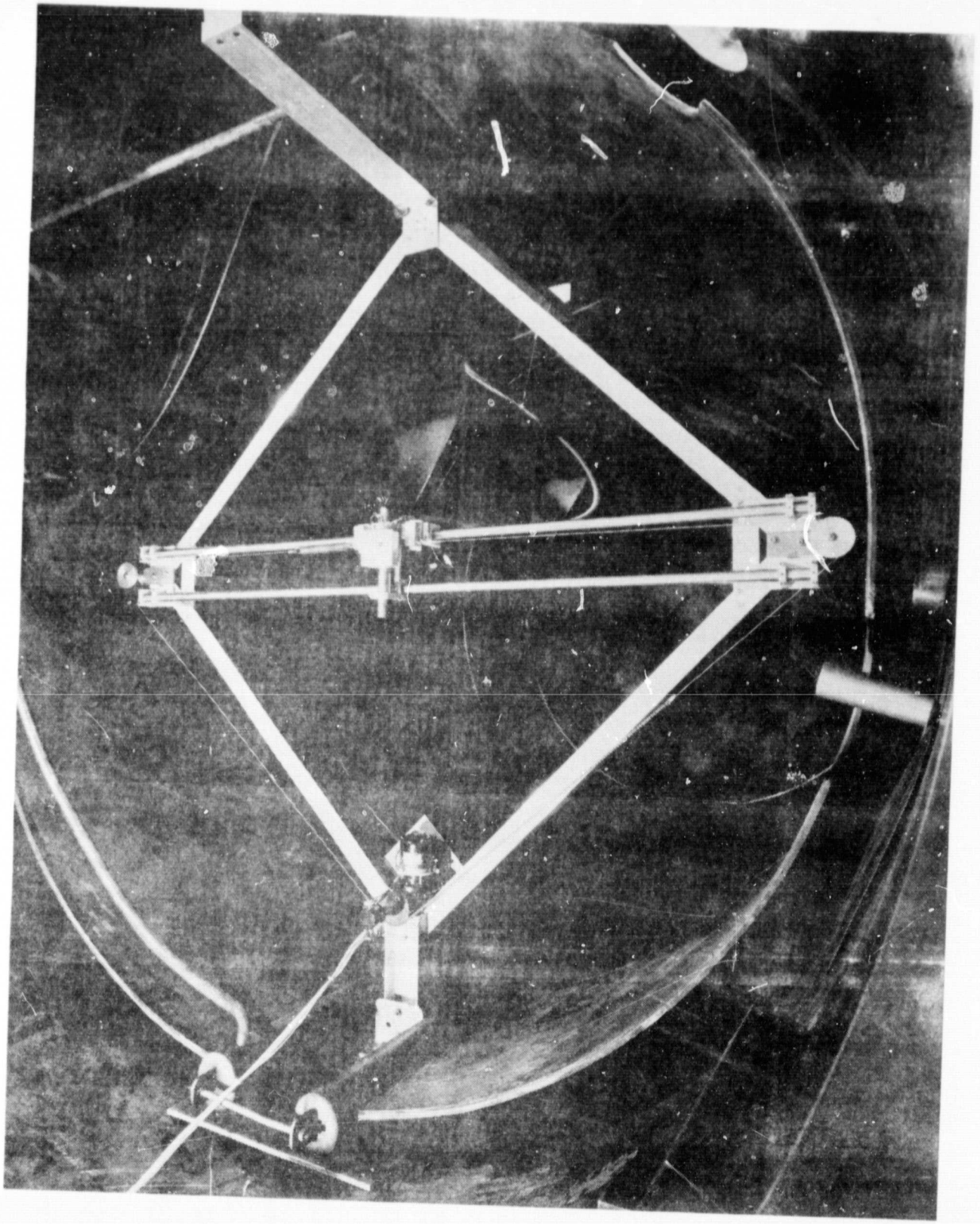

Figure 7. Double QCM Probe Support

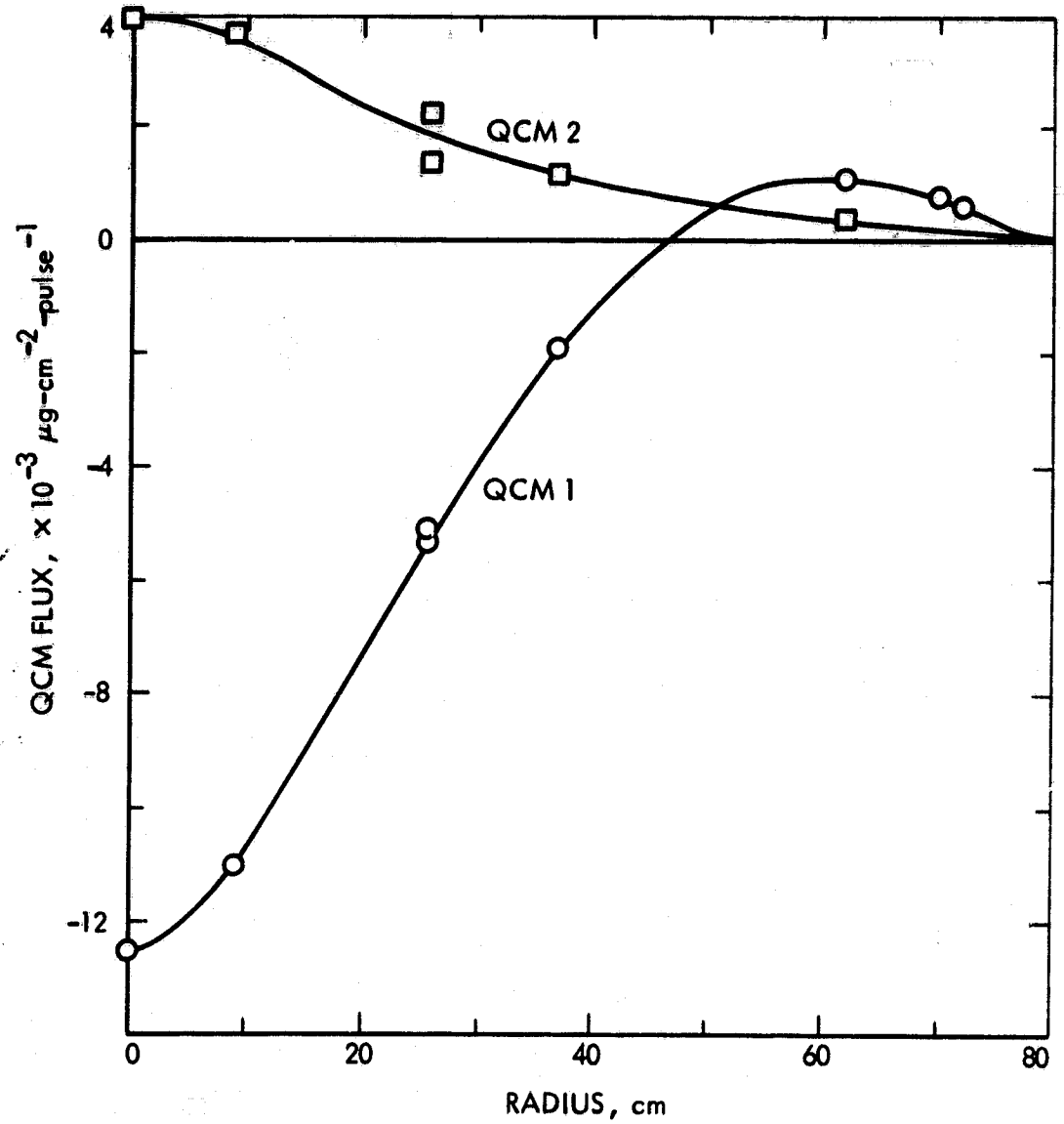

Figure 8. Double QCM Probe Data

measured from the PPT plume axis. As expected, the signal from QCM 1 indicates its collecting surface is eroding for probe positions out to a radius of about 45 cm. The signal from QCM 2 is consistent with this erosion in the sense that it is largest when the eroded mass flux is largest, and hence when the greatest amount of material is available for collection.

The two data points shown for each QCM at a radius of 26 cm were taken on opposite sides of the thruster axis, and thus provide a measure of the symmetry of the plume and the accuracy of the probe analysis. The two data points of the QCM 1 signal are virtually identical, indicating that the incoming plume mass flux is the same on opposite sides of the PPT axis, and, hence, is axisymmetric. The two data points of QCM 2 differ by about a factor of 1.6, indicating that the fraction, K, of scattered and eroded material collected by QCM 2 from QCM 1 can vary by as much as 60%.

Using the data of Figure 8, Equation (6) was used to calculate the constant, K. This value was found to be 0.014, and indicates that only 1.4% of the material reflected and eroded from QCM 1 is collected by QCM 2. The error induced in the calculated mass flux profile due to the variation in K can be seen in Figure 9 which shows this calculated profile versus radius. The two data points at a radius of 26 cm indicate that the error in this mass flux due to the variation in K can also be as much as 60%. With this implicit error in mind, the profile of Figure 9 still provides a reasonable measure of the mass flux distribution over the plume radial extent. This profile approximates a Gaussian shape, with a half width at half maximum of 28 cm, corresponding to an enclosed half angle from the plume axis of 21°.

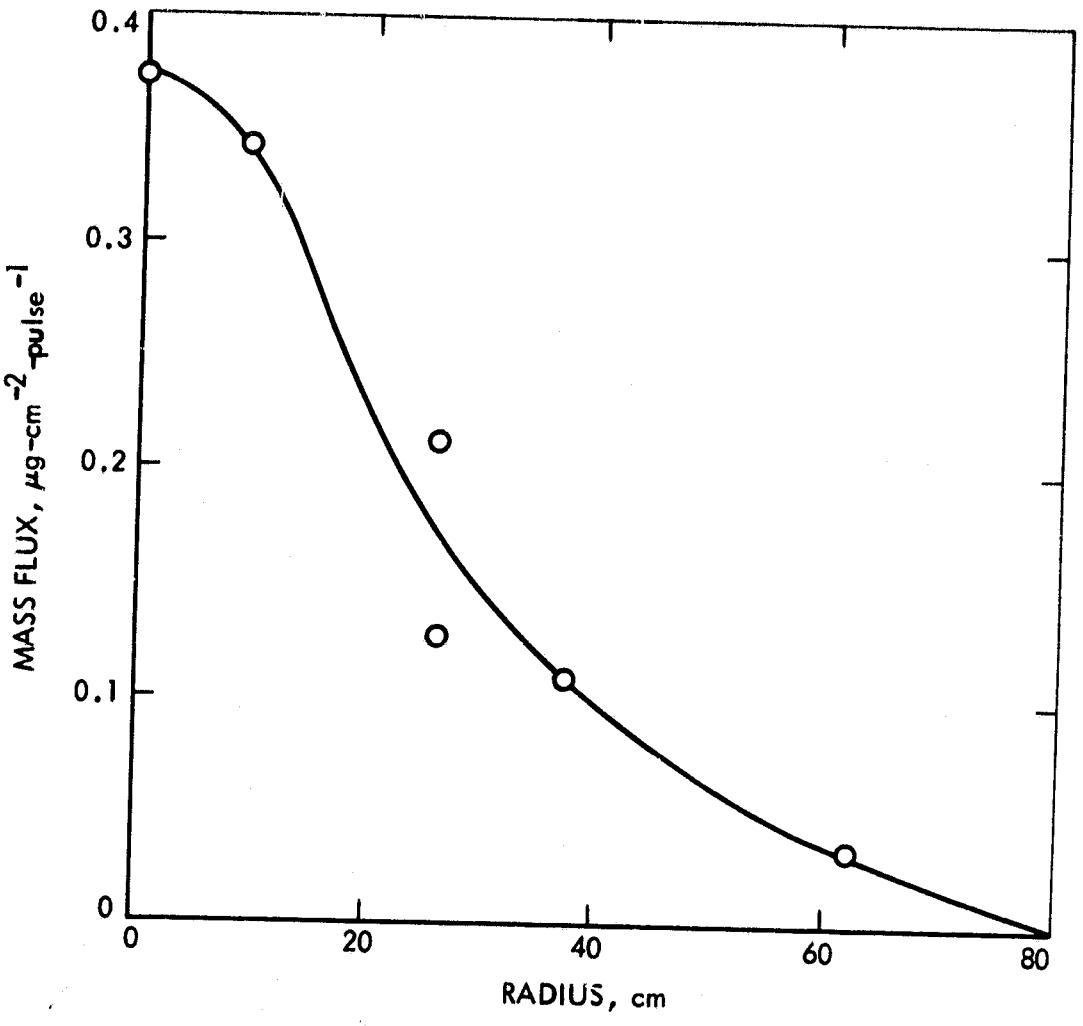

Figure 9. PPT Plume Mass Flux Profile

At a radius of 60 cm (which corresponds to an enclosed half angle of 40°) the plume flux is less than 10% of its centerline value.

2.3 High Speed Plume Photography Earlier studies of lower energy pulsed plasma thruster discharges have utilized high speed photography to study the evolution of the primary plume over the total discharge time.[11] These studies have provided valuable information about the PPT primary plume velocity and formation, which indicates that the plume is not a simple expansion of a homogeneous plasma. In order to investigate the properties of the 1 mlb PPT plume under study in this report, and to substantiate some of the previous experimental results, a high speed photography study of the PPT primary plume was carried out. In particular, a measure of the plume velocity was desired in order to determine the time at which the plume collides with the vacuum tank wall and begins to backscatter.

This study was carried out with the thruster installed in the SEP vacuum facility in the same location as for the previous Mylar target and double QCM probe tests. An observation port in the side of the vacuum chamber was used to view the plume. This port has a glass window with its center displaced 46 cm downstream of the PPT nozzle exit plane. The experimental set-up is sketched in Figure 10, and shows the trigger delay generator (TRW model 46A) which served to trigger the camera shutter after a set delay from the beginning of the PPT discharge pulse. The camera is a TRW image converter camera model 1D and used a microsecond framing plug-in unit Model 4B to control the number and length of exposures per discharge. This particular framing

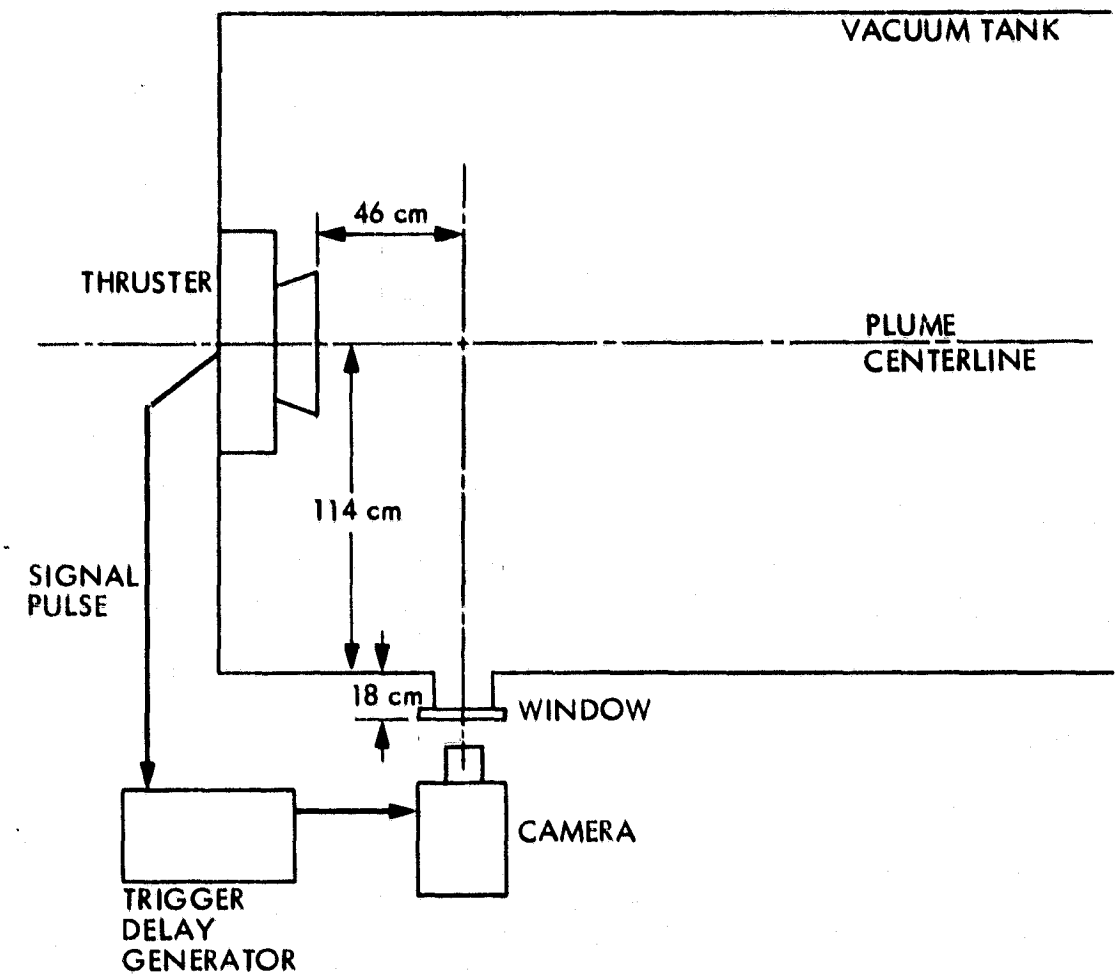

Figure 10. High Speed Camera Test Set-up

unit allowed three separate exposures to be made during each PPT discharge. The duration of each exposure was of order 0.2 μsec and the separation between each exposure was controllable between 0.5 and 20.0 μsec. To insure that the axis of the camera was perpendicular to the PPT plume axis, and to determine the exact image demagnification, a ruler was suspended from the top of the vacuum tank, along the thruster axis. The camera was aimed at a point on this ruler corresponding to a right angle between the thruster and camera axes and a photograph of the scale was taken. The demagnification was then calculated and found to be 13.9:1.

Figure 11 shows a sample series of photographs taken of the PPT plume. Each individual frame has three grid lines superimposed on the actual plume exposure. The overall series shows the time history of the plume as it passes the observation area, with time increasing from the bottom of the figure. Each group of three pictures was taken during one discharge pulse. In order to compare the plume behavior from pulse to pulse, each separate series of photographs overlaps the time of the accompanying series. The photographs in Figure 11 span the time from when the plume first appears in the viewing region, about 19 μsec after discharge initiation, to when the plume luminosity decays to where it is no longer visible, about 37 μsec after the discharge initiation. As observed, the plume is not homogeneous, but in fact contains locallized regions of high luminosity, and thus presumably high density. Over fifty photographs similar to those in Figure 11 were taken and all show some degree of nonuniformity in the luminosity pattern. The nonuniformities in the plume plasma must average out over many discharge

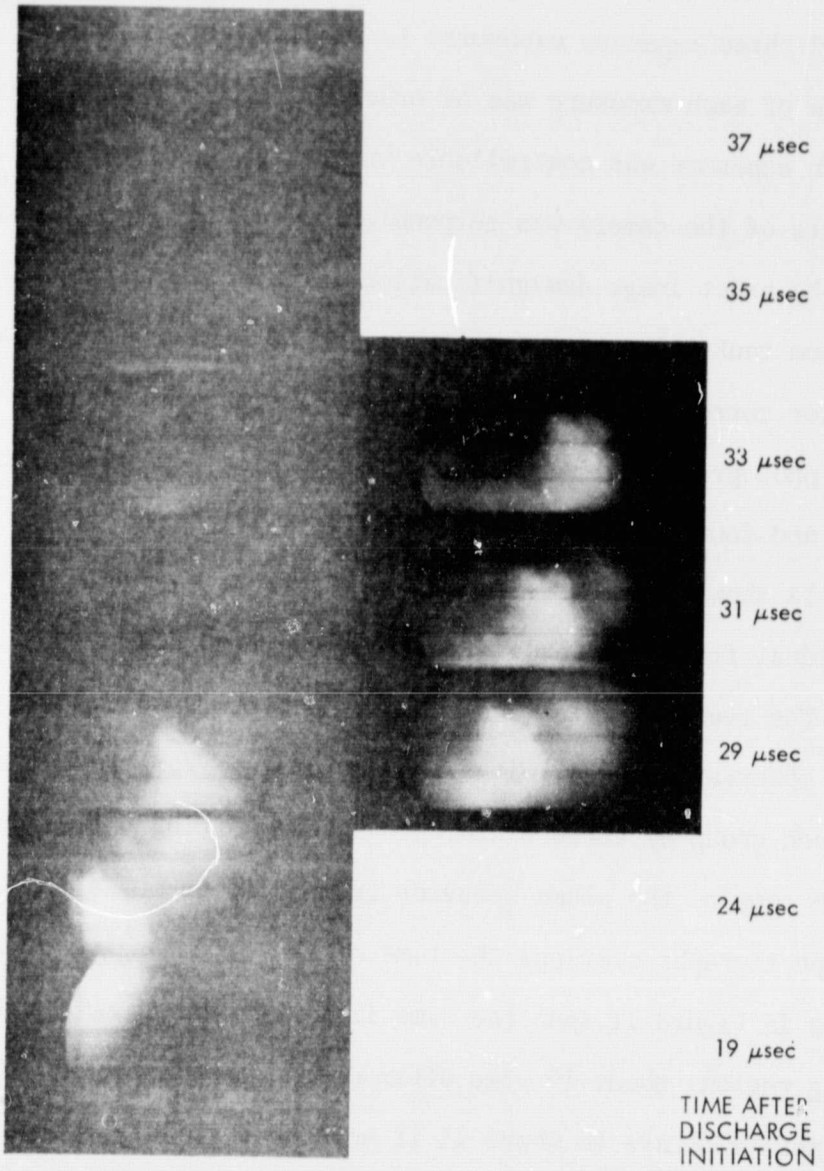

Figure 11. PPT Plume Photographs

pulses, in order to give the relatively uniform experimental results found with the Mylar target and double QCM probe tests. The plume backflow is expected to behave in a similar manner, since it originates in the primary plume.

The velocity of the luminous discharge plasma seen in the photographs of Figure 11 can be determined by calculating the time-of-flight distance between one photograph and another, separated by a known time interval. Using this method, the velocity of the plasma front as seen in the earliest group of pictures in Figure 11 is 30 $\pm$ 5.5 km/sec. The velocity of the bright luminous region, seen in the middle group of Figure 11, is 23 $\pm$ 5.5 km/sec. The error bars in these velocities represent standard deviations calculated by combining the measured velocities of several series of photographs similar to those in Figure 11. The discrepancy between the velocities of the plume leading edge and the luminous region inside the plume may be due to several reasons, including different magnetic force acceleration patterns, and different local acoustic flow properties.

The plume average exhaust velocity is known to be 17 km/sec, which is significantly smaller than the two measured velocities. This suggests that the luminous portion of the plume consists of only a fraction of the total discharge mass and that the remainder is moving at a velocity lower than the plume average. This type of behavior has been seen before in micropound thrusters[10], where the luminous portion of the plume was found to be the ionized fraction of the plume. Measurements of the ion velocity of the millipound thruster plume were made at Fairchild [5] using

a Langmuir probe and show good agreement with the present photographic measurements.

In the MOLSINK facility, where the plume backflow measurements were made, the thruster was installed with its exit plane perpendicular to the major axis of the ellipsoidal tank, roughly 1.5 m from the tank end. Thus, the plume leading edge will reach the tank wall roughly 50 μsec after the PPT discharge initiation. Since this portion of the plume is the most energetic, it would be expected that most of the wall backscatter would originate with this portion. Assuming, conservatively, that the backscatter velocity is equal to the incoming plume velocity, the backscatter will reach the area of the thruster nozzle roughly 100 μsec after the discharge initiation.

The energetic portion of the PPT plume is ionized and thus is confined to within the magnetic field pattern of the PPT discharge. The lower energy, slower moving portion is not confined by this field and thus, is free to flow radially outward and axially upstream more easily. The PPT plume backflow is expected to be primarily composed of material from this lower energy portion. Although the velocity of this portion of the plume is unknown, it must be less than the plume average velocity and is probably close to its sonic velocity. Assuming the temperature of this material is less than 10,000 K, an upper estimate of the velocity can be found from the definition of the sonic velocity, C_S:

$$C_S = \sqrt{\gamma RT}$$

where γ is the ratio of specific heats and is taken to be 5/3, and R is the ideal gas constant divided by the average plume molecular weight of 16.7 amu[8]. The result gives a value of roughly 3000 m/sec, or about one-tenth of the high speed plume portion. Using the estimated wall backscatter return time of 100 μsec, the low speed backflow will travel only about 30 cm from the thruster axis before the wall backscatter overtakes it, thus any backflow measurement in the MOLSINK facility must be designed to correct for an almost simultaneous wall backscatter.

In addition to the preceding observations of the PPT plume on the thruster axis, the high-speed camera was also used to determine the expansion angle of the luminous portion of the plume. Figure 12 shows a schematic of the camera geometry used to make this measurement. At the camera axial position of 46 cm, it was tilted up from its original position, aligned perpendicular to the thruster axis, to a position where the edge of the plume was centered on the photograph. As shown in part (a) of Figure 12, the angular displacement was found to be 17°. Using this angle and the known distance from the camera to the thruster axis (132 cm), the plume radius at this axial location can be determined. As shown in part (b) of Figure 12, the plume expansion angle, θ, can then be calculated and found to be roughly 10°, which is in agreement with the previous measurements. From the photographs taken of the PPT plume edge, the velocity of the plume at this location was found to be 26 $\pm$ 5 km/sec. This velocity is approximately equal to the measured center-line plume velocity; thus the plume velocity radial profile is essentially flat out to the plume edge. This type of radially uniform velocity profile is similar to those found in other types of plasma thrusters.[12]

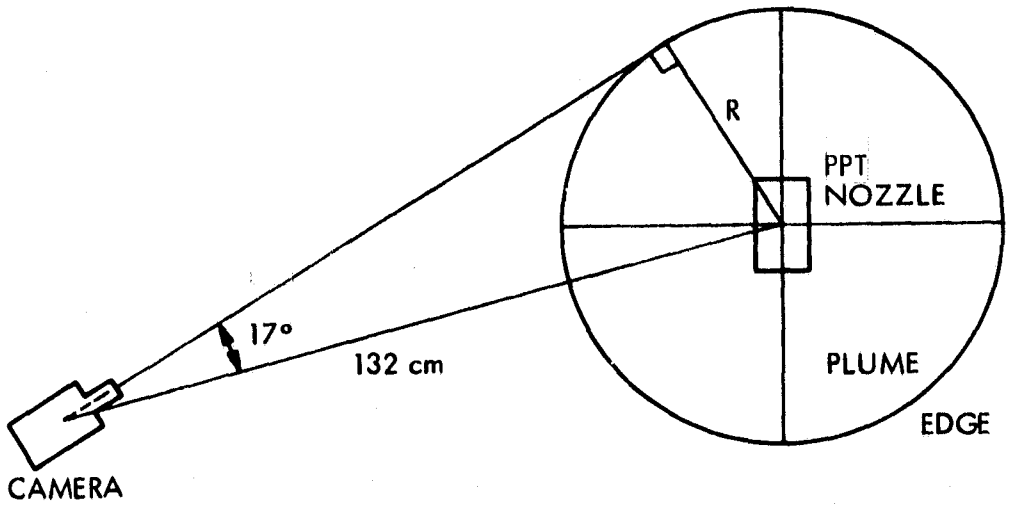

(a) END VIEW

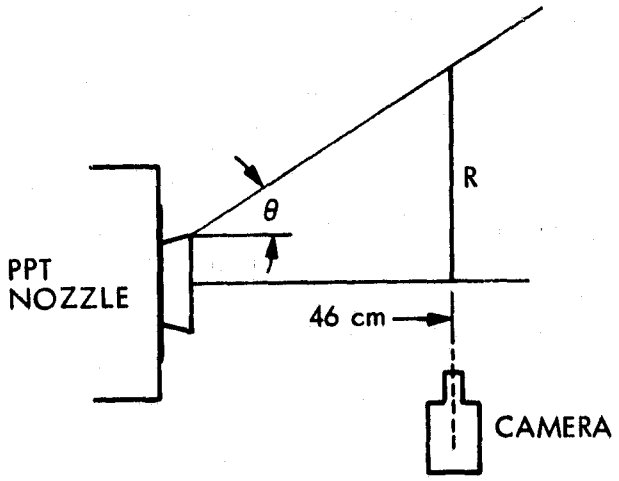

(b) SIDE VIEW

Figure 12. PPT Plume Camera Geometry

2.4 Plume Composition Analysis The results of the previous studies have indicated that the plume material in the central part of the primary plume is energetic enough to erode the vacuum tank wall surfaces. In addition, it is known that the major amount of plume-wall backscatter is from this central part of the plume.[6] These two facts combine to suggest that the backscattered material from the tank walls may be composed of ablated material from the wall, and hence, recognizably different from the backflow from the plume itself. In order to determine if this possibility is indeed true, a series of tests was run to determine the plume composition using visible light spectroscopy and carbon disk analysis.

A 0.5 m Jarrel-Ash grating spectrometer was set up in the same location as the high speed camera shown in Figure 10, to observe the optical radiation from the PPT exhaust plume perpendicular to the plume axis. The wavelength range from about 2000 Å to 6000 Å was covered using Royal Pan Film, with a mercury vapor lamp for a comparison spectrum. Exposures were varied from 15 to 45 discharge pulses to provide adequate resolution. The results indicate that spectral lines can be found over the entire range. Analysis indicates that much of this radiation is due to singly ionized fluorine with some contributions from ionized carbon. No lines from neutral carbon or fluorine, or from any other specie, were found. This indicates that the energy of the plume neutral specie component is such that the radiation from this component is negligible with respect to that from the ionized specie. It also suggests that little recombination of the charged particle plasma is occurring upstream of the observed plume region. Since no spectral lines from any specie from

the vacuum tank wall were observed, it appears that the wall backscatter cannot be resolved from the plume backflow using this spectroscopic method.

An alternate method of resolving the possible differences between the plume backflow and wall backscatter involves the analysis of the material deposited on sampling surfaces exposed to the PPT plume. A scanning electron microscope (SEM) was used to observe the morphology of the surface deposits on these sampling surfaces and energy-dispersive X-ray analysis was used to identify the atomic species. This type of X-ray analysis is unable to differentiate between species of atomic numbers lower than 9; hence only the fluorine in the Teflon propellant can be identified, while the carbon will remain transparent. In addition to possibly differentiating between backscatter and backflow, scanning electron microscopy is also useful in checking the uniformity of the deposits on the collecting surfaces. This uniformity strongly affects the calibration constant for the QCMs used in these plume studies. For the previous work, including that of the Phase I effort, this deposit was assumed to be uniform and the calibration constant was calculated accordingly. This assumption can be checked using the aforesaid method. These analyses, including both the SEM photography and the X-ray energy dispersive spectroscopy, were performed by Dr. Raymond L. Chuan of the Brunswick Corporation.

Initially the analysis was carried out on the deposit on the collecting surface of a QCM used in the off-axis skimmer of the Phase I testing.[6] It was hoped that an examination of this QCM would provide some evidence of the species backscattered from the tank wall, since only this backscatter could have reached the QCM. An SEM photograph of a portion of this QCM

collecting surface is shown in Figure 13 (a). As evident, the deposit on the QCM platinum electrode surface consists of relatively few isolated particles. Particle A is shown at a greater magnification in Figure 13 (b), where it appears to be amorphous with an overall size of roughly 80 microns. X-ray spectra of this particle indicate that it is composed primarily of aluminum and hence, is probably a sputtered particle from the aluminum in the vacuum tank walls or QCM body. The remaining particles were each examined and found to have no resolvable X-ray spectra, indicating that they are composed of low atomic number elements (less than 9), which may or may not be from the PPT plume.

Analysis of the previous QCM surface was ambiguous, since its collecting surface was shielded from the PPT plume by the skimmer wall and since little measurable mass was deposited on its surface. In addition, the X-ray spectra of the few particles on this QCM surface were masked by the spectra of the silicon from the quartz crystal and the platinum from the actual collecting electrode. To remedy these problems, three carbon disks approximately 1.0 cm in diameter were installed in the MOLSINK facility to be exposed to the PPT discharge. Carbon disks were used because carbon has an atomic number of less than 9, and hence is transparent to the X-ray spectroscopy used. Each disk was placed in the bottom of a 2.0 cm by 3.0 cm box, roughly 1.0 cm deep, which acted as a relatively open collimator to control the region viewed by the carbon disk surface. These boxes were either pure aluminum foil or commercial pot metal depending on the particular carbon disk. Two of the carbon disks were placed side-by-side on the downstream edge of the thruster aluminium

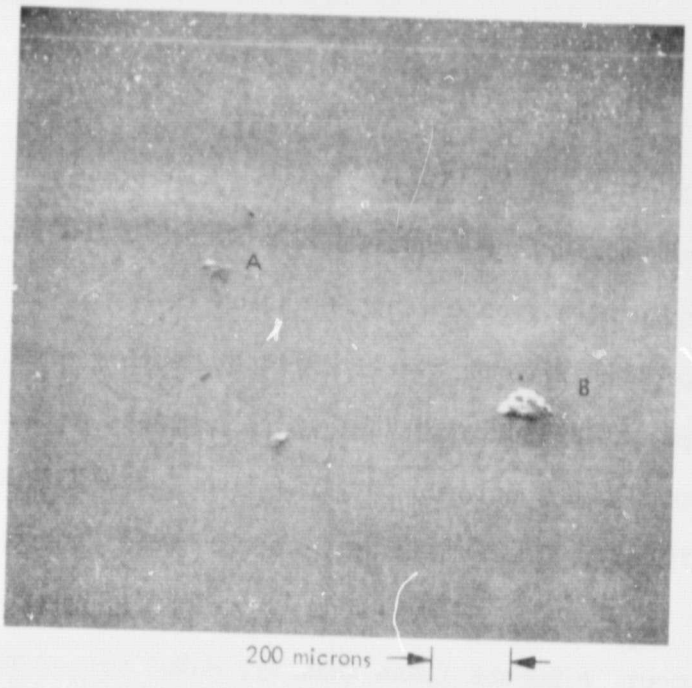

(a)

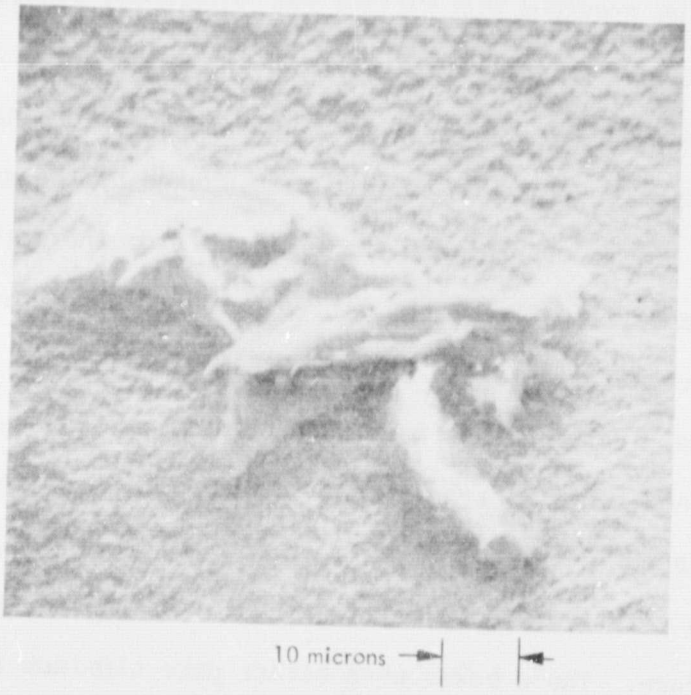

(b) PARTICLE A

Figure 13. SEM Photographs of QCM Electrode

enclosure, approximately 15 cm off the thruster axis and 5 cm upstream of the exit plane. They were set to face directly downstream toward the MOLSINK wall area where the backscatter is greatest. One of these disks was mounted in a pure aluminum foil box and the other in a pot metal box. The third disk was attached to a bracket on the MOLSINK wall, about 45° off the thruster axis. This disk was set to look directly into the thruster discharge chamber and was in a pot metal box. These disks were exposed to approximately 110,000 discharge pulses and then removed for analysis.

The analysis of the two carbon disks mounted together on the thruster enclosure indicates that there is a quantitative difference between the deposit collected on the disk in the pure aluminum box and the deposit on the disk in the commercial pot metal box. This difference indicates that some material was actually eroded from the boxes containing the carbon disks. Thus, any elements which are contained in the box material and are seen in the analysis may not necessarily originate in the PPT plume or tank wall backscatter. These elements include aluminum from all the boxes and iron, lead, zinc, and other trace elements from the pot metal boxes.

The carbon disk from the pure aluminum box mounted on the thruster enclosure and facing downstream was analyzed to determine the deposit morphology and elemental composition. Two sample SEM photographs of the carbon disk surface features are shown in Figure 14. Figure 14 (a) is a low magnification view which shows a number of particles adhering to the surface. Figure 14 (b) is an enlarged view of particle A showing it to be an amorphous lump of material seemingly composed of many

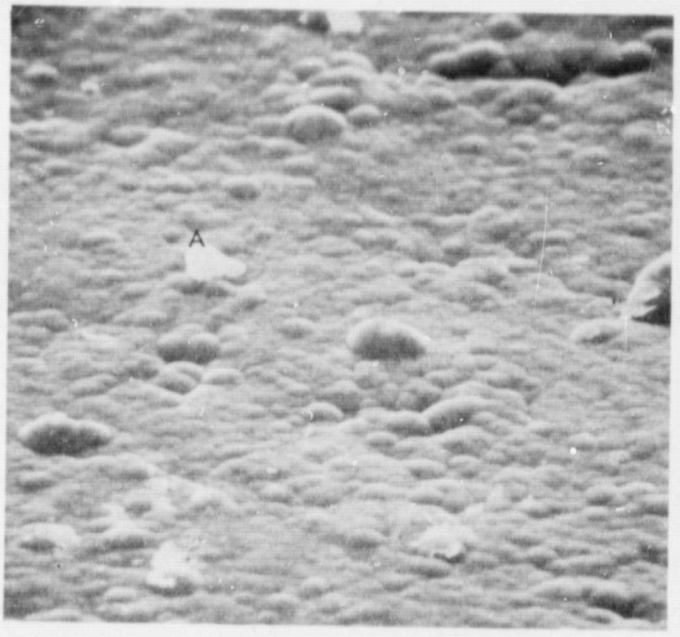

(a)

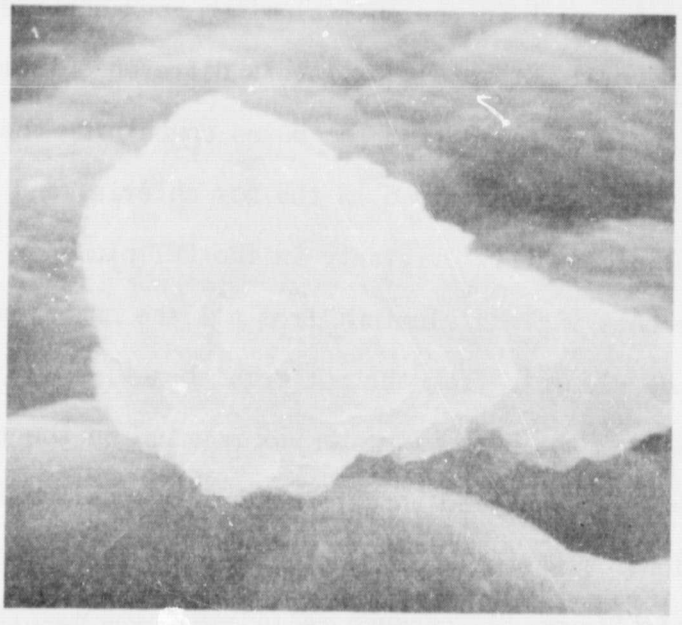

(b) PARTICLE A

Figure 14. SEM Photographs of Carbon Disk Deposits

small spherical particles. X-ray spectroscopic analysis of this particle shows a strong fluorine line which is probably in chemical combination with carbon, making this particle similar to Teflon. Figure 15 shows two more enlarged views of particles observed on this carbon disk. X-ray analysis indicates that these particles also show Teflon; however, their morphology is fundamentally different from that of Figure 14 (b). Both of these particles, and in fact almost all the observed particles, appear to be cracked from a uniform layer built up on the carbon disk substrate. This cracking may possibly be due to thermal stresses induced during the warming of these disks to room temperature after having been maintained at low temperatures during the experiment.

Although the carbon disk mounted on the MOLSINK wall was installed in a pot metal box, and therefore subject to considerable contamination, the analysis of the deposit on this disk indicated several interesting points. To the naked eye, this disk was well covered with a material showing a velvety purple color similar to the deposits seen on the MOLSINK walls around the lower door. The surface density of particles on this disk was higher than that of the other disks; however, the analyses of these particles indicate that they are composed of materials from the pot metal box, and thus may not be due to the PPT discharge plume. As in the previous disk, this disk also showed the ubiquitous presence of fluorine over the entire surface, suggesting that the teflon propellant deposited in a uniform layer. In addition, copper, presumably from the PPT electrodes, was also seen to be uniformly distributed over the disk surface. This indicates that it is possible to

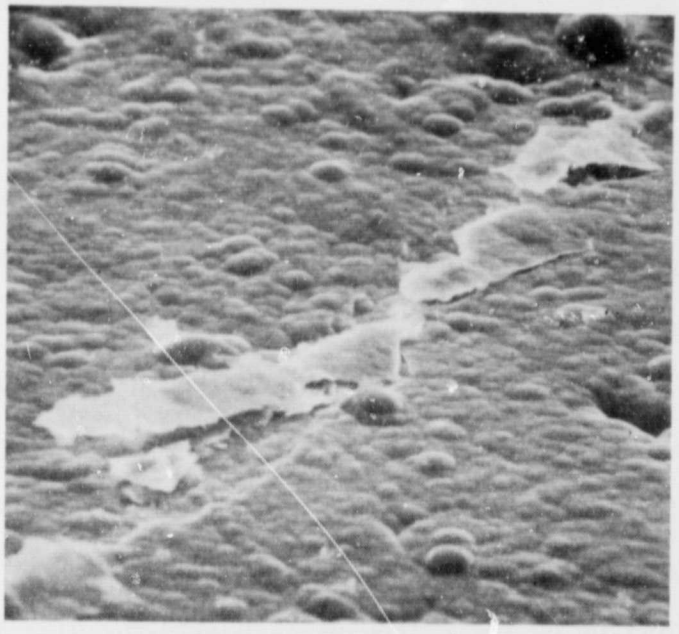

(a)

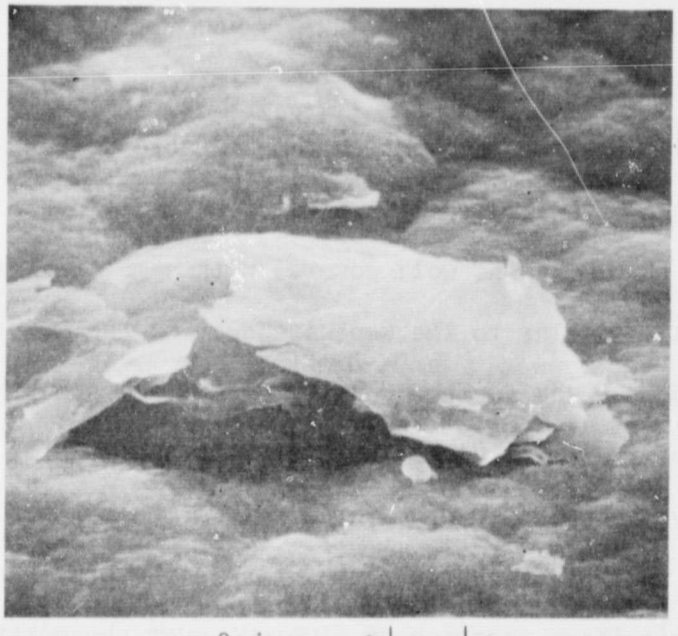

(b)

Figure 15. SEM Photographs of Surface Particle Cracking

qualitatively recognize the PPT discharge erosion products in the discharge and, hence, possibly determine the actual erosion rate.

This analysis of the carbon disks exposed to the PPT discharge indicates that there is no easily recognizable difference between the material rebounding from the MOLTRAP wall and the material flowing directly from the thruster discharge chamber. Thus, it would be impossible to distinguish between the PPT plume backflow and the plume-wall backscatter using this method. Further analysis indicates that the major part of the deposition on these carbon disks is in a uniform layer with only a few particles at isolated points. This type of deposition indicates that the earlier assumption of uniform deposition on QCM collecting electrode surfaces is accurate; hence the use of this fact in calculating the QCM calibration constant is justifiable.

2.5 Summary The previous studies of the PPT plume have provided valuable insight which can be applied to the design of an appropriate plume backflow measuring system. The measured axisymmetry of the plume downstream of 75 cm from the nozzle confirms that the plume-wall backscatter is axisymmetric, as was indicated in the Phase I studies. Furthermore, this axisymmetry suggests that the PPT plume backflow may also be axisymmetric; hence the experimental program to measure this backflow need not include an extensive study of the azimuthal variation in this backflow. The radial mass flux measured using the double QCM probe indicates that virtually all of the primary plume is confined to a 40° half-angle conical expansion. This measure of the plume boundaries and the estimate of the flux density within this plume will be useful in determining the regions to be observed in order to measure the plume

backflow. Finally, the plume velocity and composition analysis indicate that the plume backflow cannot be easily differentiated from the plume-wall backscatter, by either appropriate sensor timing or elemental analysis. Thus, to measure the plume backflow, a method must be developed which differentiates between the backflow and the backscatter in some other fashion, such as the method described in Section 1, using collimated QCMs.

3.0 BACKFLOW MEASUREMENT DEVELOPMENT AND TEST HISTORY

Based on the results of the previous section, it appears that the conceptual method of measuring the PPT backflow using collimated QCMs is feasible. This method requires the design and assembly of an experimental apparatus capable of supporting an array of collimated QCMs, moving these QCMs to various radial and axial locations in the plume, and varying the dip angle between the PPT nozzle exit plane and the collimator axis. In addition, each QCM must be cooled to LN_2 temperatures and have its temperature regulation, power, and output signal leads connected to the appropriate systems outside of the MOLSINK tank. The first half of this section will discuss the overall design of this experimental apparatus. Included in this discussion will be a description of the preliminary testing of various collimator designs carried out in the SEP vacuum facility.

After the assembly of the test apparatus, it was installed in the MOLSINK facility and used to gather the necessary experimental data required for the determination of the PPT plume backflow. The test history and the reduction of the test data from QCM beat frequency shifts to mass flux values will be discussed in the latter half of this section.

3.1 Collimator Design and Testing The conceptual technique for measuring the PPT plume backflow was discussed in Section 1.0. Referring to Figure 1 of that section , the collimated QCM signal consists of contributions from the PPT plume and the MOLTRAP wall area within the collimator observation region. For small dip angles, the plume-wall backscatter can be ignored; thus the collimated QCM signal would be due to the backflow from the observed volume of the PPT plume.

By using a collimated QCM which observes a plume slice of enclosed angle, $\Delta\alpha$, and observing these slices from a dip angle of zero out to the maximum value for negligible wall backscatter in steps of $\Delta\alpha$, the partial plume backflow from this total volume might be found by simply summing the measured signals. Unfortunately, physical limits of the collimator design prevent this simple procedure from giving accurate results, as can be seen by the following.

Looking in a direction perpendicular to the QCM collimator axis, the geometry is as shown in Figure 16. The region observed by the QCM collecting electrode can be divided into two subregions: the illuminato and the penumbra. Any point source of backflow in the illuminato will see the entire electrode surface; hence the measured QCM signal will be directly proportional to the electrode area. Any point source in the penumbra will see only a fraction of the electrode surface (due to shadowing by the collimator aperture), and hence, will depend on the electrode area in a more complex fashion. This partial shadowing must be corrected for in the summation of the QCM signals at different dip angles in order to insure that all the backflow over a given range of dip angles is measured. This correction is analytically very complex, as will be seen in Section 4, and hence, it is desirable to design the QCM collimator such that the penumbra and the associated correction to the measured QCM signal is small. As will be seen by the following analysis, this cannot be done under the existing experimental constraints.

Referring to Figure 17, the edge of the penumbra is at an angle, β, with respect to the collimator axis, and the edge of the illuminato is at an angle

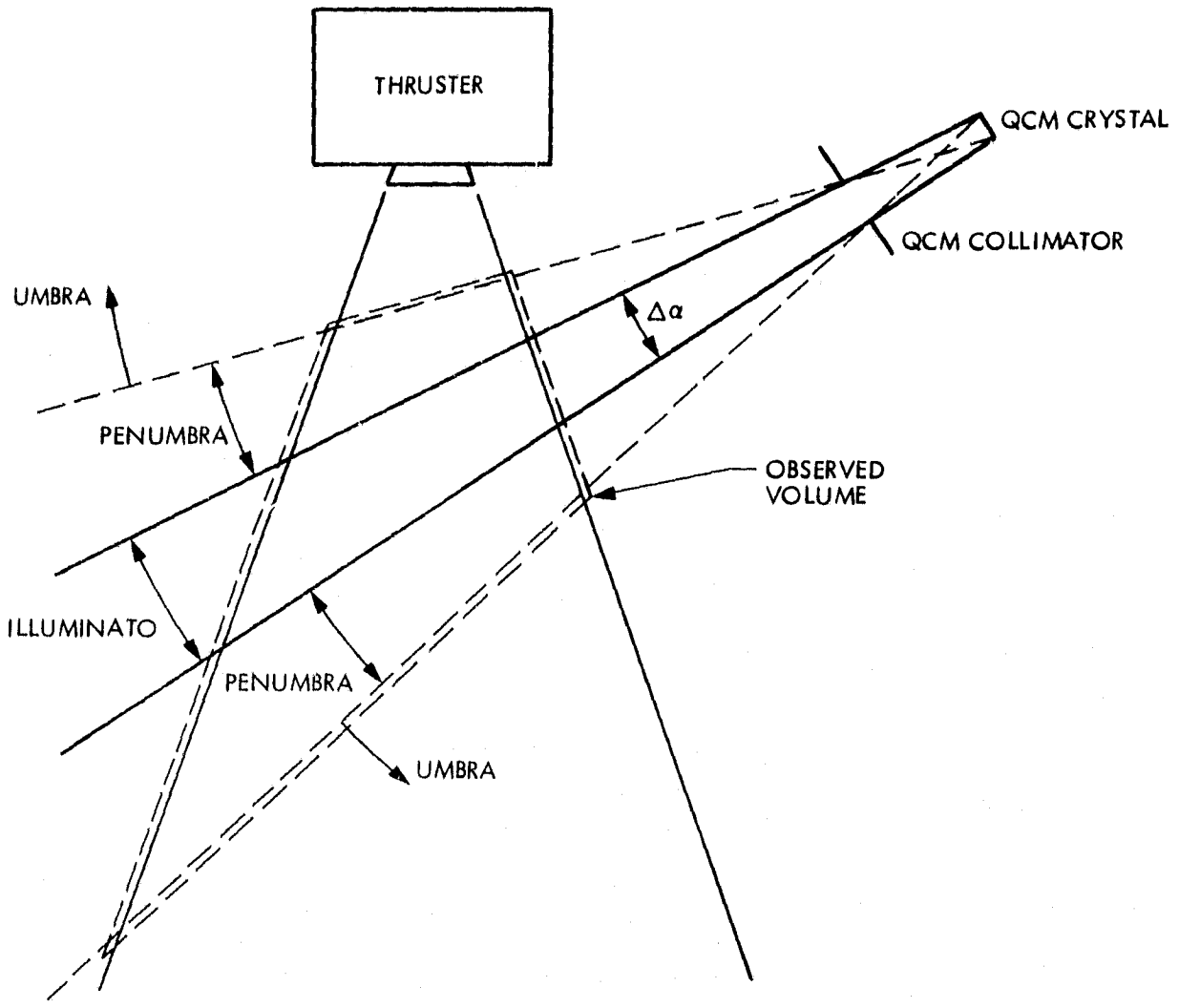

Figure 16. QCM Collimator Observation Region

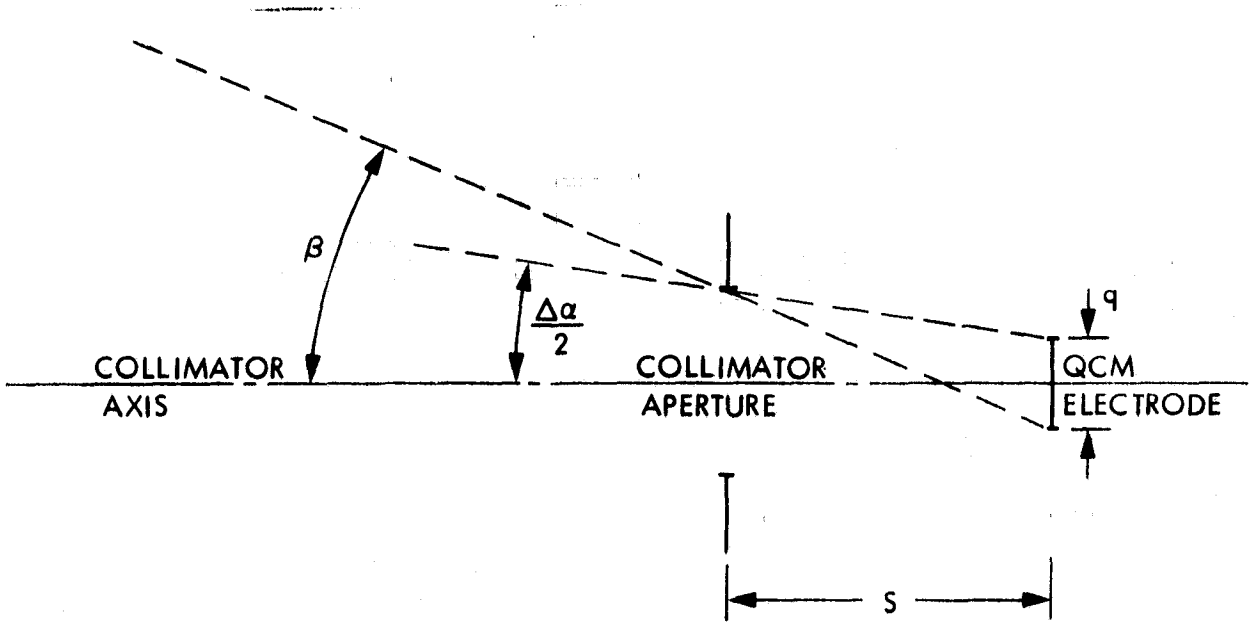

Figure 17. QCM Collimator Aperture Geometry

$\frac{\Delta\alpha}{2}$ with respect to this axis. With the QCM electrode width, q, and the electrode-aperture distance, s, the penumbra angle, β, is:

$$\beta = \tan^{-1}\left[\frac{q}{s} + \tan\frac{\Delta\alpha}{2}\right]$$

From Figure 1, it can be seen that the aperture angle , $\Delta\alpha$, should be less than 10^{o} to insure adequate spatial resolution. Table I shows the values of β calculated for various $\Delta\alpha$ and q/s. The QCM electrode width, q, is approximately 0.8 cm; hence the tabulated values of q/s cover a range of electrode-aperture distances, s, from 8 to 80 cm.

TABLE I. QCM Collimator Penumbra Angle (degrees)

$\Delta\alpha$ (degrees)	q/s		
	0.1	0.05	0.01
0	5.71	2.86	0.573
5	8.17	5.35	3.07
10	10.6	7.82	5.59
20	15.4	12.8	10.6

Practical considerations of the available space in the MOLSINK tank dictate that s should be no larger than about 10 cm; hence the ratio q/s is restricted to values greater than roughly 0.1. According to Table I, this indicates that the collimator penumbra angle will be equal to or larger than the aperture angle; hence the correction to the collimated QCM signal due to the penumbra must be large.

The choice of the collimator aperture angle depends on a compromise between the good spatial resolution of small apertures and the magnitude of the QCM signal which decreases with small apertures. The QCM signal not only depends on aperture size but also on exposure time, dip angle and location. In general, the signal decreases with increasing dip angle (out to the angle where the wall backscatter begins to increase) and with increasing distance from the thruster axis. To determine the magnitude of the QCM signal, and hence, aid in the final choice of collimator aperture angle, a series of tests was run in the SEP facility with two types of QCM collimators at various locations. The collimators are identical except for the aperture angle, which is 20° for some collimators, and 0° for the remainder. A perspective view of the 0° aperture angle collimator is shown in Figure 18. The QCM crystal is exposed to the main collimator through a 0.8 cm square hole cut in the center of the collimator backplate. The front face of the collimator is circular so that the aperture angle remains constant over the entire width of the collimator slice. This width is set at 100° to include the entire width of the PPT plume and yet not over expose the regions outside of the plume which would contribute to the observed wall-plume backscatter. The radius of the curve front is 8.0 cm, exactly 10 times the QCM electrode width; hence the penumbra angle for the 20° collimator is 16° and for the 0° collimator is 5.7° (see Table I).

Six collimated QCMs were mounted in the thruster nozzle exit plane in a rectangular array as shown in Figure 19. The three rows of two QCMs each were placed 48 cm, 63 cm, and 78 cm from the thruster axis, respectively.

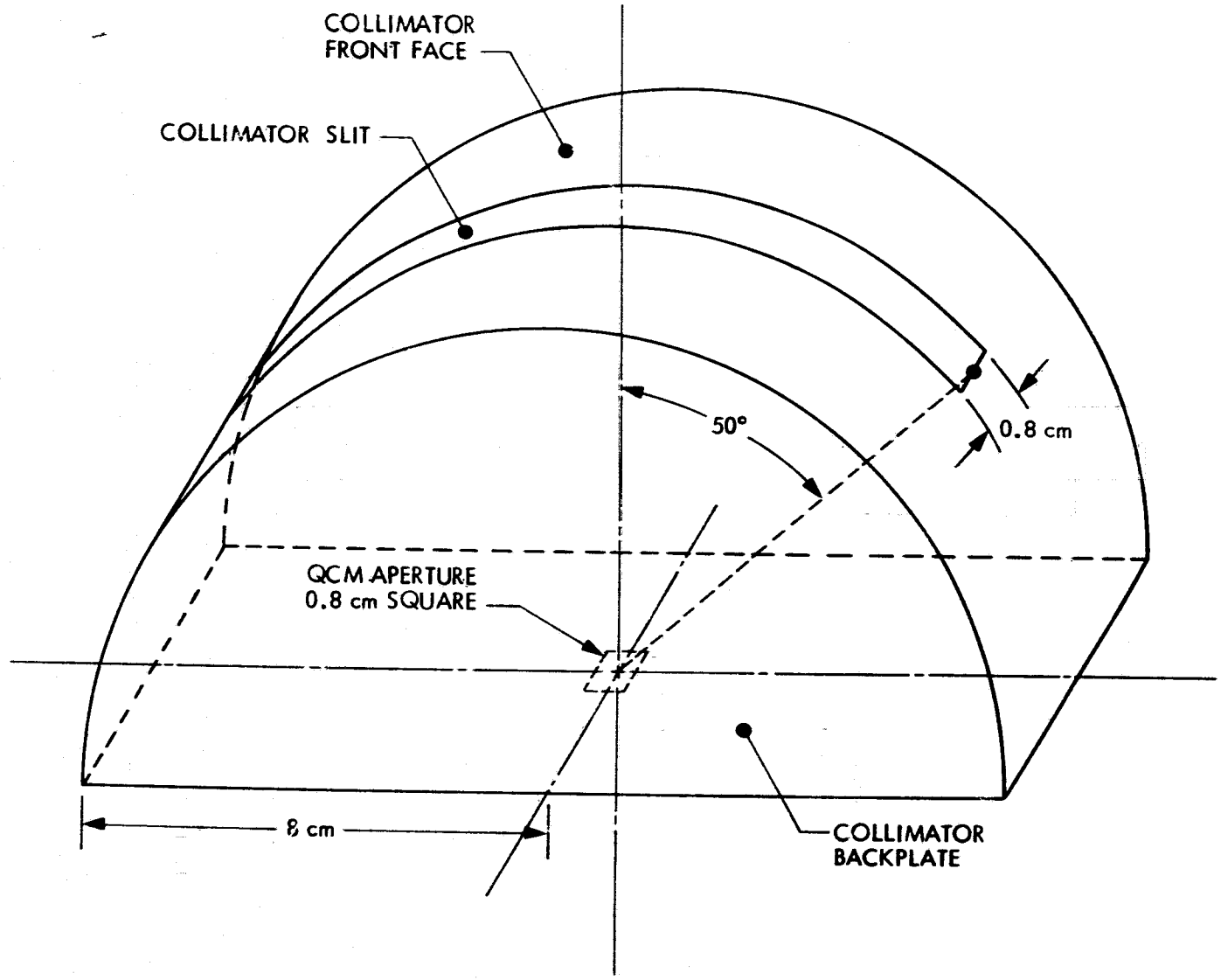

Figure 18. QCM Collimator Design

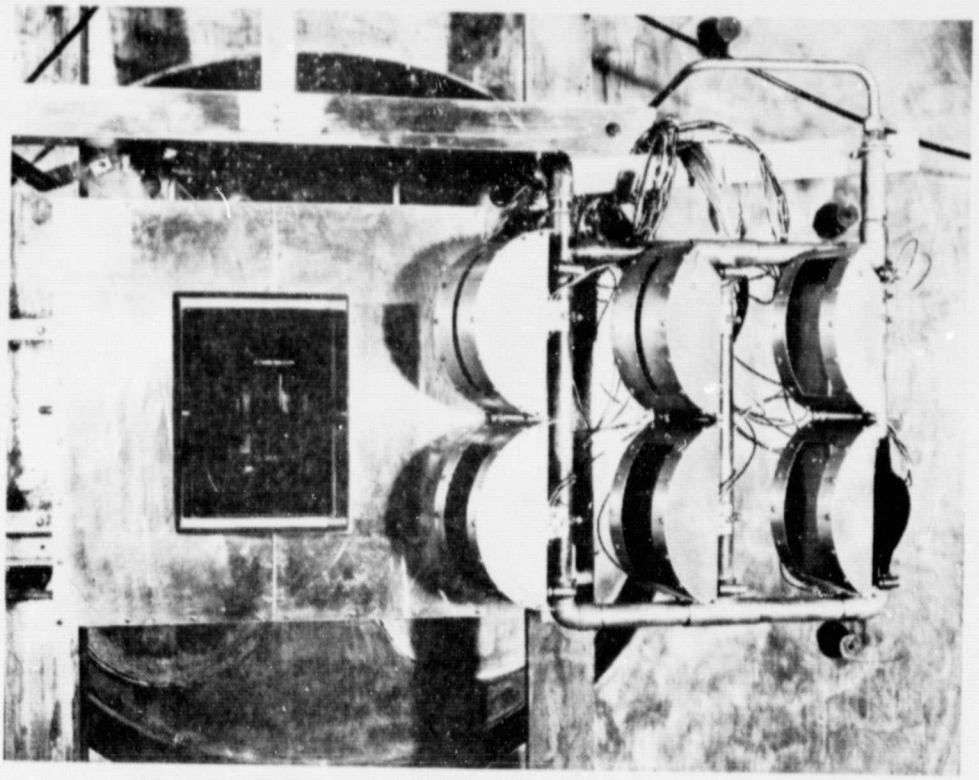

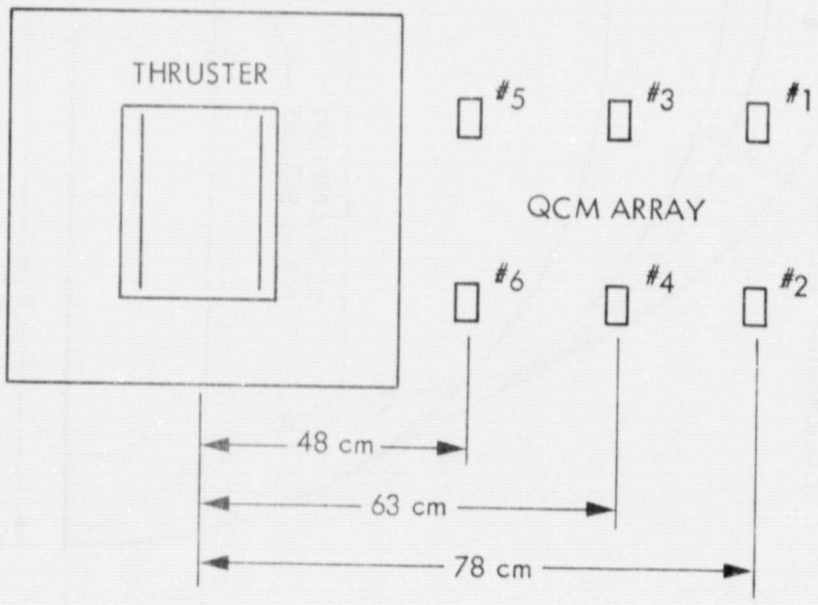

Figure 19. QCM Collimator SEP Facility Test Array

All the collimators were set to view along a line cutting the thruster axis at a dip angle of 60°. The two QCMs at each radial location were expected to be insensitive to their slightly different azimuthal positions due to the measured plume symmetry about the thruster axis. As will be seen, this assumption is acceptable within the error of the measurements. In Figure 19, QCM numbers 3 and 5 had the narrow 0° collimators while QCM numbers 1, 2, 4 and 6 had the 20° collimators.

In the SEP facility, the PPT thruster was fired downstream towards a large LN_2 cooled steel target at the end of the tank. This target can be rotated about a horizontal axis, perpendicular to the thruster axis, and thus, was used to vary the tank backscatter characteristics during the test. In addition, the QCM array was in place during the previously discussed plume Mylar target test, and data was taken during this test. The results of the QCM collimator testing are shown in Table II for the six QCMs and the various test conditions.

The positions and dip angle of the collimated QCMs were chosen to minimize the plume-wall backscatter effects on the observed data. In the SEP facility it is clearly impossible to eliminate the backscatter, and the data of Table II can be used to determine the magnitude of the backscatter effect. The data taken with the plume Mylar target in place is generally about a factor of two larger than the data taken without the target, indicating that a large fraction of the plume is being backscattered by this target. This backscatter increase is essentially independent of QCM collimator aperture angle, but does seem to increase with increasing QCM radial position. The downstream location of the Mylar target was chosen to be approximately at the location of the MOLTRAP

TABLE II. QCM SEP Facility Test Deposition Rates (μg/pulse)

Radius	78 cm		63 cm		48 cm	
Viewing Angle	20°	20°	0°	20°	0°	20°
QCM	#1	#2	#3	#4	#5	#6
Collector:						
Horizontal	6.9×10^{-4}	4.8×10^{-4}	1.7×10^{-4}	4.9×10^{-4}	2.4×10^{-4}	13.9×10^{-4}
45°	6.1×10^{-4}	4.2×10^{-4}	1.6×10^{-4}	4.4×10^{-4}	2.6×10^{-4}	14.2×10^{-4}
Vertical	-----	7.3×10^{-4}	-----	7.9×10^{-4}	-----	14.3×10^{-4}
Mylar Target	1.3×10^{-3}	1.3×10^{-3}	3.4×10^{-4}	8.2×10^{-4}	3.8×10^{-4}	-----

wall when the thruster is installed in the MOLSINK facility. As will be seen in the following sections, the measured backscatter in the MOLSINK facility, for otherwise identical conditions, is roughly a factor of five less than the Mylar target backscatter, indicating that the cryogenic-anechoic walls of the MOLTRAP do provide an improvement in the backscatter levels of the PPT thruster discharge.

Figure 20 shows a plot of QCM signal versus the tank target tilt angle for the various QCM radial locations. As can be seen, the data taken at the larger radii depends strongly on this tilt angle, indicating that, except for the data taken at 48 cm, the tank backscatter is affecting the QCM signals. This data also indicates that a target position of 45° minimizes the QCM signals and hence the wall backscatter. Figure 21 shows the QCM signals plotted versus radius for a target position of 45°. As can be seen, for smaller radii, where the plume-wall backscatter is presumably a minimum, the data drops with increasing radius. A comparison between the large and small collimator aperture angle data indicates the expected drop in signal as the aperture angle is reduced; however, the small aperture angle data is still well above of the QCM resolution, indicating that the 0° aperture can be used in the MOLSINK PPT thruster backflow measurements.

3.2 MOLSINK Test Configuration The PPT thruster was mounted in the MOLSINK facility in a manner identical to the installation of Phase I of this investigation, supported by a shaft entering the MOLTRAP through the upper MOLSINK doors. This shaft allowed the thruster to be rotated about its axis, so studies of the azimuthal plume behavior could be made. The thruster fired directly down to the

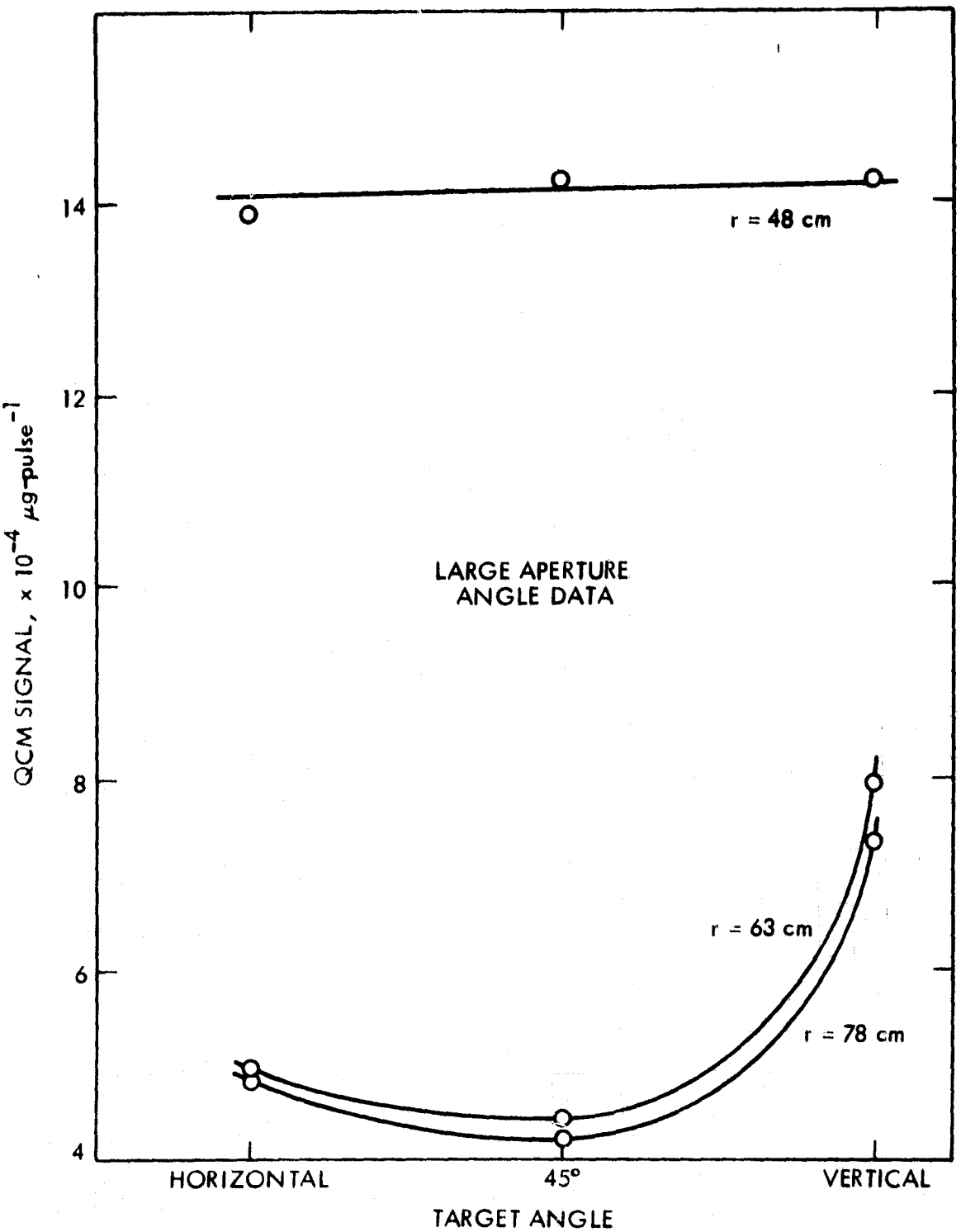

Figure 20. SEP Facility Target Backscatter

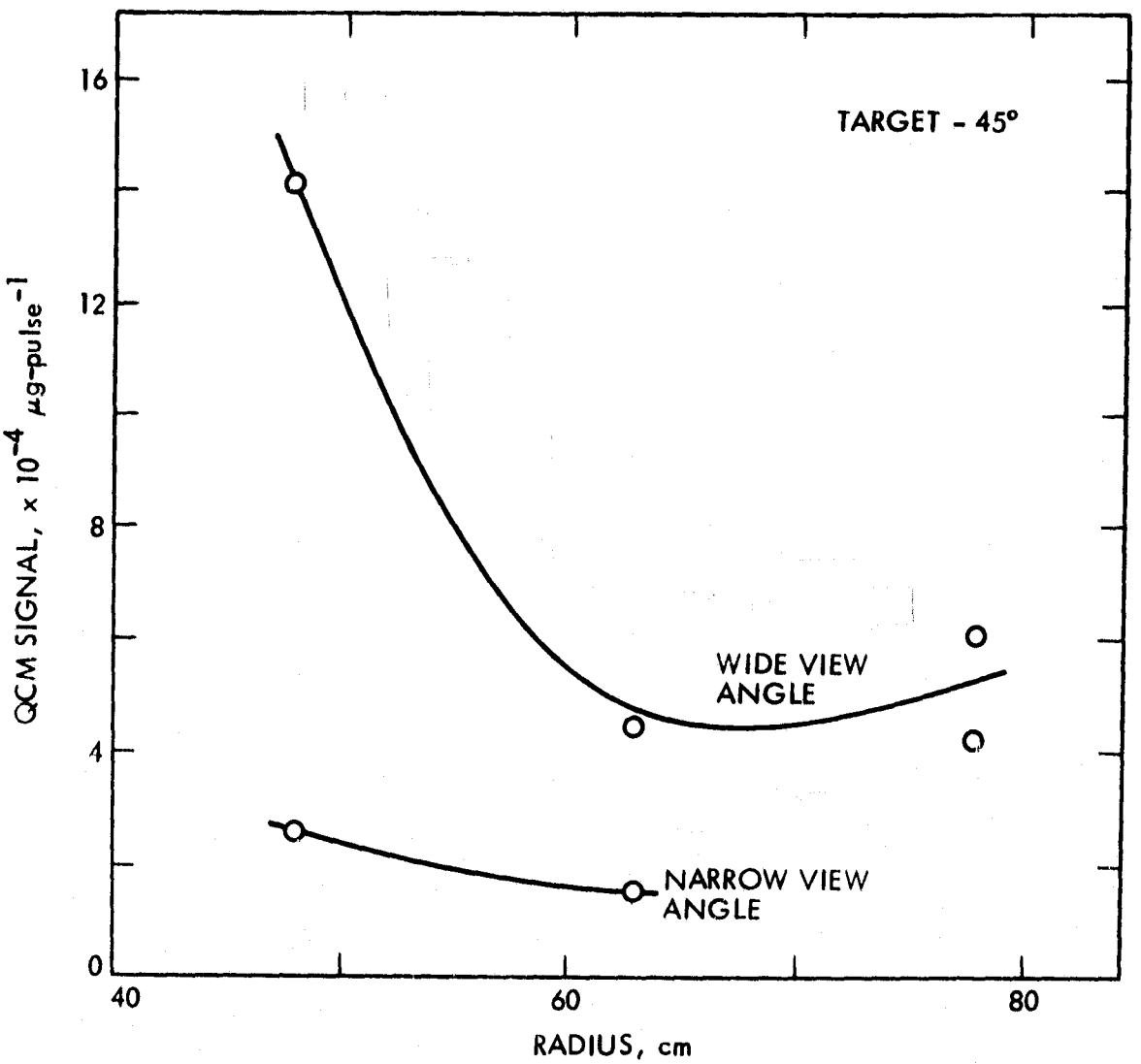

Figure 21. SEP Facility QCM Collimator Variation

lower MOLTRAP wall from the nozzle exit plane set 4.8 cm above the MOLTRAP horizontal midplane. The thruster power and control leads were fed into the MOLTRAP through the upper MOLSINK doors and down along the support shaft to the thruster.

Eight collimated QCMs were mounted in pairs, in four rows, 38 cm, 54 cm, 70 cm, and 86 cm from the thruster axis, respectively. A pair of QCMs was used at each radius to provide some redundancy in case of failure and to increase the measurement accuracy. Each pair was mounted perpendicular to an LN_2 cooled support pipe running radially outward from the thruster axis. A diagram of one collimated QCM pair is shown in Figure 22. The QCM collecting electrodes were placed 16.0 cm apart to leave room for the curved front faces of the collimators. A 0.8 cm square hole was cut in the QCM faceplates which were mounted rigidly to the QCMs. The collimators rotate about pivot points at their outer ends and are controlled via a linkage to the outside of the MOLSINK tank. The aperture angle was set at 0°; hence the total viewing angle including the penumbra is roughly 12°. The QCMs were rigidly mounted to the support pipe to prevent problems with movement of the electrical leads at low temperature and to provide adequate thermal conduction to the central LN_2 cooled support shaft. Because the normal to the QCM surface was fixed, while the collimator axis was free to rotate to various dip angles, a correction to the measured data is necessary. This correction consists of multiplying the measured QCM fluxes by the cosine of the angle between the QCM normal and the collimator axis, and accounts for the change in QCM collecting area perpendicular to the collimator axis.

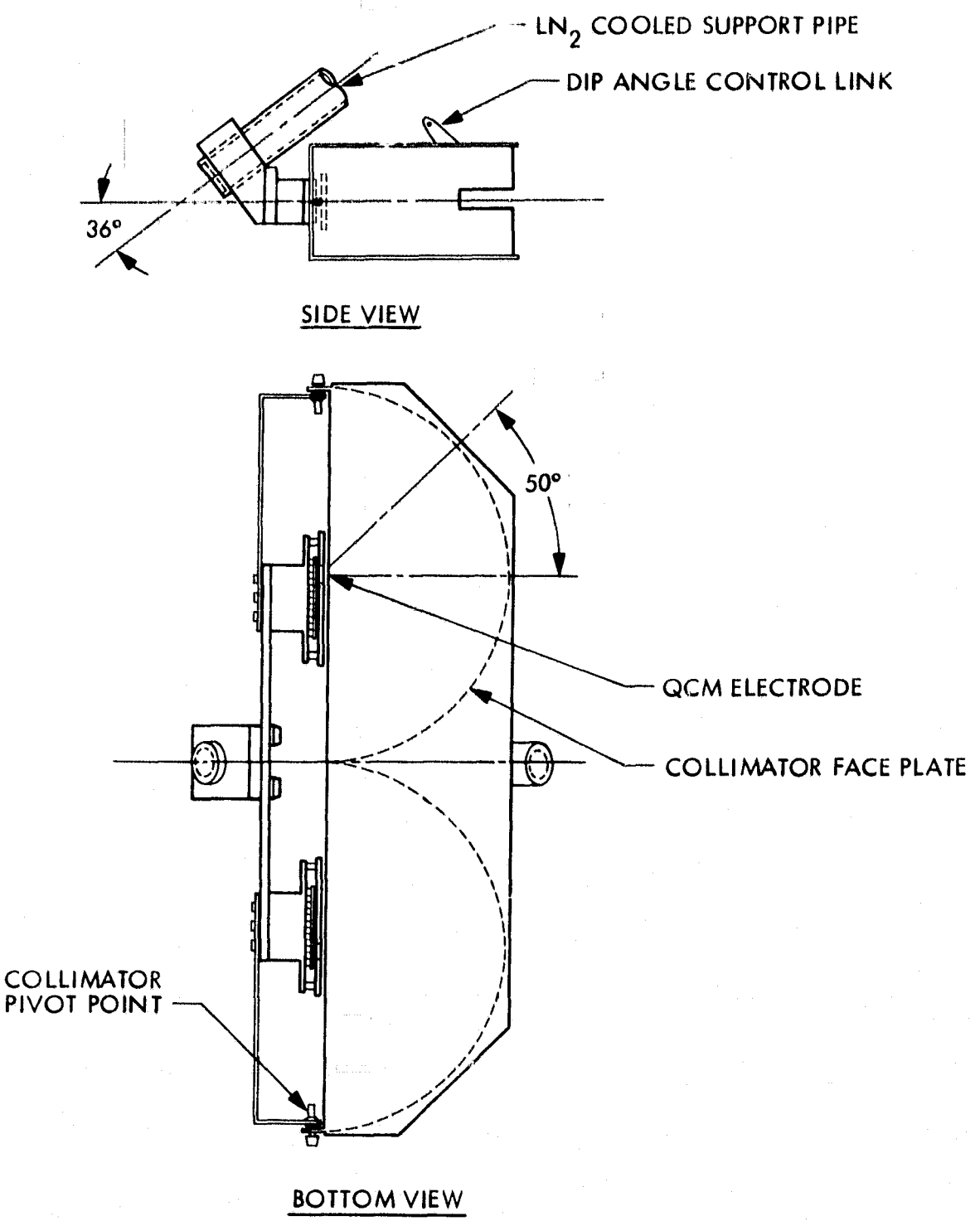

Figure 22. MOLSINK Collimated QCM Pair

Figures 23 and 24 show views of the completed array taken from the side and below; and from the side and above, respectively. The collimator apertures can be seen as 0.8 cm wide slits in the curved front faces of each collimator in Figure 23. Each QCM and its associated electronics box (mounted on white Teflon insulators) can be seen in Figure 24. Each QCM is shielded around the sides by Kapton sheet; however, for the photograph of Figure 24, the QCM on the far right is unshielded so that its mounting can be observed. Also in Figure 24, the linkages connecting the collimators together to control the dip angle can be seen. These linkages consist of 90° pivot arms connected with lengths of smaller diameter steel tubing. The main link connecting the collimators to outside the tank can be seen in Figure 24 extending up and out along the large diameter support pipe to the right of the picture. Using these linkages, the dip angle of the collimators in the array can be set anywhere between 0° and 60°.

Figure 25 shows a schematic of the QCM array mounted in the MOLSINK chamber. The plane of the array tilts downward away from the thruster at an angle of about 13°. This tilt is required so the outer radii collimators can see past the inner ones at small dip angles. The entire array is mounted on a slip ring tied to the central thruster support shaft above the thruster. This allows the array to move axially with respect to the thruster over a range of roughly 43 cm. The axial position of the array will be identified by the axial position of the QCM electrode face closest to the thruster, at a radius of 38 cm. This QCM can be positioned anywhere from 12 cm upstream to 31 cm downstream of the PPT nozzle exit plane.

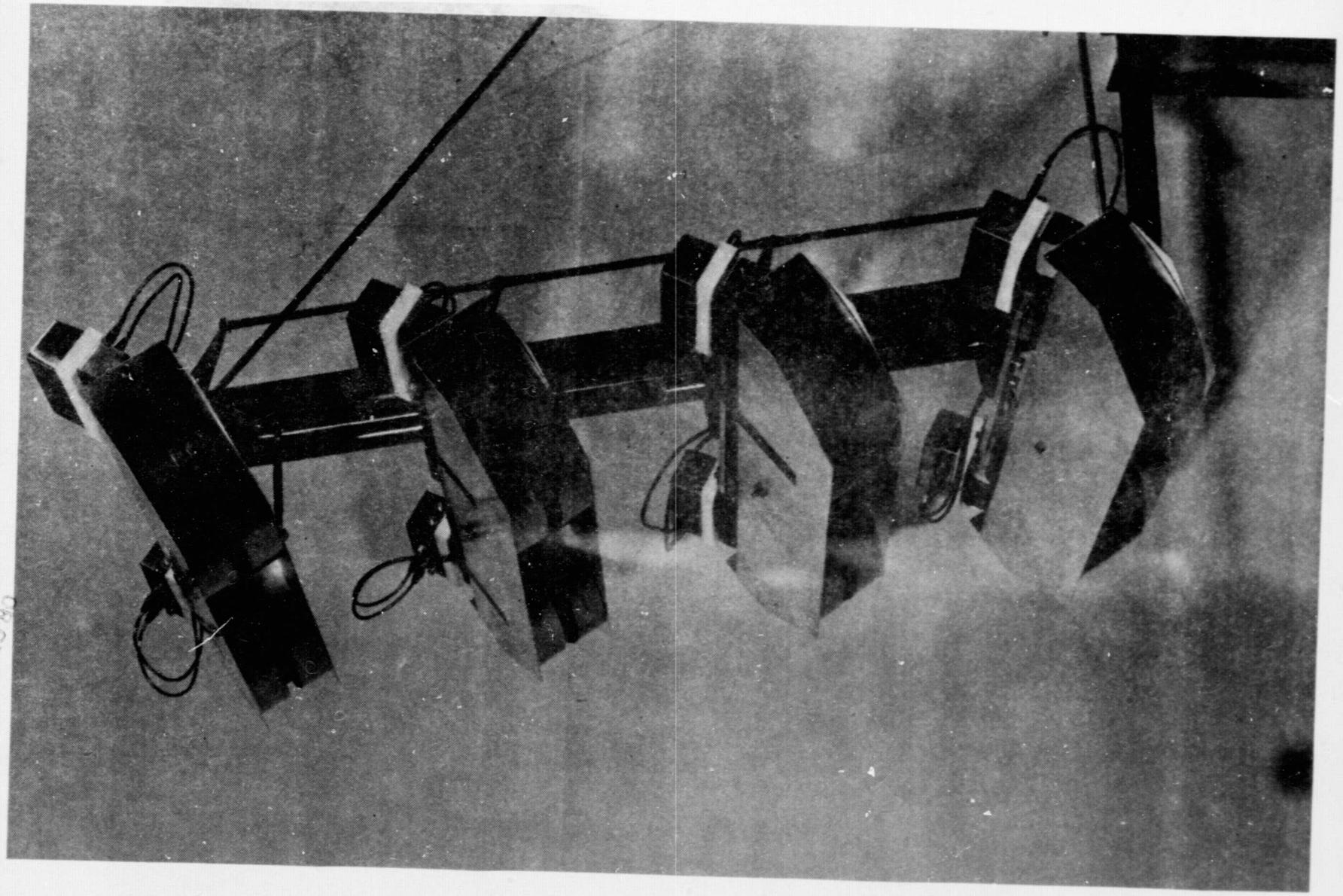

Figure 23. MOLSINK QCM Array Photograph - Below

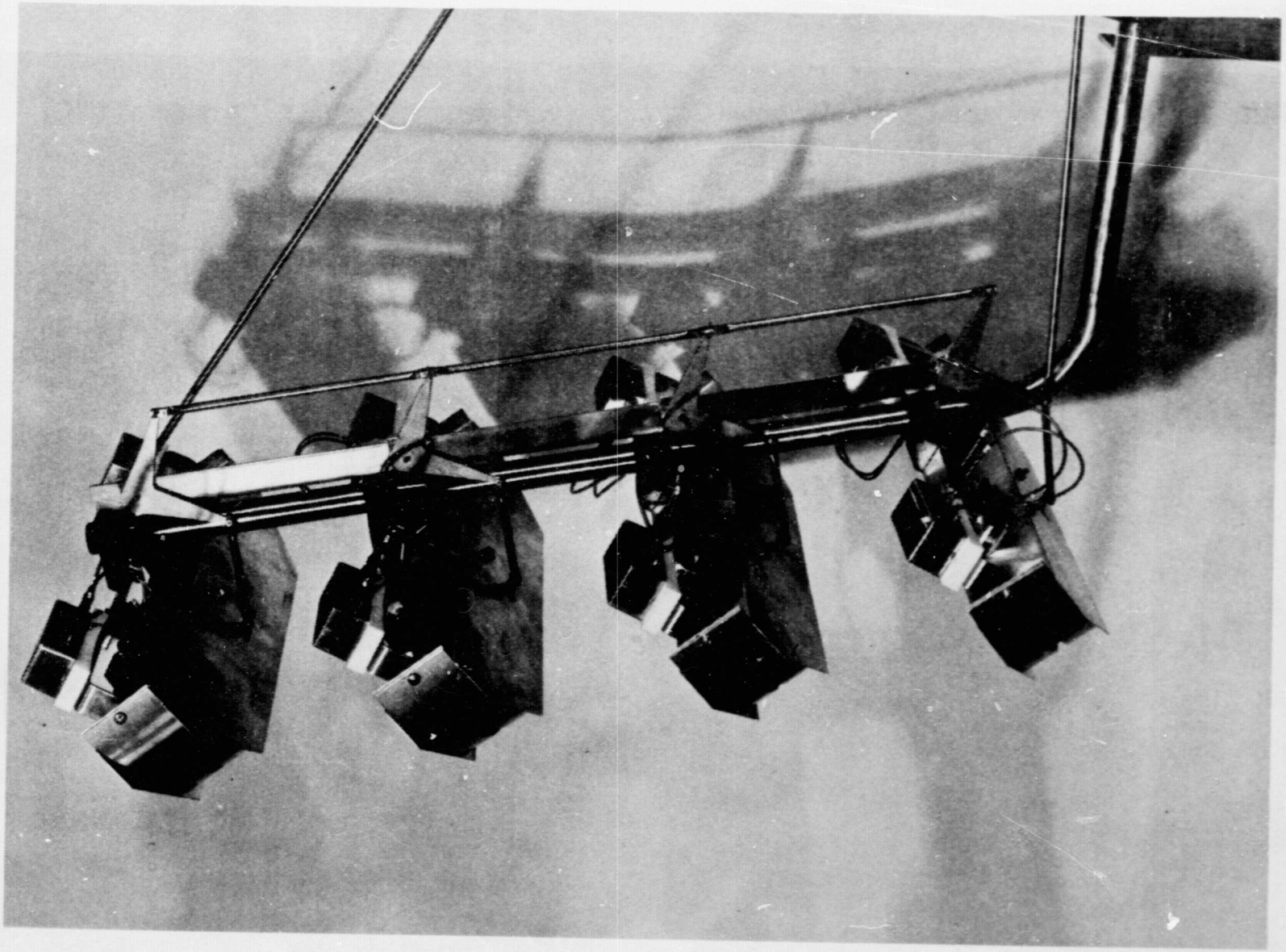

Figure 24. MOLSINK QCM Array Photograph - Above

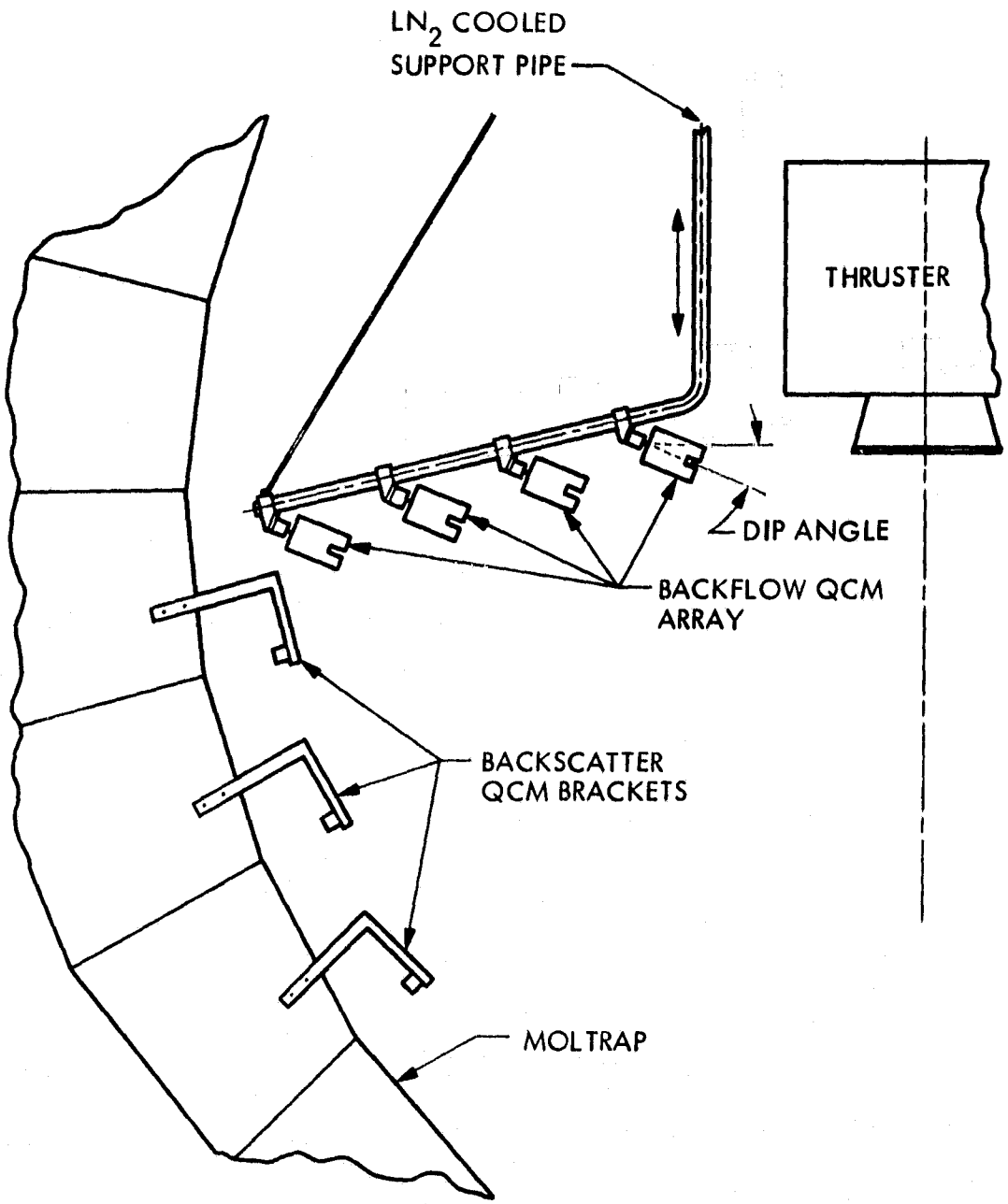

Figure 25. MOLSINK QCM Array Schematic

The LN_2 cooled support pipe for the QCM array has a smaller steel tube installed inside it, through which LN_2 is force fed to the lower end of the pipe. The LN_2 returns upward out of the tank through the annular space between the two tubes. Throughout the following experiments, this cooling system was used to maintain the array QCM temperatures at approximately -190°C. During the actual data taking phase, this temperature was kept constant to within ± 10°C, to insure that the QCM frequency shifts were not due to temperature fluctuations.

In order to accurately measure the total plume-wall backscatter over those areas of the MOLSINK wall observed by the array QCMs at small dip angles, three additional pairs of uncollimated QCMs were mounted on brackets on the MOLSINK wall. Figure 26 shows a photograph of one such bracket, which is L-shaped with a V-shaped cut in its vertical leg for mounting on a MOLTRAP fin. The fins in the MOLTRAP run vertically from the top to the bottom of the tank; hence, when installed, the QCMs on the bracket extend azimuthally away from the bracket's vertical leg, around the MOLTRAP and thruster axis. The front plate of the QCM itself has a 0.8 cm hole in it such that the QCM electrode observes the volume subtended by a 54° half angle cone around the electrode axis. The bracket cross-section was designed to provide adequate conduction cooling of the QCMs to the MOLTRAP wall. In fact, this cooling was great enough so that the QCMs had to be heated with their internal temperature regulating resistors in order to maintain an operating temperature of -190°C. Two QCMs were installed on each bracket to provide redundancy. As shown in Figure 25, the brackets were installed on the MOLTRAP wall at angles of 45°, 60° and 75° from the MOLTRAP axis, referenced from the tank center point.

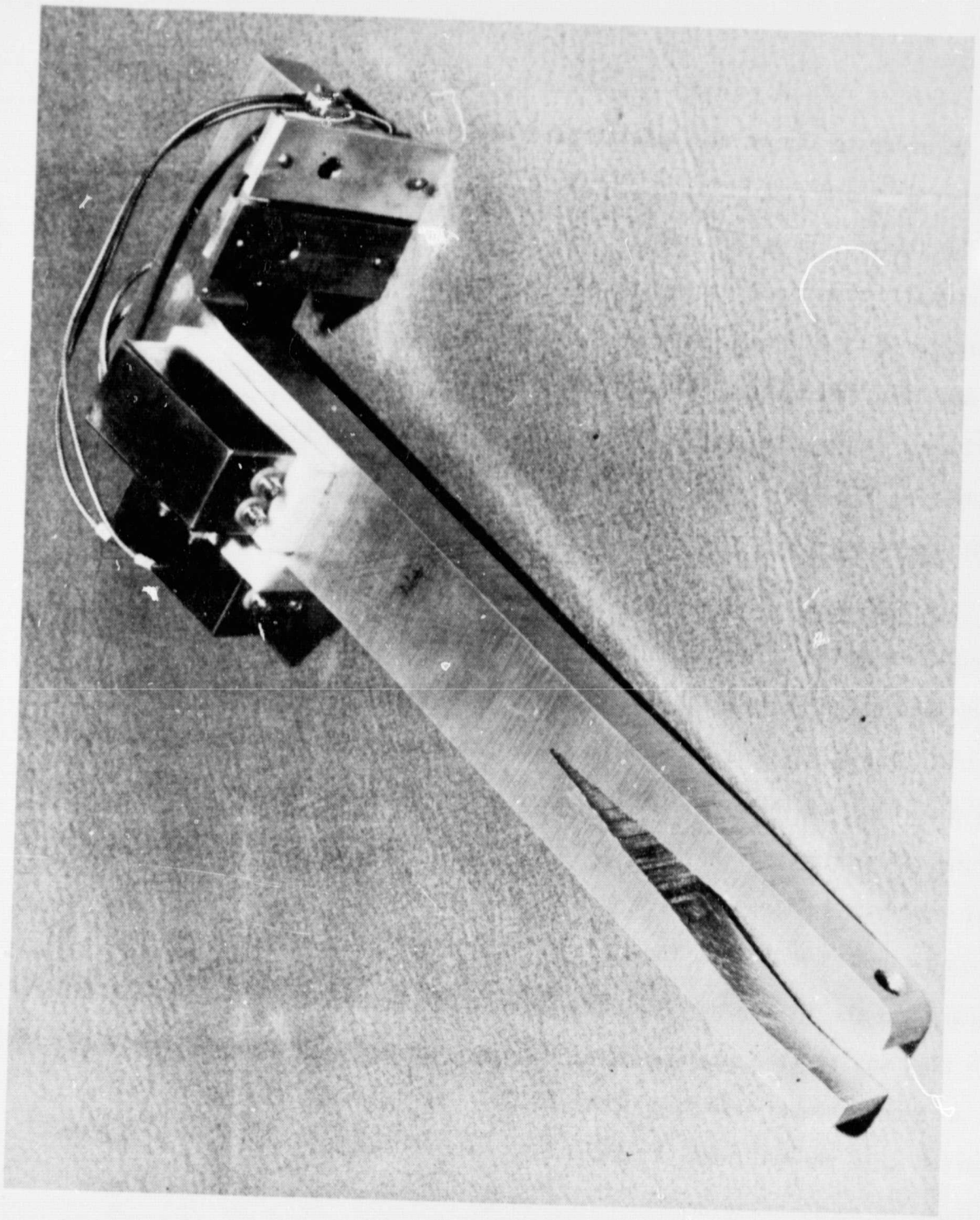

Figure 26. Backscatter QCM Bracket

In order to insure adequate temperature control of the test assembly, a number of thermocouples were placed in sensitive locations throughout the MOLTRAP volume. Each QCM and its associated electronics package was individually monitored, and if necessary, temperature regulated with feedback controllers. The internal temperature of the thruster was continually controlled and maintained at 20-26°C at all times to prevent the oil-filled capacitors from freezing. Finally, the lower MOLTRAP door was monitored to insure that the PPT plume did not materially affect the temperature at this location.

3.3 MOLSINK Backflow Test History The PPT plume backflow measurements using the previously described test set-up spanned a period of approximately three months, with over 700 hours of accumulated facility operation. A typical test sequence started with sealing the outer MOLSINK doors and pumping down both the inner and outer vacuum chambers to approximately 10^{-5} torr. During the entire process, the QCM electronics and the various thermocouples were continually monitored for acceptable operation. Once a low enough pressure was established, the LN_2 cooling of the guard vacuum walls was begun, and the inner chamber was isolated from the outer one. Finally, the gile flow was started, and the facility was allowed to come to thermal equilibrium at an inner chamber pressure of about 10^{-12} torr. The thruster was then started at a nominal rate of one pulse every 20 seconds, and the facility was allowed to equilibrate again at an average pressure somewhat greater than 10^{-12} torr. Attempts at measuring this average pressure using a vacuum discharge gauge failed due to the PPT discharge interference; however an

upper bound on this pressure was determined to be about 10^{-9} torr. Once the entire test set-up reached this equilibrium pressure and temperature, data was taken with the QCM diagnostics. Except for interruptions due to mechanical problems with the test set-up or the MOLSINK facility, the test was run continuously until sufficient data at all axial positions and collimator dip angles was accumulated.

Prior to the first backflow measurements and with the PPT thruster not operating, the output frequency stability of the test array QCMs was measured. With the thruster not operating, the QCM mass accumulation rates are zero; hence the output frequency should be constant with time except for drift due to temperature variations. This drift was monitored for a six hour period and was found to average less than 0.6 Hz for all the test QCMs. The worst drift was found to be 2.0 Hz; hence to insure the accuracy of the QCM mass accumulation measurements, the total frequency shift for each backflow data point should be greater than 10 times this value or about 20 Hz. The collected backflow data was measured over an exposure time sufficient to accumulate this minimum frequency shift, except when these times became impractically long.

Using the collimated QCM array, backflow data was taken at three axial locations, as measured by the axial position of the QCMs on the array closest to the thruster axis. These QCMs were positioned at 11.1 cm upstream, 2.54 cm downstream, and 30.5 cm downstream of the PPT nozzle exhaust plane. At each of the axial locations, data was taken at various dip angles from 0° to 60°. Some typical QCM output frequency signals are shown in Figures 27 and 28 versus observation time. Both the output frequency and time are

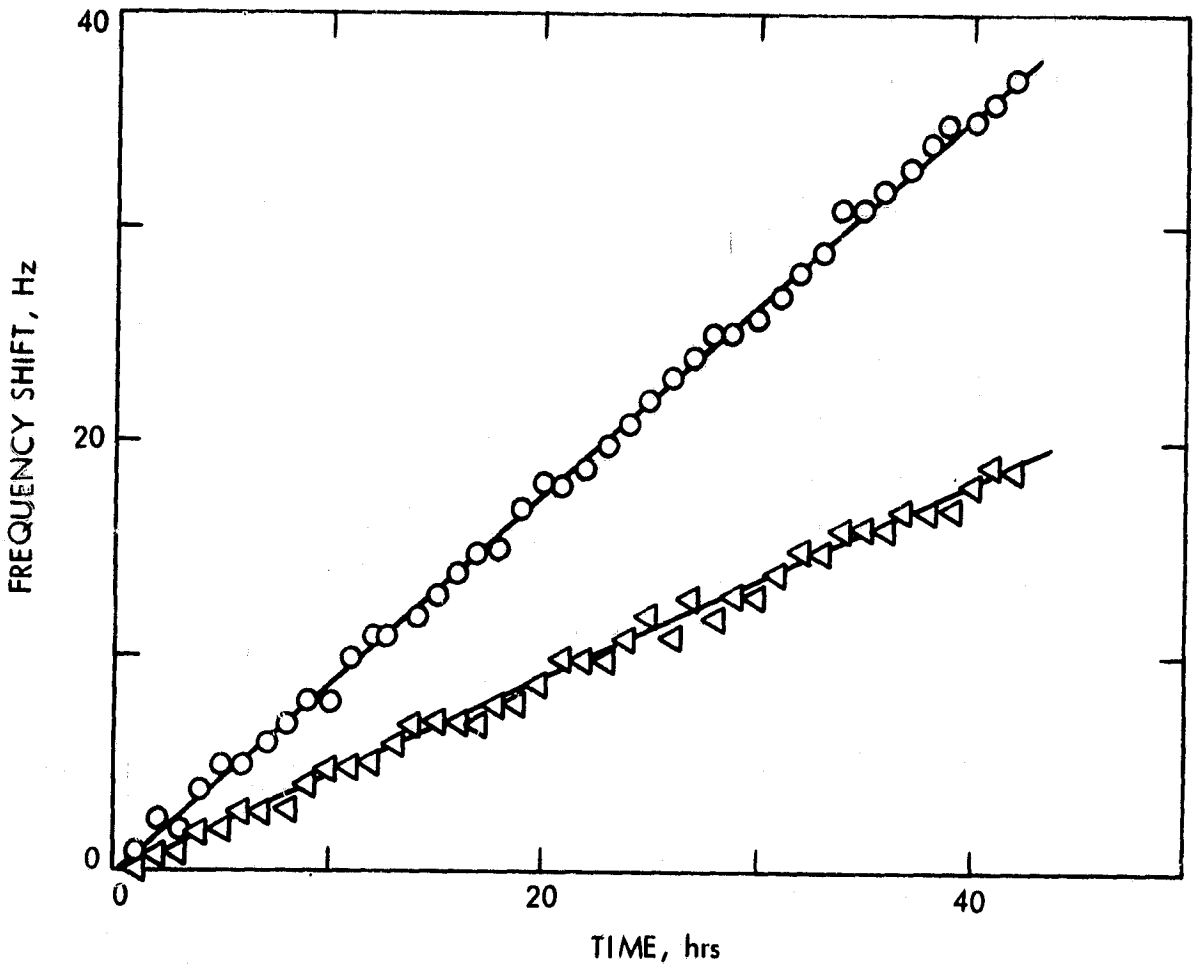

Figure 27. QCM Frequency Output - Good Correlation

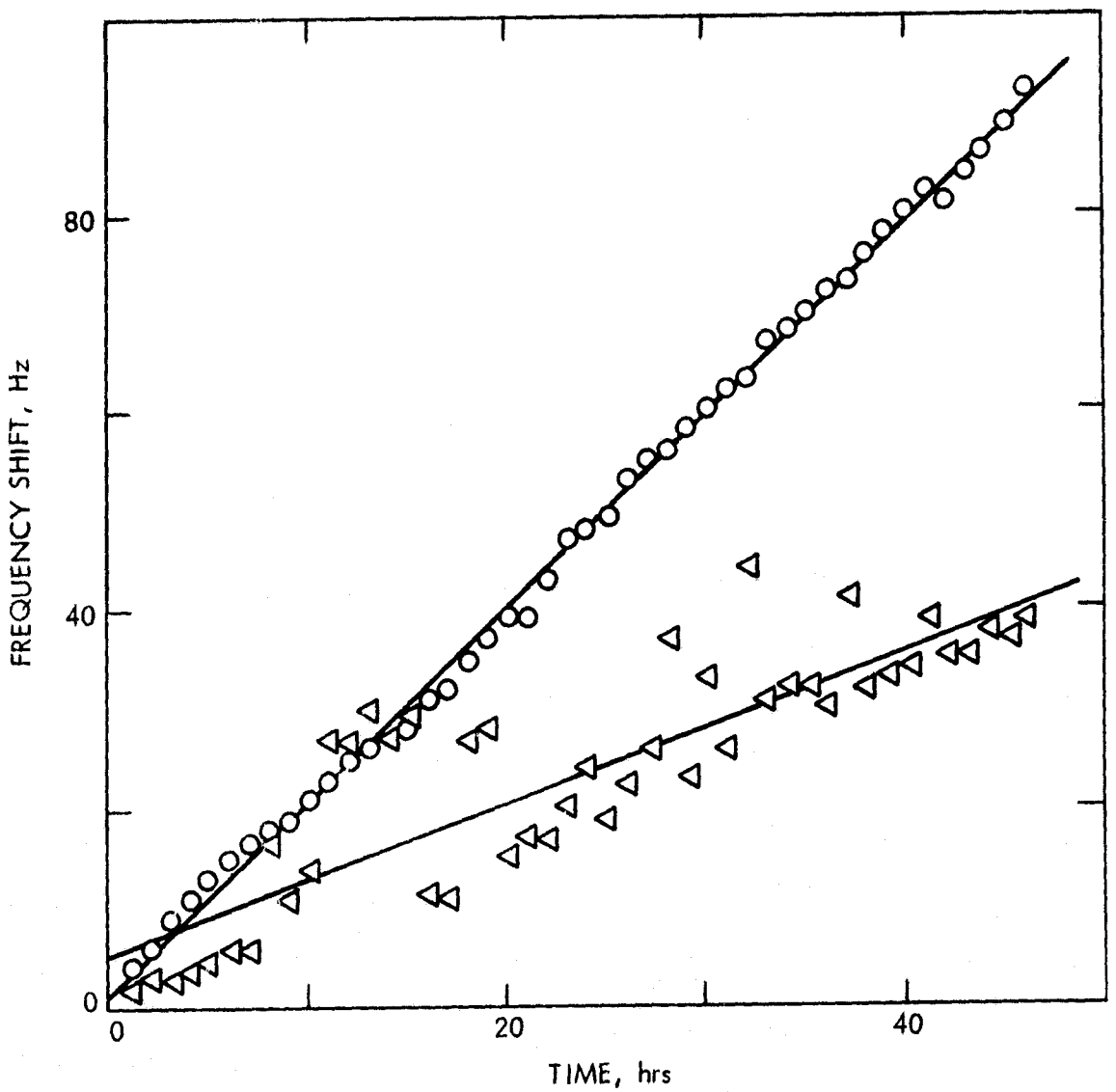

Figure 28. QCM Frequency Output - Poor Correlation

referenced to zero at the beginning of the particular observation. Figure 27 shows an example of typical data taken at either of the two downstream axial locations and for the large dip angles at the upstream location. The slopes of these data were calculated using a linear regression analysis and then used to calculate the QCM mass accumulation rates by multiplying them by the QCM calibration constant and dividing them by the thruster pulse rate. The error in the calculated slope of the data is equal to the square root of one minus the square of the linear regression coefficient ($\sqrt{1-r^2}$). For Figure 27 the correlation coefficients are around 0.999; hence the errors are very low. Although one of the data sets shown in Figure 28 is less accurate, the slope of these data is also estimated by a linear regression analysis, as before, except now the correlation coefficient is low and resulting error is large.

Once the QCM mass accumulation rates were found from the frequency shift data, they were corrected for the difference between the collimator dip angle and the QCM surface normal, as previously discussed. The final results are shown for the various axial positions and dip angles in Table III, along with their individual regression analysis correlation coefficients in parentheses. QCMs 1 and 2, 3 and 4, 5 and 6, and 7 and 8 are each at virtually identical locations and were expected to give identical results. As can be seen, the data from the individual QCMs in these pairs can vary by as much as 50%. This variation is not consistent, but in fact, changes with dip angle and axial location. Although the azimuthal separation between the QCM pairs is small, this may be the cause of the signal difference.

TABLE III. QCM Array Mass Fluxes (10^{-5} μg-cm^{-2}- pulse^{-1})

Axial Position	Dip Angle	Radius 38 cm		54 cm		70 cm		86 cm	
		1	2	3	4	5	6	7	8
30.5cm downstream	0°	203. (.992)	217. (.993)	21.9 (.984)	28.9 (.974)	9.56 (.920)	10.9 (.872)	30.9 (.936)	18.9 (.965)
	16°	179 (.998)	179 (.998)	38 (.992)	47.9 (.991)	29.5 (.986)	25 (.990)	35.3 (.992)	33.8 (.990)
	24°	114 (.998)	120 (.998)	26.8 (.996)	37.7 (.994)	16.7 (.994)	21.5 (.979)	31.8 (.995)	26.9 (.990)
	46°	80.9 (.998)	81.6 (.999)	44.0 (.996)	57.1 (.997)	24.1 (.983)	44.7 (.987)	43.7 (.994)	32.2 (.973)
2.54cm downstream	0°	20.8 (.998)	27.4 (.999)	4.7 (.995)	6.09 (.996)	1.43 (.944)	2.09 (.965)	3.76 (.989)	3.29 (.986)
	12°	13.8 (.999)	20.9 (.999)	8.0 (.998)	10.6 (.998)	3.57 (.991)	3.58 (.991)	5.63 (.997)	5.61 (.996)
	24°	10.9 (.998)	16.3 (.998)	6.53 (.997)	6.91 (.997)	3.42 (.996)	6.01 (.984)	7.5 (.999)	5.35 (.996)
	36°	8.92 (.999)	12.5 (.999)	5.85 (.998)	6.98 (.998)	4.58 (.997)	5.32 (.996)	9.05 (.999)	8.71 (.999)
	48°	8.21 (.998)	10.4 (.998)	6.33 (.996)	7.86 (.997)	5.46 (.995)	6.04 (.996)	10.9 (.998)	10.4 (.997)
	60°	9.73 (.970)	16.2 (.982)	7.36 (.948)	9.73 (.966)	4.86 (.894)	7.36 (.866)	14.9 (.986)	16.2 (.997)
11.1cm upstream	0°	.95 (.478)	10.8 (.945)	55.9 (.876)	26.3 (.923)	1.63 (.526)	30.7 (.853)	-.68 (.061	-10.4 (.654)
	18°	18.4 (.997)	17.3 (.998)	12.2 (.904)	17.0 (.982)	-	4.42 (.718)	10.5 (.965)	12.1 (.946)
	26°	19.9 (.998)	26.1 (.998)	13.4 (.841)	13.6 (.956)	5.3 (.806)	8.46 (.855)	7.82 (.855)	8.63 (.925)
	36°	18.2 (.999)	20.2 (.999)	9.2 (.904)	10.9 (.994)	-	6.63 (.890)	11.2 (.961)	12.1 (.975)
	60°	18.6 (.996)	17.8 (.998)	9.94 (.752)	13.5 (.980)	-	8.08 (.749)	17.5 (.931)	17.0 (.934)
11.1cm upstream	0°	7.02 (.998)	5.36 (.997)	10.6 (.984)	12.4 (.959)	-	4.91 (.811)	8.07 (.972)	8.87 (.877)
	12°	9.29 (.997)	7.32 (.998)	12.4 (.997)	12.3 (.976)	-	7.40 (.975)	9.99 (.997)	10.1 (.935)
	24°	23.2 (.999)	15.7 (.997)	11.0 (.998)	12.0 (.996)		6.32 (.994)	8.76 (.991)	8.65 (.986)
Thruster rotated 90°	36°	27.0 (.997)	20.9 (.992)	11.7 (.979)	12.5 (.998)	-	7.91 (.996)	11.7 (.996)	9.24 (994)
	60°	12.7 (.990)	10.8 (.960)	1.49 (.051)	5.72 (.348)	-	3.04 (.150)	14.9 (.718)	16.7 (.806)

To check this possibility and to determine if the measured backflow has any significant azimuthal dependence, data was taken for two thruster azimuthal locations separated by 90° for the upstream array axial position, as shown in Table III. Figure 29 shows the data taken from the QCM pair at the 38 cm radius plotted versus dip angle for the two thruster azimuthal positions. As can be seen, the different data points do not vary in a consistent manner, indicating that the scatter is primarily due to random variations in the measurements. The data taken at the remaining three radii, 54, 70, and 86 cm, behave in a similar manner and indicate that within the measurement error, the backflow is azimuthally uniform. Hence, the variation in data between each QCM of a given pair will be taken as due to random error, and the two signals will be averaged for the upcoming backflow analysis of Section 4.0.

During the backflow measurements of Table III, the plume-wall backscatter was monitored continually with the three QCM brackets shown in Figure 25. The data from these QCMs was found to be independent of the array axial position and QCM collimator dip angle, as it should be. More importantly, the data was also found to be independent of the thruster azimuthal position, as expected from the plume symmetry data of Section 2.0. The data taken with these QCMs is shown in Table IV, with respect to the bracket angular displacement from the MOLSINK center axis.

The second QCM at the angular position of 75° failed soon after test inception, so only one datum is available at this location. The data at the other two locations shows a self-consistency similar to that found with the collimated array QCMs, and thus will simply be averaged at each location for the final data analysis to follow.

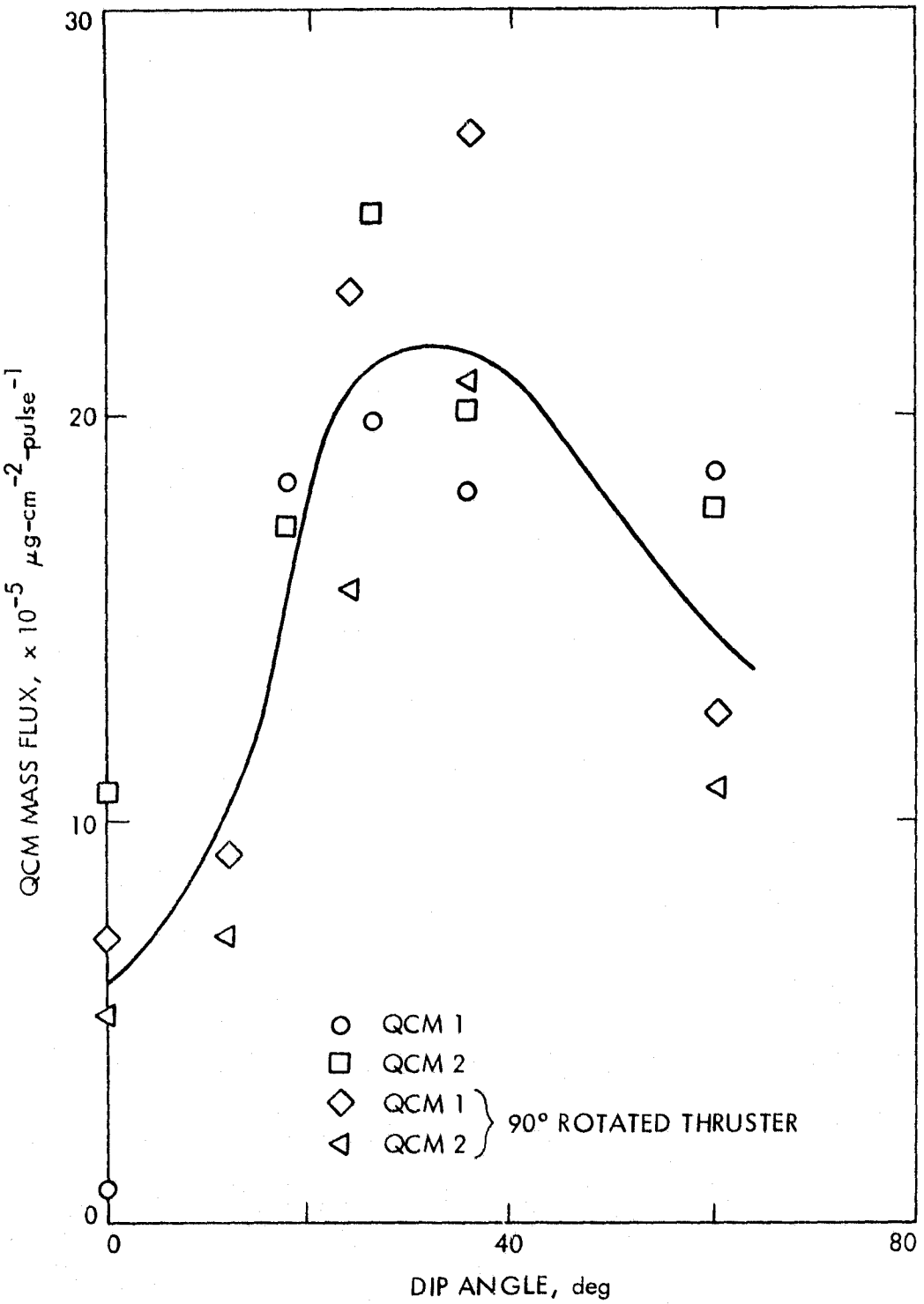

Figure 29. Backflow Flux Azimuthal Behavior

TABLE IV. Backscatter QCM Mass Fluxes

QCM bracket angle	Mass Flux ($\mu g\text{-}cm^{-2}\text{-}pulse^{-1}$)
45°	5.18×10^{-4}
45°	5.46×10^{-4}
60°	2.97×10^{-4}
60°	1.51×10^{-4}
75°	1.09×10^{-4}

3.4 Summary Based on the experience gained during the Phase I segment of the PPT plume characterization[6] and following a series of tests in the SEP vacuum facility, an array of collimated QCMs was designed and built to measure the PPT plume backflow. The quality of the design was evident in its trouble free operation at LN_2 temperatures and in the relative accuracy and consistency of the output data. Although this data behaves in a manner somewhat different than was expected (compare Figure 29 to Figure 1), the error bars on the data are small enough to determine approximate signal variations with array axial position and collimator dip angle (see Appendix 1). In general, these variations indicate that at greater axial distances upstream of, and at greater radial distances away from the thruster nozzle exit area, the QCM signals decrease. In addition, these signals generally increase with dip angle at differing rates, presumably depending on the relative dominance of the plume backflow or the plume-wall backscatter. Further interpretation of the data must await the more detailed analysis of the next section to more fully distinguish between these two sources of QCM signal.

4.0 BACKFLOW TEST DATA ANALYSIS AND MODELING

During the design and operation of the collimated QCMs described in the previous section, the ultimate requirement for a relatively complex analytical reduction of the data was always considered. The use of a collimator to separate out the effects of the plume-wall backscatter leads to the requirement that, for useful results, the geometric effects of the collimator must be removed from the measured data. In addition, the contribution of the plume-wall backscatter must be estimated to insure adequate resolution of the actual plume backflow. Using this analytically corrected data, the total backflow flux through a representative area was calculated by integrating the data over the collimator dip angle. Finally, an attempt was made to reduce the data to the form of a scattering source function in the thruster plume. It was hoped that this source function could be used to extrapolate the calculated backflow fluxes to regions outside of the measurement area.

4.1 Wall Backscatter Correction Since it has been concluded that scattering from the plume has near azimuthal symmetry, the average signals from the side-by-side mounted QCM pairs are used for this analysis. The pairs are located at distances 38, 54, 70 and 86 cm from the PPT plume centerline and are labeled A, B, C, and D, respectively. The position of pair A relative to the PPT exit plane is z_a, while succeeding pairs are each offset 3.6 cm downstream relative to their preceding pair (see Appendix 2). The results of the wall backscatter measurements are considered by calculating upper bound corrections (assuming no attenuation) to the array QCM signals. Let the position on the elliptical tank wall be given by the angle Ψ from the tank and PPT centerline (Figure 30).

$$I_w = k \exp\left(-\frac{\psi}{17^\circ}\right) \cos\theta$$

$$k = 9.78 \times 10^{-3}\ \mu g/\text{pulse cm}^2\text{ster}$$

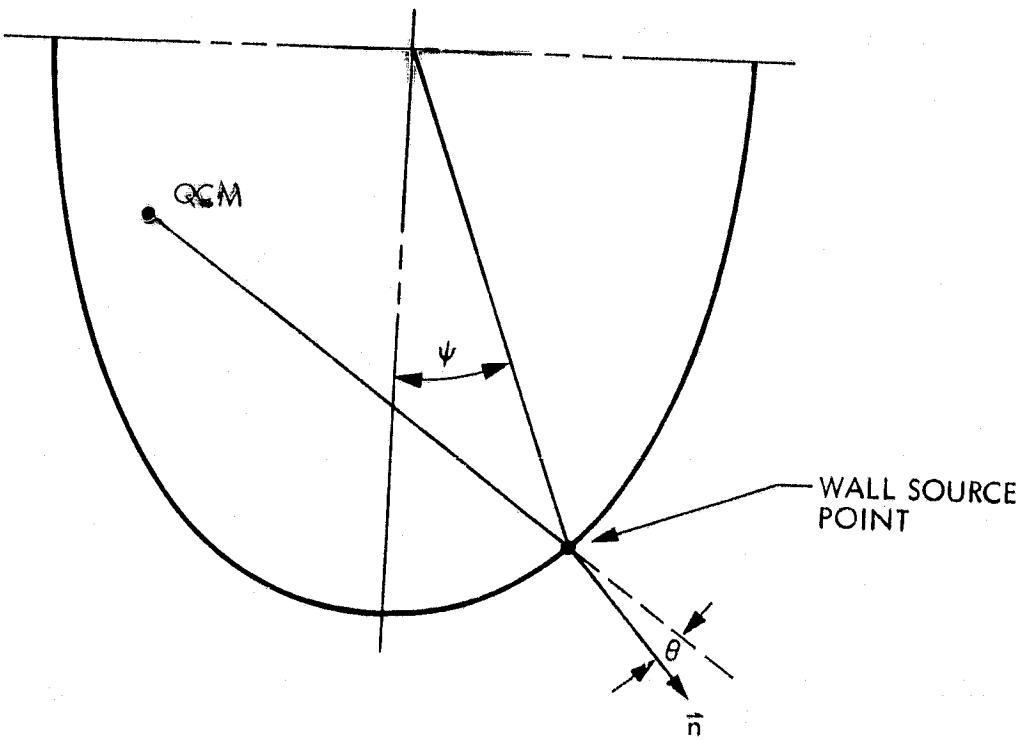

Figure 30. Wall Scattering Model

The wall scattering is assumed to vary as the cosine of the angle, θ, from the wall normal; reduction of wall QCM signals to intensities is discussed in Appendix 3. The wall QCMs were placed at ψ=45°,60°, and 75°; and the measured results are presented in Figure 31. The normal intensity varies exponentially with respect to the angle ψ. (The plume center value indicated by the intersection of the straight line of Figure 31 with ψ=0 is consistent with the Phase I measurement.) The wall intensity as given in the figure is used as an input source to calculate the array QCM signal contributions assuming that all the particles leaving the wall in the direction of a given QCM reach it. Details of the effect of QCM geometry and location on this calculation are found in Appendix 4. The array QCM pair data and upper bound wall backscatter corrections are presented in Table V. For dip angles greater than 40°, the upper bound correction is considerably larger than the QCM signal. This means that there must be considerable attenuation of the backscattered wall flux (by nearly an order of magnitude) and that collisional effects in the plume are important. Since the attenuation is an unknown, that part of the QCM signal due to plume backflow (total signal minus wall backscatter) cannot be known for the larger dip angles. Only QCM signals whose upper bound corrections are comparable to or less than the signal may be treated as plume backflow. This reduces the total number of useful data by about 20%.

4.2 Backflow Flux Collimator Correction and Integration The QCM signal results from collection of particles over a solid angle defined by the aperture of the collimator and over an area defined by the opening in the back of the collimator. Division of signals (in mass rate) by the solid angle-area product gives their intensities. Total flux through a reference plane can be estimated by integration over angle of the product of intensity and the cosine of the angle between the

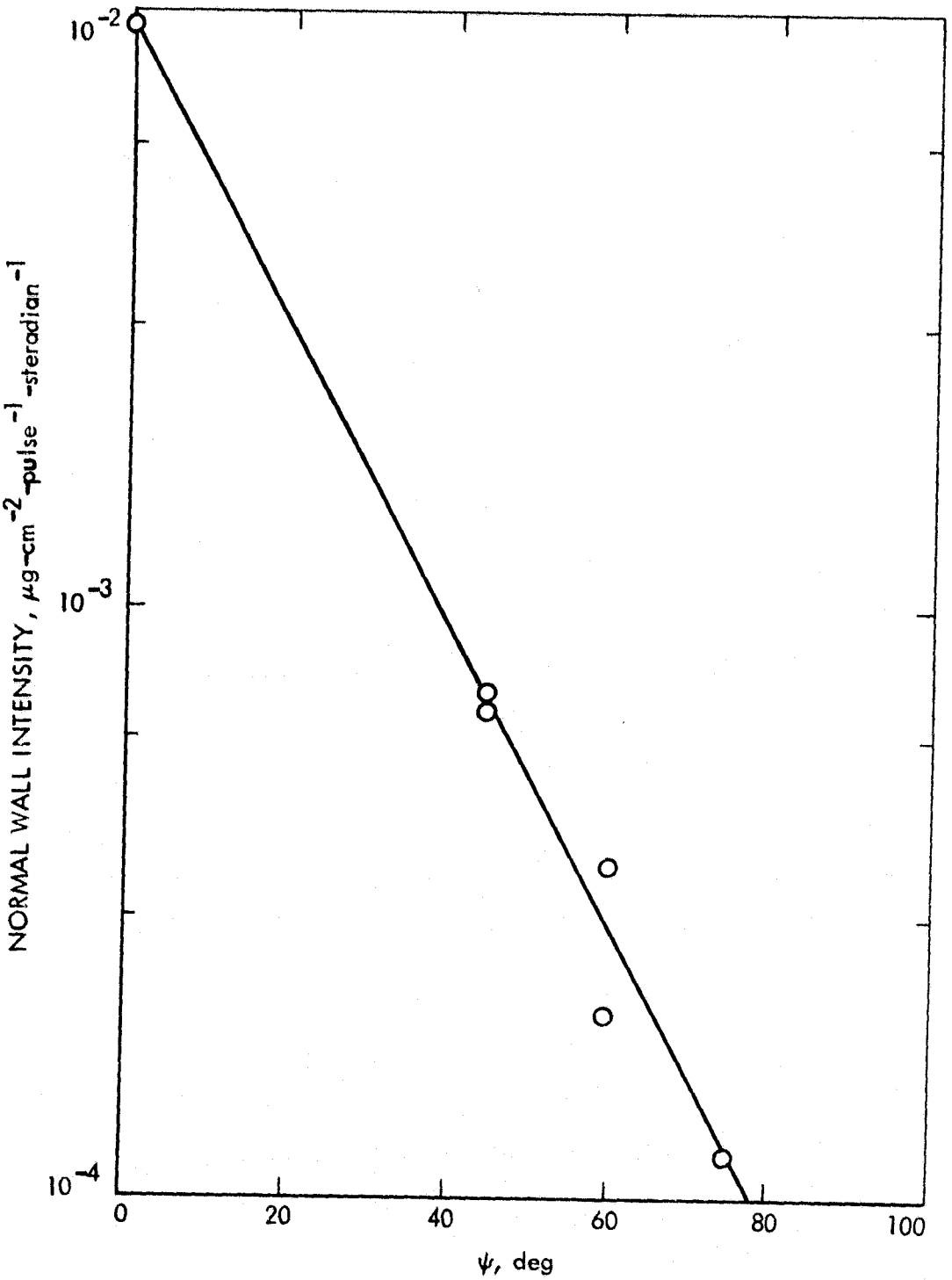

Figure 31. Wall Scattering Intensity

TABLE V. QCM Array Mass Fluxes and Backscatter Corrections

Data Point	Z_a(cm)	Dip Angle (°)	QCM Pair	QCM Signal $\frac{\mu g}{(Pulse)}$	Correction $\frac{\mu g}{(Pulse)}$
1	-11.1	18	A	7.18E-5	6.55E-6
2		18	B	5.89E-5	8.25E-6
3		18	C	1.78E-5	1.05E-5
4		18	D	4.56E-5	1.30E-5
5		26	A	9.27E-5	1.15E-5
6		26	B	5.44E-5	1.53E-5
7		26	C	2.77E-5	1.97E-5
8		26	D	3.31E-5	2.52E-5
9		36	A	7.54E-5	2.25E-5
10		36	B	3.97E-5	3.02E-5
11		36	C	2.61E-5	3.95E-5
12		36	D	4.56E-5	5.07E-5
13		60	A	5.89E-5	7.76E-5
14		60	B	3.79E-5	1.00E-4
15		60	C	2.61E-5	1.25E-4
16		60	D	5.56E-5	1.35E-4
17	2.54	0	A	8.91E-5	2.06E-6
18		0	B	2.00E-5	2.76E-6
19		0	C	6.53E-6	3.29E-6
20		0	D	1.31E-5	3.90E-6
21		12	A	6.85E-5	6.62E-6
22		12	B	3.68E-5	7.96E-6
23		12	C	1.41E-5	9.70E-6
24		12	D	2.22E-5	1.17E-5
25		24	A	5.48E-5	1.49E-5
26		24	B	2.71E-5	1.94E-5
27		24	C	1.90E-5	2.45E-5
29		36	A	4.19E-5	3.13E-5
30		36	B	2.52E-5	4.11E-5
31		36	C	1.95E-5	5.30E-5
32		36	D	3.50E-5	6.70E-5
33		48	A	3.59E-5	5.79E-5
34		48	B	2.76E-5	7.60E-5
35		48	C	2.24E-5	9.71E-5
36		48	D	4.15E-5	1.20E-4
37		60	A	4.19E-5	9.33E-5
38		60	B	2.76E-5	1.19E-4
39		60	C	1.98E-5	1.45E-4
40		60	D	5.04E-5	1.42E-4

TABLE V. (cont'd)

Data Point	Z_a(cm)	Dip Angle (°)	QCM Pair	QCM Signal $\frac{\mu g}{(Pulse)}$	Correction $\frac{\mu g}{(Pulse)}$
41	30.5	0	A	7.74E-4	6.92E-6
42		0	B	9.40E-5	7.64E-6
43		0	C	3.79E-5	8.58E-6
44		0	D	9.23E-5	9.73E-6
45		16	A	7.18E-4	2.01E-5
46		16	B	1.72E-4	2.45E-5
47		16	C	1.09E-4	2.97E-5
48		16	D	1.38E-4	3.57E-5
49		24	A	4.72E-4	3.19E-5
50		24	B	1.30E-4	4.01E-5
51		24	C	7.70E-5	4.95E-5
52		24	D	1.18E-4	6.03E-5
53		40	A	3.14E-4	6.94E-5
54		40	B	1.95E-4	8.87E-5
55		40	C	1.33E-4	1.11E-4
56		40	D	1.47E-4	1.36E-4

intensity direction and plane normal. This procedure is detailed in the following discussion. Since intensity variations transverse to the plume are not determined by use of the slit collimator geometry, only variations with respect to the dip angle can be calculated. Details are given in Appendix 5. The slit admission angle is 0.1 radian or 5.73°. Transverse-mean intensities ($\mu g\text{-pulse}^{-1}\text{-cm}^{-2}\text{-rad}^{-1}$) are given in Table VI (QCM location and dip angle may be found in Table V). Normal fluxes through a plane parallel to the QCM array holder which tilts at an angle of 12.7° are estimated (Figure 32). The angle α=(12.7 + dip angle) is that from the plane surface and sin α is equal to the cosine of the angle from the normal, thus the partial flux

$$F(\alpha) = \int_0^{\alpha} I(\alpha) \sin\alpha \; d\alpha$$

where I is obtained from Table VI. Plots of the integrand and a similar expression with the upper bound wall backscatter correction included are given in Figure 33 for a typical QCM position. For this case, the uncertainties in net plume backscatter do not permit integration beyond an angle α_{max} of about 45° . Partial fluxes and the associated values of α_{max} are listed in Table VII. Values were obtained by graphical integration. It was noted that in the range $25° \lesssim \alpha \lesssim 50°$, partial flux F varied approximately as α^2 for those cases of larger α_{max}. This behavior suggests that the partial integrals for small α_{max} may be extrapolated to larger α_{max} values. A least square curve fit of the form

$$F = k(\alpha_{max})^2/r^p$$

with axial variations removed through division by the r=54 cm values gives p≈2.

TABLE VI. Backflow Intensities

Data Point	Intensity ($\mu g\text{-pulse}^{-1}\text{-cm}^{-2}\text{-rad}^{-1}$)
1	1.79E-3
2	1.47E-3
3	4.43E-4
4	1.13E-3
5	2.30E-3
6	1.35E-3
7	6.88E-4
8	8.22E-
9	1.92E-3
10	1.01E-3
11	6.66E-4
12	1.16E-3
17	2.39E-3
18	5.37E-4
19	1.75E-4
20	3.52E-4
21	1.73E-3
22	9.28E-4
23	3.56E-4
24	5.60E-4
25	1.36E-3
26	6.72E-4
27	4.71E-4
28	6.43E-4
29	1.07E-3
30	6.43E-4
31	4.97E-4
32	8.93E-4
41	2.08E-2
42	2.52E-3
43	1.02E-3
44	2.48E-3
45	1.79E-2
46	4.29E-3
47	2.72E-3
48	3.44E-3
49	1.17E-2
50	3.23E-3
51	1.91E-3
52	2.93E-3
53	8.17E-3
54	5.07E-3
55	3.46E-3
56	3.82E-3

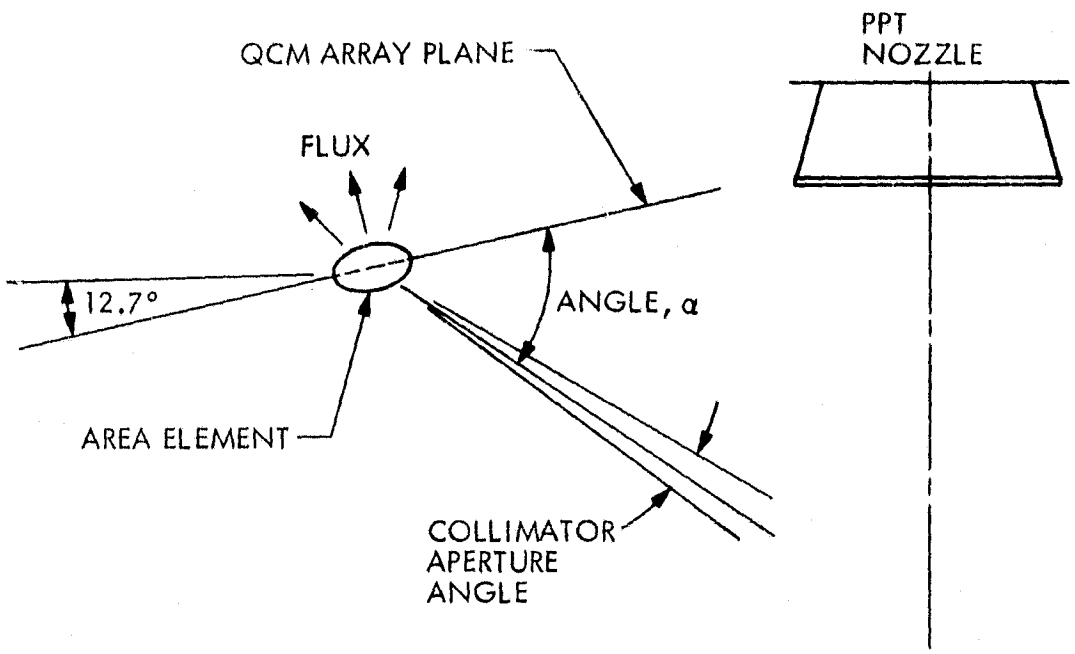

Figure 32. Backflow Integration

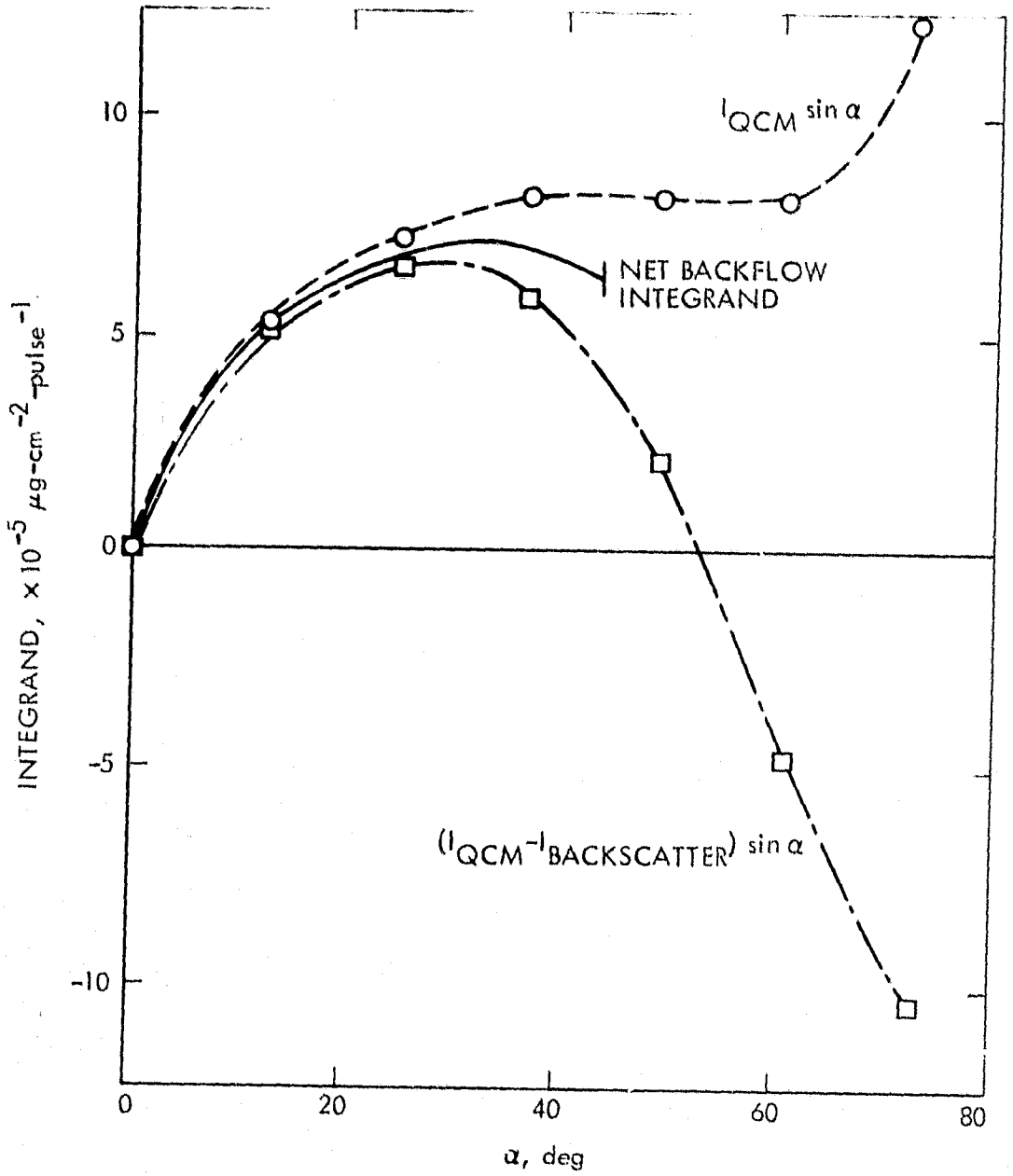

Figure 33. Backflow Integrand

TABLE VII. Plume Backflow Results (X 10^{-4} μg-cm^{-2}-$pulse^{-1}$)

(α_{max})

Array Axial Position	QCM Radius			
	38 cm	54 cm	70 cm	86 cm
30.5 cm Downstream	54 (54°)	15 (54°)	3.4 (36°)	5.1 (36°)
2.5 cm Downstream	4.2 (44°)	1.2 (34°)	.12 (22°)	.33 (26°)
11.1 cm Upstream	6.3 (54°)	4.4 (45°)	.83 (30°)	1.4 (36°)

(The flux at r-38 cm for the upstream position is probably low due to partial screening by the PPT). Using p=2, the coefficient k(z) can be estimated. Results are (α in degrees):

Axial Position z_a (cm)	k (μg-$pulse^{-1}$-$degree^{-2}$)	Standard Deviation (μg-$pulse^{-1}$-$degree^{-2}$)
30.5	2.09×10^{-3}	8.2×10^{-4}
2.5	2.75×10^{-4}	1.0×10^{-4}
-11.1	5.49×10^{-4}	2.1×10^{-4}

For each position the RMS error is slightly below 40%. The rough fit gives consistently high fluxes at r=70 cm and consistently low fluxes at r= 86. Using the above k to remove the mean axial dependence of the partial fluxes and using

the assumed α^2 variation to shift the fluxes to α_{max}=50° values, the radial dependence and data scatter are shown in Figure 34. Although another radial dependence could give a slightly better fit, it is felt that inaccuracies in the data and in the extrapolation procedure do not make a more stringent curve fit necessary or desirable.

The plume expansion angle is approximately 35° , thus the direction parallel to the plume boundary is approximately α=140° , giving I=0 for $\alpha \gtrsim 140°$. It may be expected that the intensity drops to small values at somewhat smaller values of α and that its maximum is somewhere in the region $\alpha = 50°$ or slightly larger. Intensity plots support this conclusion. Total fluxes may be estimated by multiplying the α_{max}= 50° values by a factor of two or three.

4.3 Source Function Studies A limited attempt has been made to numerically estimate the plume source function needed to duplicate the measured intensities. A simple model based on a linear combination of source elements is assumed. The QCM readings can then be represented as a known vector, equal to the product of an influence matrix containing QCM and source geometry effects and an unknown source coefficient vector. The source vector can be found by a powerful generalized matrix inversion technique known as singular value analysis. Unfortunately, the linear source model was found to be inadequate in that there was a marked tendency towards partially negative sources. Also, a volume source distribution in the plume was, at best, not very accurate. (This is not too surprising since the model does not explicitly consider attenuation, which has been found to be important for wall scattering fluxes.) Nevertheless, the attempt produced

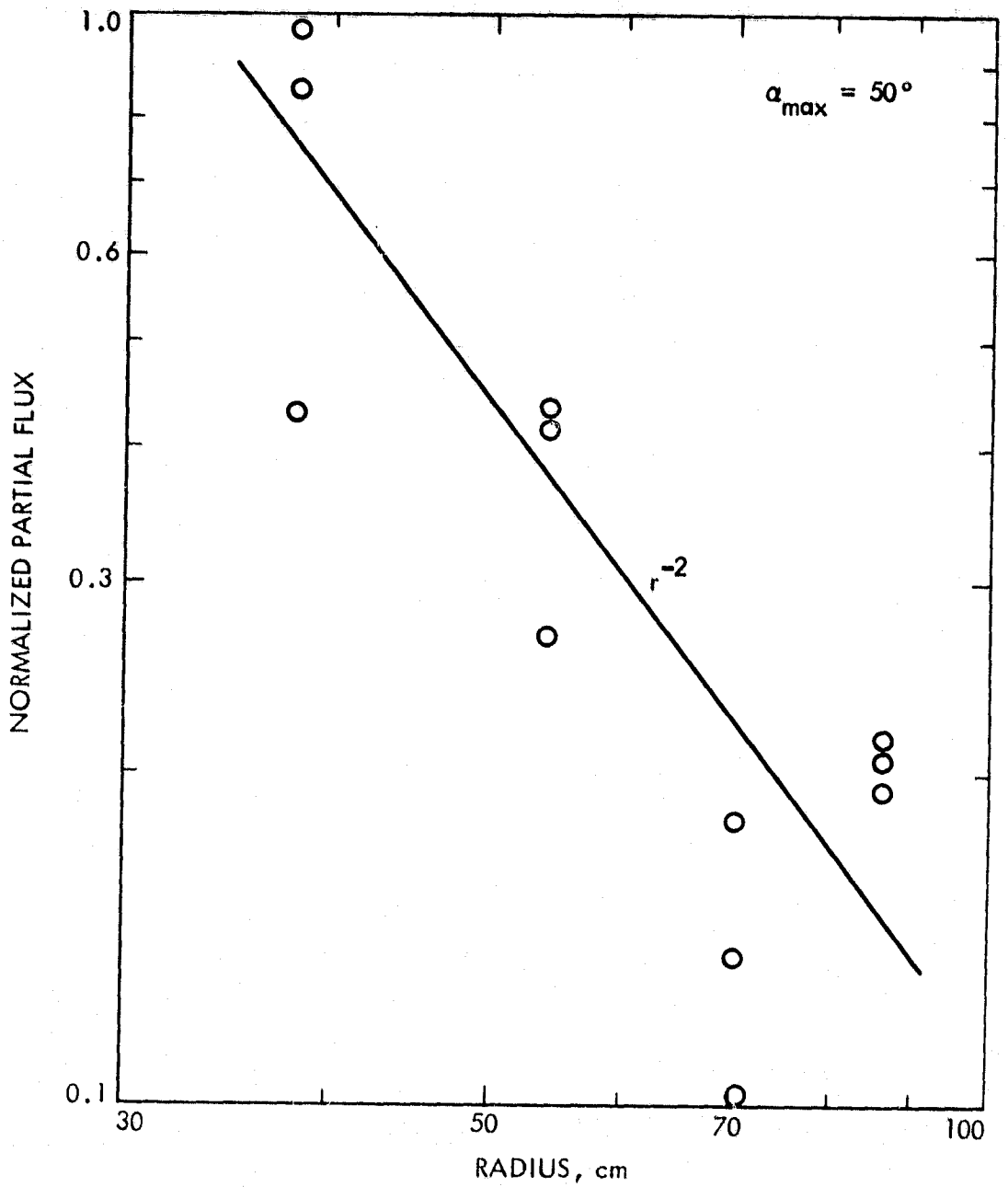

Figure 34. Backflow Flux Radial Profile

some qualitative information and indicated the type of approach necessary for a possible source calculation. The model and its results are described briefly.

A given source element (volume or surface) may be totally unscreened from the collector opening by the QCM aperture slit, or may be partially screened, or may be totally screened from the QCM collector. The corresponding viewing regions of the QCM collimator are labeled illuminato, penumbra and umbra (see Figure 16). For the second case of the penumbra, the collecting area is the overlap of the collector opening and aperture projection on the QCM plane, Figure 35. Calculation of the area involves considerable algebra; details are given in Appendix 4. The source element is assumed to contribute to a QCM signal an amount proportional to the element strength times the solid angle of the collecting area relative to the element. The first effort assumed constant, isotropic sources in rings of given radial and axial intervals (for example, Figure 36 shows a cross-section of 30 such rings). An influence matrix element describes the net effect of a given ring of unit strength on a particular QCM. This is calculated by dividing the ring into small pieces of size $\Delta r \times \Delta\theta \times \Delta z$, calculating the collecting solid angle of the centroid of each piece, and summing the calculations over all volume pieces. Denote the QCM signal by R, source strength by S, solid angle by Ω, volume by V, then

$$R_i = \sum_j M_{ij} S_j, \quad i \geq j,$$

$$M_{ij} = \int d\Omega_i \, dV_j = \sum_{\Delta V} \Delta\Omega_i \, \Delta V_j .$$

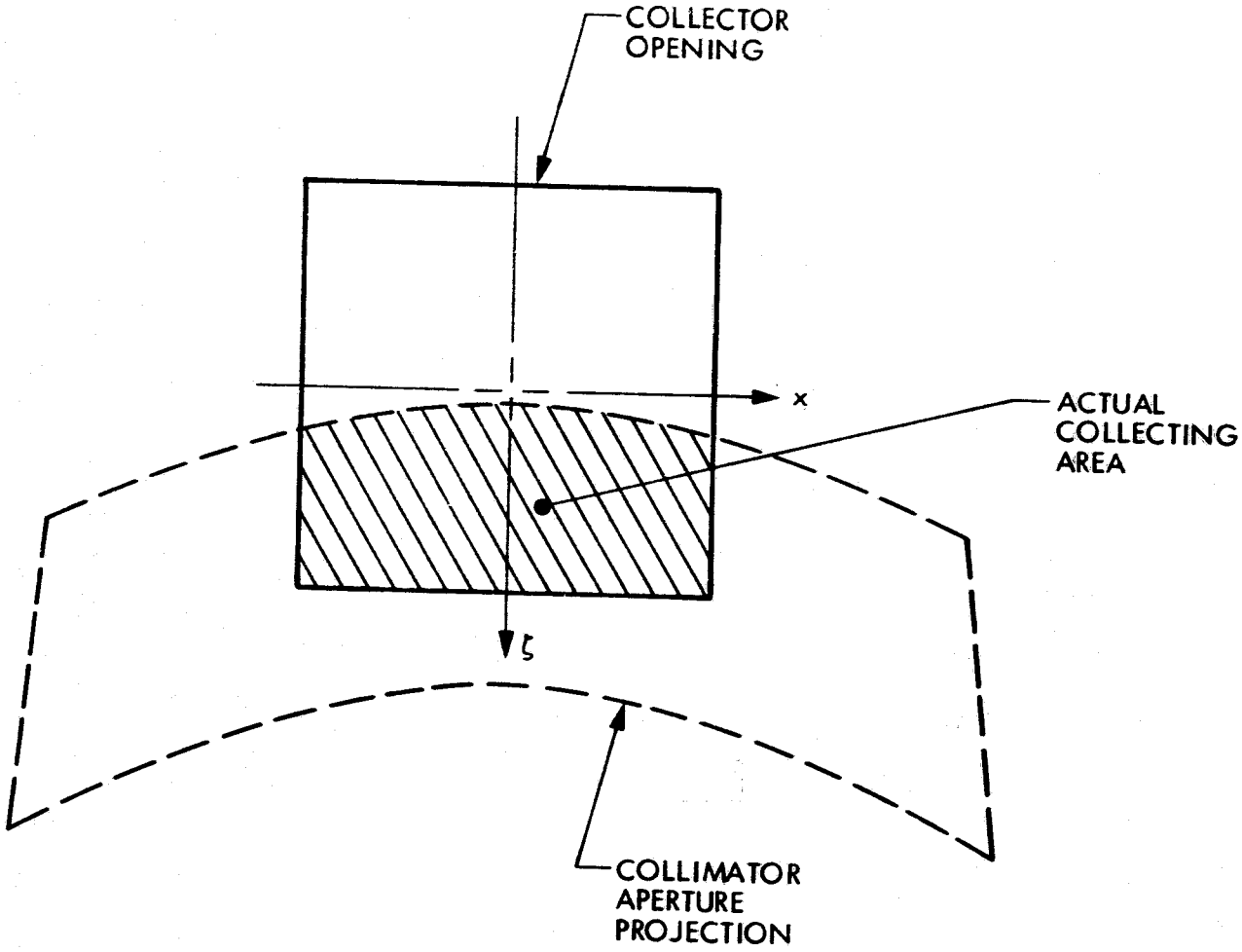

Figure 35. QCM Plane Area Geometry

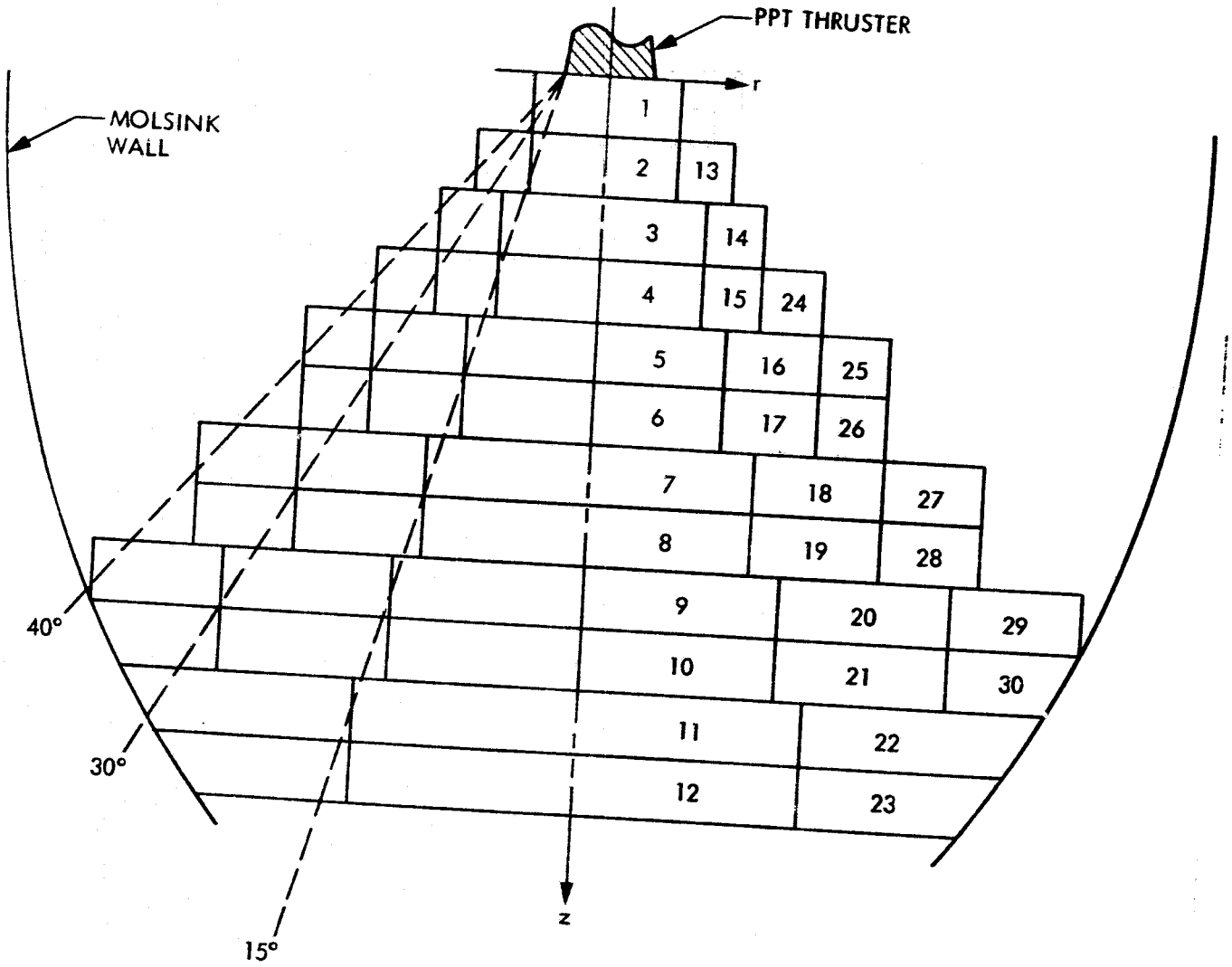

Figure 36. Ring Volume Source Geometry

The S-vector is to be found as a least square fit, i.e., to minimize the residue defined as $\Sigma_i \ (R_i - \Sigma_j \ M_{ij} S_j)^2$. This is done by decomposing matrix M into

$$[M] = [U] \ [D] \ [V]^T$$

where U and V are orthogonal matrices of eigenvectors of $[M] \ [M]^T$ and $[M]^T[M]$, respectively, and D is a diagonal matrix of nonincreasing quantities known as the singular values of M. Then

$$(S) = [V] \ [D]^{-1}[U]^T(R)$$

is easily found. The ratio of the first (largest) singular value to smallest nonzero value is the condition number for M. If the log of this number is larger than the number of significant digits in the input matrix, the smallest value represents numerical noise and should be nulled. A study of the behavior of the residues of the sequence of solutions obtained by successively nulling ever larger singular values enables one to make judgments on the accuracy of the input and to select the proper solution vector from this sequence. Singular value analysis can be used to handle ill-conditioned matrices; this capability was found necessary for this particular problem.

The calculated source functions were invariably negative for the larger radii rings in the plume. Best results were for narrow (plume angle 15° or less) sources with only an axial variation and with QCM signals normalized to unity (relative fit). Minimum deviations were larger than 100% RMS. This is probably due to attenuation effects in the actual situation.

Since attenuation seemed important, a second effort to calculate a source distribution was made by assuming a surface source near the PPT plume edge (see Figure 37). The source flux vector was defined in a coordinate system made up of a surface normal vector, $\vec{n}$, a surface vector through the source cone

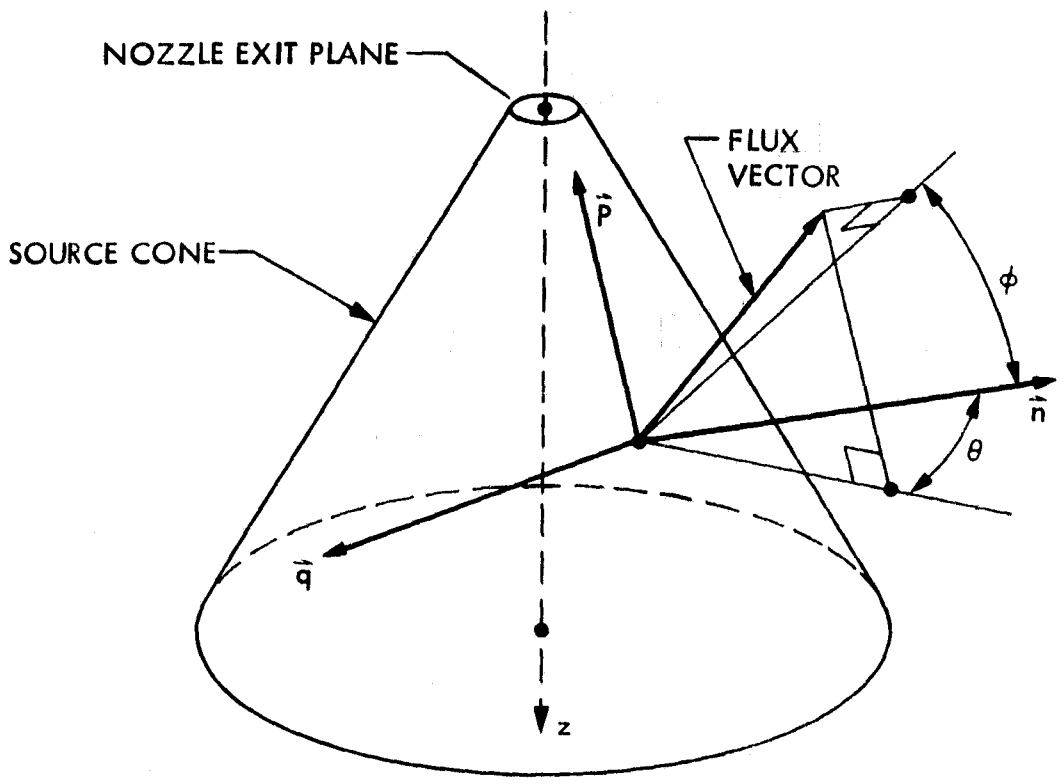

Figure 37. Surface Source Cone Geometry

vertex, $\vec{p}$, and a surface tangent vector, $\vec{q}$, in the $\vec{n} \times \vec{p}$ direction. Quadratic variation with respect to axial distance and direction angles (θ,ϕ) was assumed. Although a fit with as low as 25% RMS error was possible, again the problem of a partially negative source distribution occurred.

The results indicate that if any further attempt at a source calculation be made, then a nonlinear procedure should be adopted. A surface source function should be chosen dependent on position, direction, angles, and parameters a, b, c, .. such that it is nonnegative for all values of the parameters (nonlinear in parameters). QCM signals result by integration over solid angle and surface. The value of the parameters may be found by finding a minima of the residue using Newton's method. The difficulties that may be expected with this method are:

(1) Selection of the form of the source function. There is little physical basis for a selection procedure.

(2) Selection of initial values of the parameters. Particular initial values may yield a local minima but not a global one.

(3) Stability of the calculation.

4.4 Summary The relative complexity of the previous analysis is due in part to the planned sacrifice of analytical simplicity in favor of experimental simplicity. Several experimental design features were corrected for in this analysis, including the use of slotted two-dimensional collimators and fixed QCMs mounted separately from the collimators. Despite these complexities and the error bars on the experimental data, a reasonable estimate of the total plume backflow from the plume region close to the thruster was obtained. Throughout the analysis, conservative assumptions were made where necessary, in order to arrive at an estimate of the backflow which, at worst, is too large. Although the attempts at modeling this backflow in terms of a distributed source met with little success, a possible method was identified which may prove feasible with further study.

5.0 NOZZLE DESIGN STUDY

The existing rectangular ceramic nozzle on the PPT was designed to help control the radiated EMI from the discharge and to minimally interfere with the plume flow[13]. The results of the plume studies of section 2.0 suggest that the PPT plume has a large component of neutral species, which would be unaffected by the electric and magnetic fields of the discharge. The expansion of this neutral plume component downstream of the discharge chamber may be strongly affected by the nozzle design; and hence an appropriate nozzle may serve to reduce the neutral plume backflow. To determine if this hypothesis is correct, a new nozzle was designed, installed on the thruster, and tested in the MOLSINK facility with the collimated QCM array for any changes in the plume backflow between it and the original nozzle.

One of the primary difficulties with using QCMs to measure the mass flux rates in the PPT plume is in their inability to resolve the plume mass flux versus time during a single discharge pulse. In addition, some questions exist as to the accuracy of the QCM measurement (see Appendix 1); and hence it would be desirable to have an alternate method of measuring the plume mass fluxes as a way of corroborating the QCM results. One possible method which may prove useful is the use of Faraday cups to measure the charged particle flux in the plume. During the testing of the new nozzle in the MOLSINK facility, a Faraday cup was installed, and its usefulness and accuracy in measuring the PPT plume were assessed.

5.1 Nozzle Design, Installation and Test The original nozzle on the PPT expands at a half-angle of about 15° to a final exit area of approximately

11.5 x 16.5 cm. A straight segment of about 1 cm in effective length is mounted at the plume exit to provide mechanical reinforcement of the nozzle joints which are simply epoxied together. To minimize the ablation of the nozzle surfaces, the nozzle was fabricated from a high temperature ceramic (Mykroy).

Based on the measured plume expansion angle of 30-40° (see section 2.0), the new nozzle was designed to expand at a half-angle of 30° in both the vertical and horizontal directions out of the PPT discharge chamber. This new nozzle will hereafter be referred to as the 30° nozzle. The final exit area of this nozzle is a rectangle 19.6 cm wide by 25.6 cm high, giving it an area roughly twice that of the original nozzle. This larger area was intended to expand the plume neutral component to a pressure more nearly equal to the vacuum environment, and hence reduce the backflow around the nozzle exit. Figure 38 shows two cutaway views of the 30° nozzle drawn with solid lines and superimposed on the original nozzle drawn with dashed lines. The side view is a cutaway view in the plane containing the plume axis and a perpendicular line connecting the electrodes, while the top view is a cutaway view in the plane containing the plume axis and a perpendicular line connecting the side-fed Teflon propellant bars. To further reduce the backflow with the 30° nozzle, a flat plate shield was attached to the outer lip of the nozzle. This plate extends outward to the dimensions of the thruster aluminum enclosure, approximately 38 cm square. Figure 39 shows the 30° nozzle and shield installed on the thruster with supports on each corner. Figure 40 shows

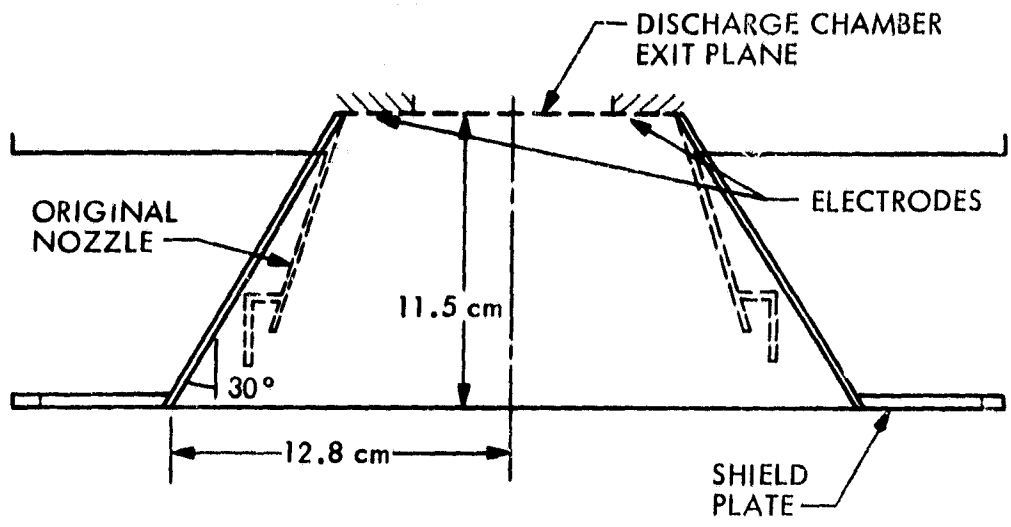

a) CUTAWAY SIDE VIEW

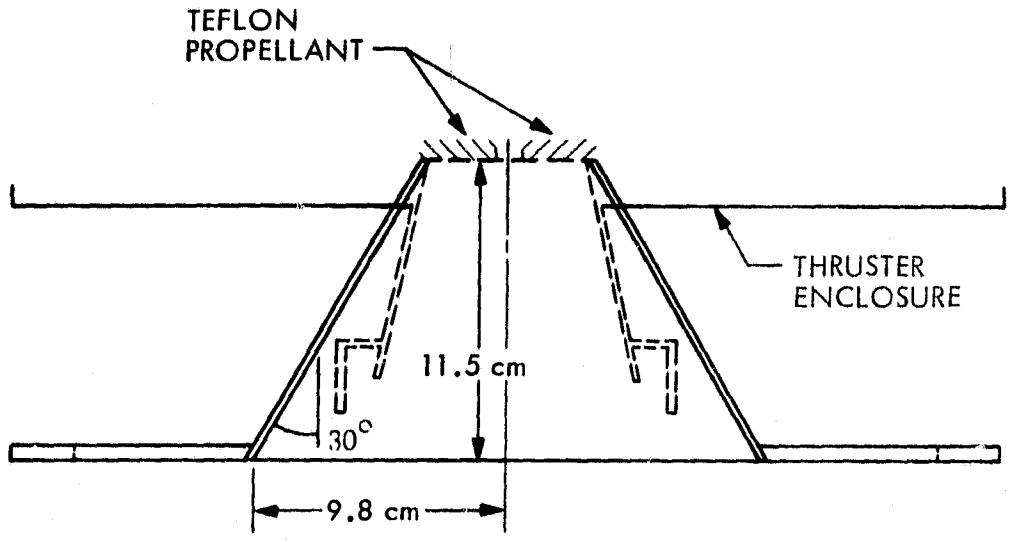

b) CUTAWAY TOP VIEW

Figure 38. PPT Nozzle Schematics

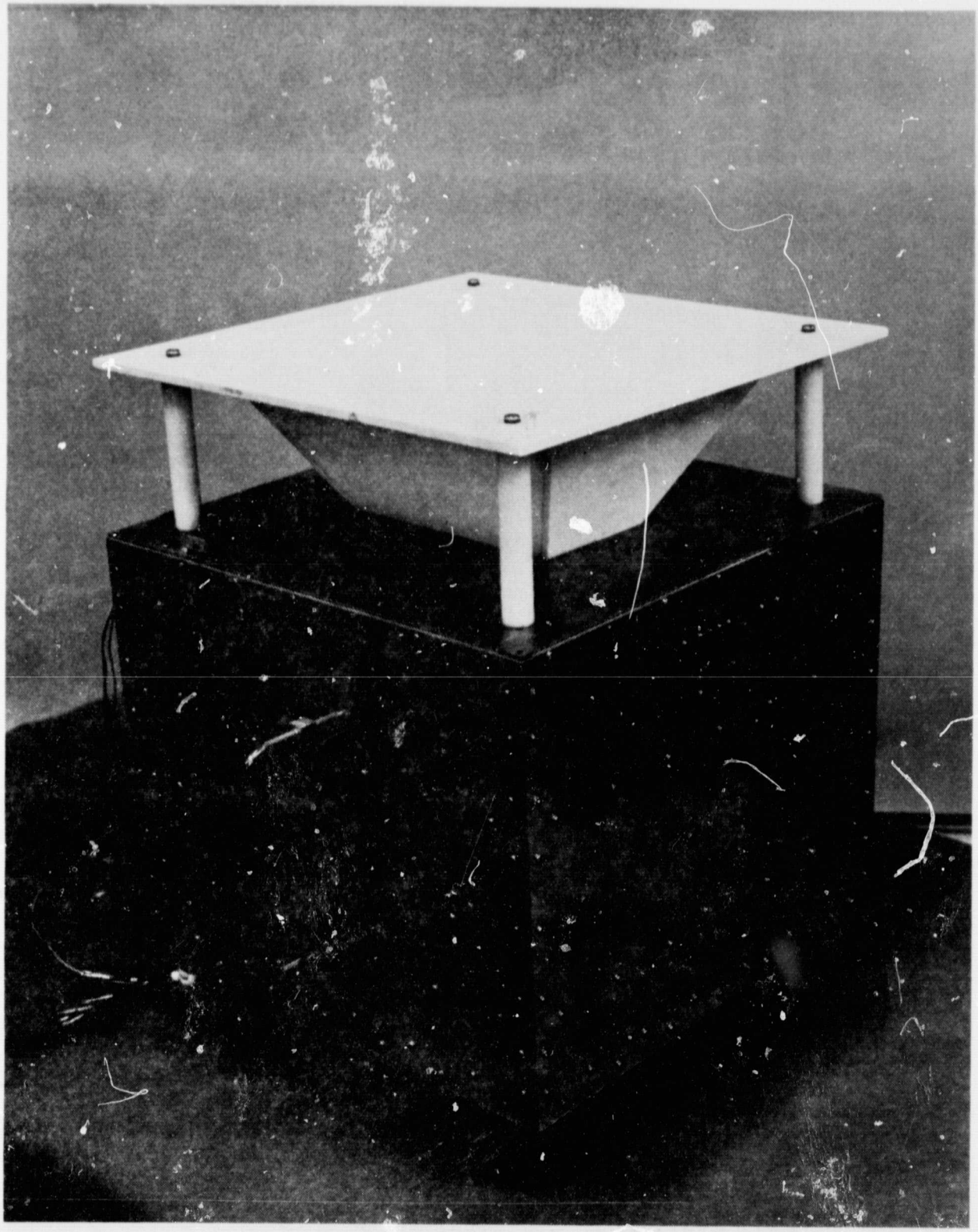

Figure 39. PPT 30° Nozzle - Oblique Side View

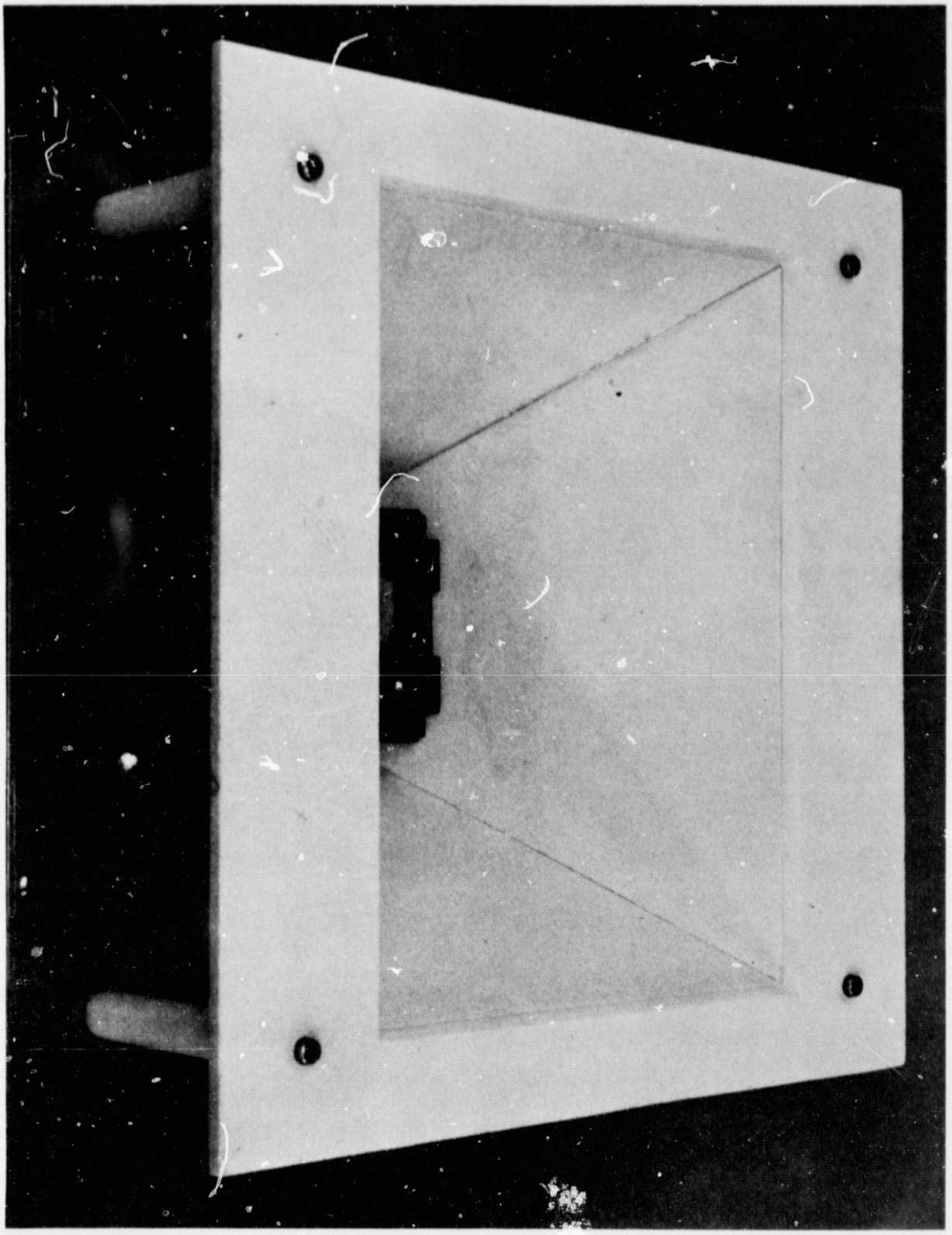

Figure 40. PPT 30° Nozzle - Oblique Front View

a view looking obliquely upstream into the nozzle throat.

The thruster with the 30° nozzle was positioned in the MOLSINK facility with the nozzle exit plane at the same location as was the original nozzle exit plane in the tests of Section 3.0. The collimated QCM array was positioned at the 2.54 cm downstream location and the 11.1 cm upstream position as in the original nozzle tests,and data was taken for simila. dip angles from 0 to 60°, Data was also taken from the QCMs mounted on the brackets on the MOLTRAP walls (see Figure 25). All experimental conditions were maintained as close to those of the original nozzle tests as possible, to provide as accurate a comparison between the two nozzles as possible. Data was taken over a two week period during which over 260 hours of facility operation were accumulated. Table VIII shows the results of the collimated QCM array measurements tabulated for the various array positions and dip angles. As in Table III, the correlation coefficients for the data are shown in parentheses and provide a measure of the error in each datum.

The results of the plume-wall backscatter measurement from the QCMs mounted on the MOLSINK wall are tabulated in Table IX. Following an analysis identical to that in Section 4.1 for the original nozzle backscatter, these backscatter mass fluxes were reduced to intensities and are shown plotted versus angular location on the MOLSINK wall in Figure 41. Also shown is the data from Figure 31 for the original nozzle. Although the two sets of data are within a factor of two of each other, and hence, are within the QCM error bar, the consistently higher data for the 30° nozzle suggests a greater mass flux

arrival rate at the walls at higher angular locations. This, in turn, suggests that with the 30° nozzle, the average plume expansion angle is larger than with the original nozzle, or alternatively that the 30° nozzle-shield combination is directing more of the plume material downstream, and thus, decreasing the plume backflow. Distinguishing between these possibilities would require further testing; however, some indications that the second alternative is correct will be seen in the following section.

TABLE VIII. 30° Nozzle Array Mass Fluxes (X 10^{-5} $\mu g\text{-}cm^{-2}\text{-}pulse^{-1}$)

Axial Position	Dip Angle	Radius							
		38 cm		54 cm		70 cm		86 cm	
		1	2	3	4	5	6	7	8
2.54cm downstream	0°	18.5 (.999)	23.7 (.997)	16.1 (.963)	9.2 (.946)	11.4 (.930)	-	7.0 (.979)	6.5 (.938)
	12°	19.8 (.999)	20.4 (.999)	11.2 (.946)	12.7 (.991)	7.2 (.986)	-	7.1 (.954)	-
	24°	19.6 (.999)	17.3 (.999)	7.0 (.947)	9.1 (.915)	6.3 (.993)	-	9.1 (.993)	10.6 (.986)
	36°	15.9 (.998)	12.5 (.997)	-	13.3 (.973)	5.8 (.969)	-	15.7 (.981)	17.8 (.958)
	60°	10.4 (.997)	8.7 (.997)	-	15.1 (.967)	9.3 (.985)	-	13.3 (.983)	12.3 (.968)
11.1cm upstream	12°	9.6 (.998)	6.5 (.995)	8.9 (.767)	9.9 (.972)	12.0 (.984)	8.6 (.848)	3.8 (.794)	-
	26°	14.6 (.998)	10.0 (.998)	-	9.6 (.925)	6.5 (.993)	6.0 (.825)	8.9 (.961)	10.4 (.948)
	36°	9.4 (.999)	6.7 (.996)	7.5 (.908)	8.7 (.861)	7.3 (.990)	5.9 (.949)	9.5 (.981)	9.9 (.962)
	60°	10.0 (.996)	6.5 (.994)	-	13.3 (.965)	8.9 (.989)	4.6 (.602)	13.9 (.950)	13.5 (.950)

TABLE IX. 30° Nozzle Backscatter Mass Fluxes

QCM Bracket Angle	Mass Flux ($\mu g\text{-}cm^{-2}\text{-}pulse^{-1}$)
45°	8.49×10^{-4}
45°	7.13×10^{-4}
60°	3.88×10^{-4}
75°	1.37×10^{-4}
75°	2.06×10^{-4}

5.2 30° Nozzle Backflow Analysis Using the best exponential fit of the measured plume-wall backscatter, as shown in Figure 41, corrections to the collimated QCM array data of Table VIII were calculated in a manner identical to that of Section 4.1. Using this corrected data to determine the maximum allowable dip angle, these data were integrated over the dip angle to determine the total backflow flux through the QCM array plane (see Section 4.2 and Figure 33) from the plume region between the dip angles of zero and the maximum value. To insure a consistent comparison between the original and the 30° nozzle, the maximum dip angle for the individual collimated QCMs for the 30° nozzle was taken to be identical to that used in the original nozzle analysis (see Table VIII). Table X shows the integrated backflow fluxes versus array axial location and QCM radius. For comparison the backflow fluxes measured with the original nozzle are also shown along with the values of the maximum dip angle in parentheses.

These tabulated values are plotted versus radius in Figures 42 and 43, for both nozzles and for the two array locations. The data taken for the 2.54 cm

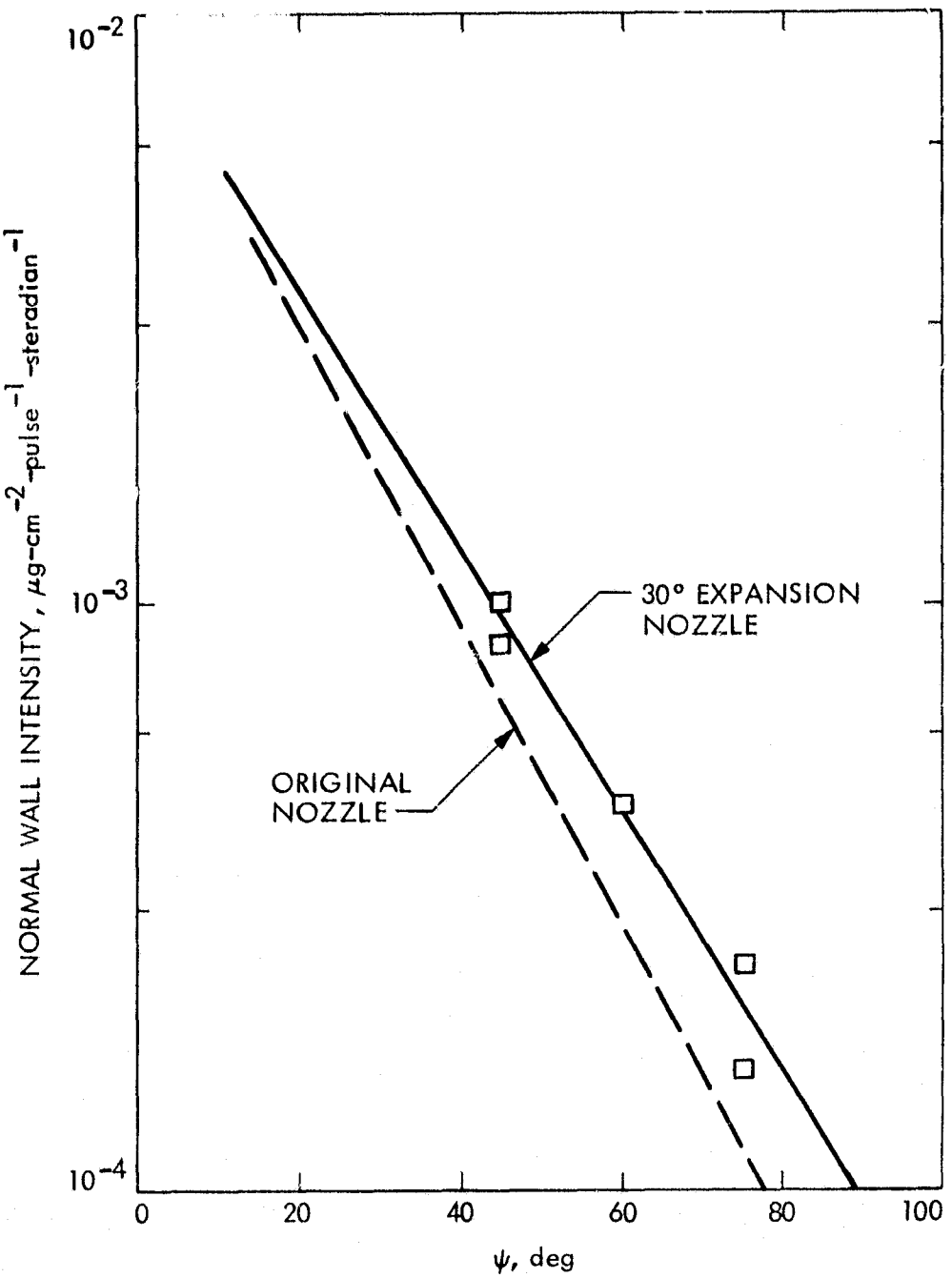

Figure 41. Wall Scattering Intensity - 30° Nozzle

TABLE X. Plume Backflow Results for Both Nozzles ($X\ 10^{-4}\ \mu g\text{-}cm^{-2}\text{-}pulse^{-1}$)

(α_{max})

Array Axial Position	Nozzle	QCM Radius			
		38 cm	54 cm	70 cm	86 cm
2.54cm downstream	30° Nozzle	4.9	1.67	0.72	0.58
	Original Nozzle	7.14 (44°)	1.15 (34°)	0.15 (22°)	0.37 (26°)
11.1cm upstream	30° Nozzle	3.1	2.2	1.4	0.7
	Original Nozzle	6.55 (54°)	4.4 (45°)	0.9 (30°)	1.3 (36°)

downstream array axial location is, within the QCM error, identical for both nozzles. Conversely, for the 11.1 cm upstream axial location, the 30° nozzle has a significantly lower backflow for the lower radius locations. These results indicate that with the original nozzle, a significant backflow arises between the downstream edge of the nozzle and the radius of the closest QCM (38 cm). With the 30° nozzle and shield, this portion of the backflow is considerably reduced, leading to the drop in the measured data at the 11.1 cm upstream position. The equivalent data at the 2.54 cm downstream location indicates that this deflected portion of the original nozzle backflow is directed downstream and not just radially outward to the edge of the shield and back upstream. Furthermore, the equivalent data at the 2.54 cm downstream location suggests that the 30° nozzle does not materially change the downstream plume flow profiles, and indicates that the shield may have the greatest effect on the backflow.

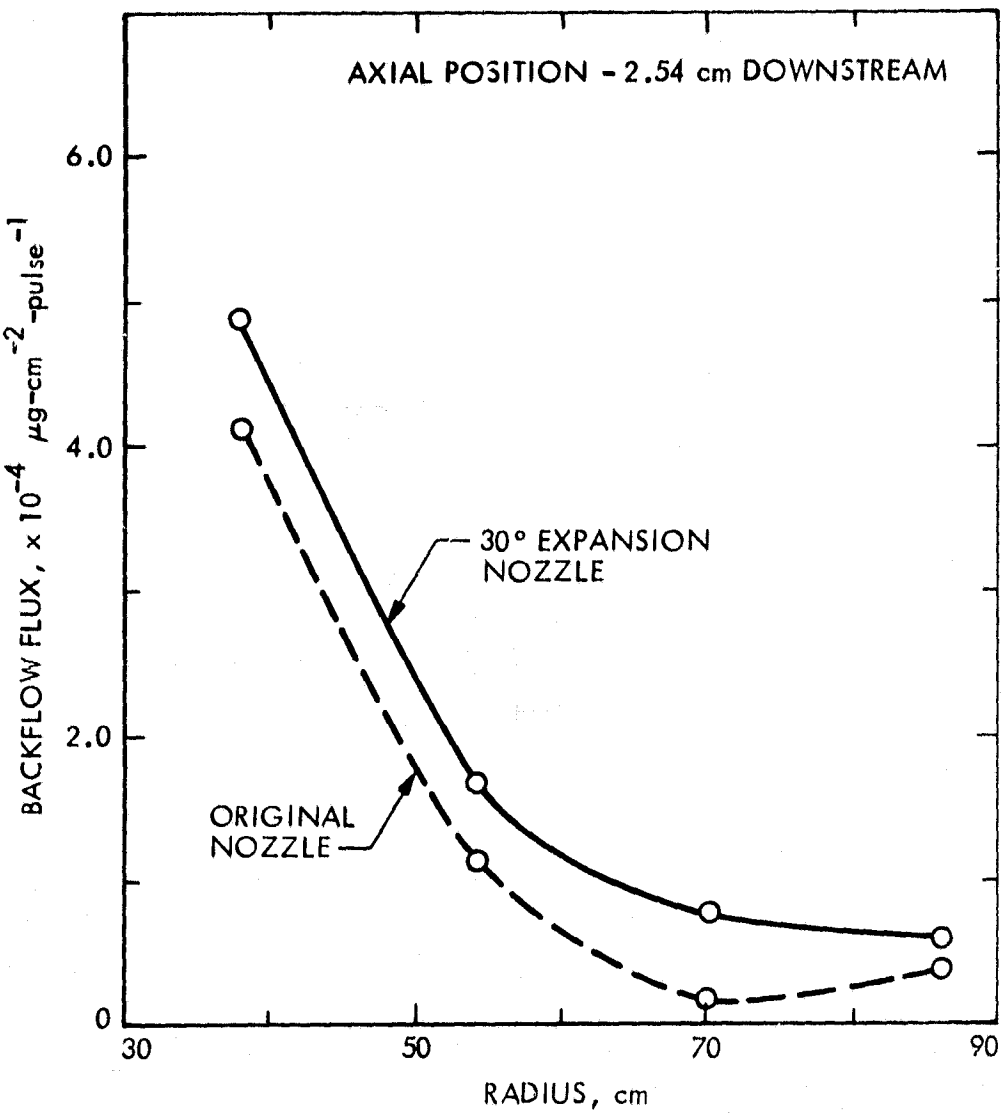

Figure 42. Backflow Radial Variation - 2.54 cm Downstream

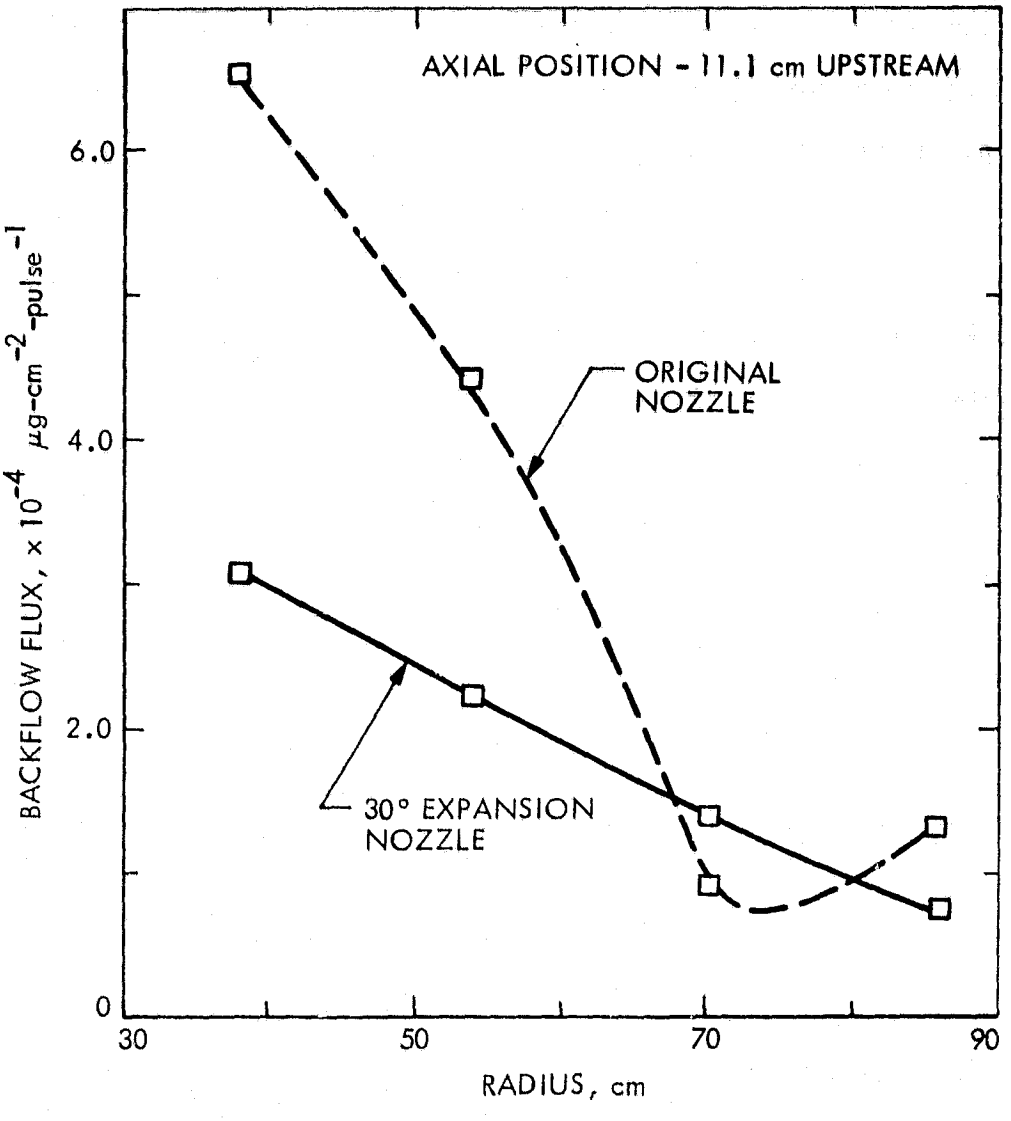

Figure 43. Backflow Radial Variation - 11.1 cm Upstream

5.3 Faraday Cup Assessment A Faraday cup collects and measures the charged particle flux to a collecting electrode from the plasma under study. This collecting electrode sits at the bottom of an insulating cup and is connected to a large reference electrode directly in touch with the plasma. A screen grid, placed over the opening of the cup, is normally biased negatively with respect to the reference electrode to repel the electron flux to the collecting electrode. The ion flux to the collecting electrode flows through the circuit and back to the plasma via the reference electrode. The ion flux or current is measured in the circuit and used to estimate the total mass flux via the ionization fraction. The time response of the Faraday cup is limited by the electronics used to measure the ion current, and hence can be made fast enough to allow resolution of the mass flux during just one PPT discharge pulse.

The purpose of this investigation was to assess the ability of the Faraday cup to provide accurate measurements of the PPT plume backflow, and to corroborate the previous QCM measurements. To this end, a Faraday cup with a collecting area of 1.27 cm^2 was mounted on the MOLSINK tank wall in the PPT nozzle exit plane on the opposite side of the thruster from the collimated QCM array. The collecting cup was turned to face directly towards the PPT axis, so as to observe a backflow mass flux similar to that measured with the collimated QCMs. Because it was attached to the MOLSINK wall, the Faraday cup operated at a temperature of about 15-20 K.

The ion current through the cup circuit was measured using one of two alternate methods. In the first method, a 1000Ω resistor was placed in series with the circuit, and the voltage across this resistor was monitored.

The second method used a Tectronics Model 6042 current probe which monitors the ion current through the magnetic field induced in the circuit wiring, and thus, interferes minimally with the actual probe circuit. The ion current was monitored and recorded on an oscilloscope triggered by the noise generated by the thruster discharge. Figure 44 shows two oscillographs of the ion current taken under identical conditions with the two alternate current measuring methods. The ion current measured with the resistor-voltage probe combination is the observed voltage divided by 1000Ω , which is consistent with the peak current of about 0.8 to 1.0 mA, taken using the Tectronix current probe. As can be seen, the Tectronix probe suffers from a relatively small signal to noise ratio.

In order to accurately measure the total ion flux to the Faraday cup, the grid bias must be set to repel the maximum number of electrons, and yet, minimally affect the incoming ion trajectories. To determine the appropriate value for the bias, measurements were made over a range of bias voltages from 0 to 100 volts. At 100 volts, the gap between the grid and the cup would break down occasionally, thus effectively limiting the maximum bias to this value. The measured ion currents were found to generally increase with increasing bias voltage, while the total ion flux to the Faraday cup integrated over time varied by no more than a factor of two over the total range of bias values. This behavior indicates that the higher bias voltages are more desirable; however, within the overall error bar, the value of bias voltage has only a small effect on the results.

(a)

RESISTOR-VOLTAGE PROBE

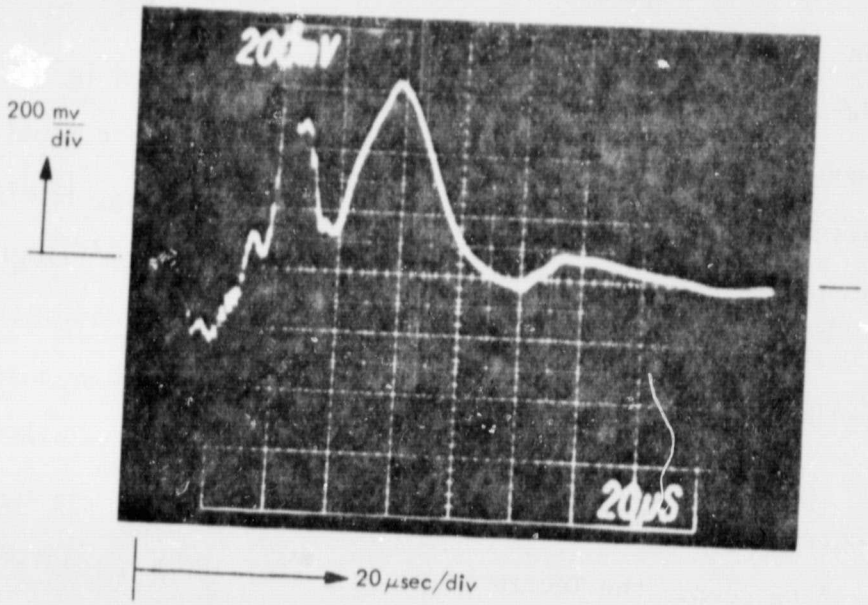

(b)

TECTRONIX CURRENT PROBE

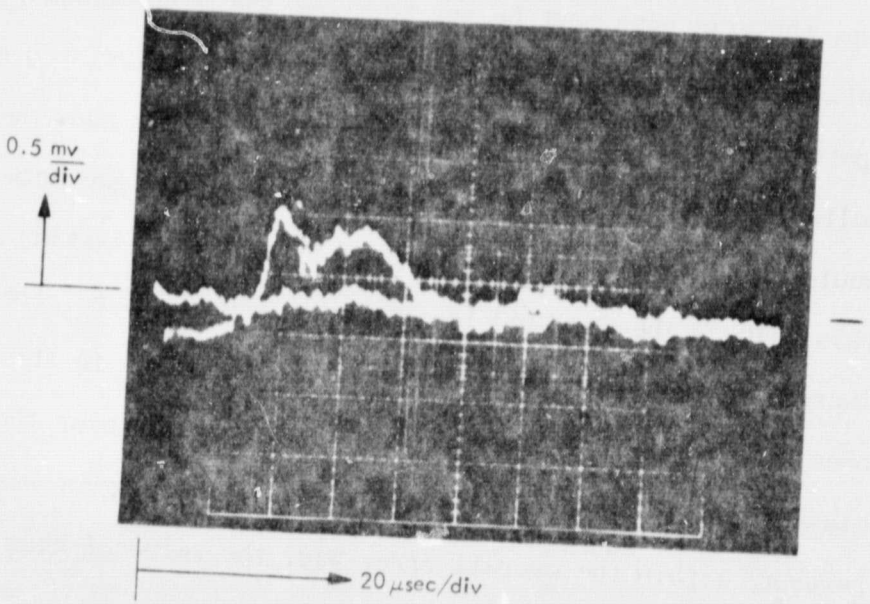

Figure 44. Faraday Cup Signals

Figure 44 shows that the ion current to the cup is negative during the first 30 μsec following the PPT discharge initiation. Since the cup is approximately 1 meter from the PPT thruster, this 30 μsec delay is consistent with the time required for ions moving at 30,000 m/sec to reach the collecting surface (see Section 2.0). Following this delay, the current shows a distinct double peak structure which cannot be due to plasma-wall backscatter since the time separation between the two peaks is too short. A possible explanation may lie in the observation by Palumbo and Begun[11] of plasmoids (blobs of luminous plasma) being accelerated off the thruster electrodes. The separation of these plasmoids was roughly correlated with each reversal of the PPT discharge current. For the thruster under study, the discharge current reverses once about 15 μsec from the beginning of the discharge[5], implying one plasmoid followed by a continuous plasma flow. The separation between the peaks of the Faraday cup data is about 20 to 30 μsec and may be due to the differing velocities of these two plasmoids driven by the decaying current.

The total ion flux collected by the Faraday cup during one PPT discharge pulse can be calculated by integrating the measured ion current over the total observation time. The average flux was obtained by estimating this integral for several PPT discharges and averaging the results. This flux was found to be 2×10^{11} ions-cm^{-2}-pulse^{-1}, assuming no double ions. Using the average atomic weight of Teflon of 16.7 amu for the ion mass, the total mass flux collected by the Faraday cup is 5.5×10^{-6} μg-cm^{-2}-pulse^{-1}. The measured QCM mass flux corrected for the larger aperture of the Faraday cup and the radius

of 1 meter from the PPT thruster axis is over 20 times larger than this value, indicating that either the Faraday cup is not collecting all the plasma ions or that the actual plasma ionization fraction is so small that the ion mass flux is only a fraction of the total. In either case it appears that the Faraday cup does not provide an accurate quantitative measure of the actual PPT backflow flux.

5.4 Summary The backflow measurements taken with the 30° nozzle on the PPT confirm the ability of the collimated QCM array to distinguish between changing mass flux levels and indicate that the overall backflow with the 30° nozzle-shield combination is less than that of the original nozzle. It is believed that the major factor in reducing the backflow is the shield and not the increased expansion angle of the 30° nozzle. The larger plume-wall backscatter found with this nozzle implies that the mass which previously was backflow is being redirected to the outer edges of the primary plume, however, it may also be due to a larger plume expansion angle.

Even with the large error on the QCM backflow flux measurements, the QCM still appears to be better than a Faraday cup for measuring this flux. The Faraday cup is useful in observing the time history of the PPT discharge plume; however, even here there remain some problems in interpreting the data. During these studies it was not possible to satisfactorily explain the apparent negative ion current during the first 30 μsec of the Faraday cup signal. In addition, the behavior of the ion current dependence on bias voltage is difficult to fully explain. Before the Faraday cup can be used with confidence, these points should be addressed.

6.0 SUMMARY AND CONCLUSION

The simplicity and reliability of micropound PPT thrusters stimulated the development of a larger millipound version suitable for an expanded range of applications including north-south stationkeeping. The larger impulse bit and greater total impulse of this millipound thruster have led to concerns about potential exhaust plume contamination of sensitive spacecraft surfaces, and thus, to a program at the Jet Propulsion Laboratory aimed at characterizing the flow field of the millipound thruster plume, especially in the region upstream of the thruster nozzle. Phase I of this program, detailed in an earlier report, was aimed at developing an understanding of the PPT plume-wall backscatter levels in the special MOLSINK vacuum facility, and a method of measuring the PPT plume backflow in the presence of this backscattered flux.

Phase II of the PPT plume characterization is detailed in this report. The primary purpose of this Phase II effort was to measure, using the method developed in Phase I, the PPT plume backflow flux over a range of locations radially away from and upstream of the thruster nozzle exit plane. As a corollary to this effort, a secondary task was to develop a better understanding of the thruster primary plume mass flux downstream of the nozzle exit plane. Once these original tasks were completed, a small additional study was made to determine the sensitivity of the PPT plume backflow to a different thruster nozzle design, and to the presence of a shield surrounding the nozzle.

In order to insure the successful completion of the MOLSINK facility PPT plume backflow measurement, the studies of the primary PPT plume were carried out first, so that the results could be factored into the design of the backflow

measurement system. Several tests were made using various diagnostics including a Mylar sheet deposition target, a double QCM probe, high speed photography, spectroscopy and carbon disk deposition analysis. These tests confirmed that despite the high aspect ratio rectangular PPT discharge chamber, the primary plume is essentially axisymmetric at distances of over 75 cm from the exhaust nozzle. The plume was consistently found to have an expansion half angle of between 30° and 40°, which, from the double QCM probe results, represents the plume radius at which the downstream mass flux has dropped to 10% of its centerline value. Furthermore, the plume mass flux profile was found to have a half-angle at half its centerline value of about 20°, indicating that the plume is more collimated than was previously supposed. Observations of the plume with high-speed photography indicate that it consists of a high velocity ($\sim$30 km/sec) luminous plasma combined with a much slower nonluminous gas. When these two mass flows are averaged, it is known that the average plume exhaust velocity is about 17 km/sec, hence the slow nonluminous component must be a significant fraction of the total plume. The flow of this component may be less dominated by the electromagnetic forces which tend to confine the plume to the thruster axis, and thus the plume back-flow may originate with the more ordinary gasdynamic expansion of this cooler plume component.

Spectroscopic evidence confirms that the luminous component of the plume contains ionized fluorine and carbon, and hence, is highly energetic. The observed erosion of surfaces placed in the primary plume is most probably due

to impingement by this high energy plasma. Analysis of the deposits on carbon sampling disks indicates that the Teflon propellant plume is primarily vapor with few large particles. This vapor condenses uniformly over the collecting surface, indicating that the QCM calibration constant analysis is correct in assuming no point masses on the sensing electrode. The observed erosion of the PPT electrodes is confirmed by the presence of copper on the sampling disk placed in the primary plume. This copper was not observed on the sampling disk upstream of and just outside the nozzle, indicating that the eroded copper is not in the plume backflow.

During the Phase I effort of this PPT thruster plume characterization, a concept of measuring the plume backflow in the MOLSINK facility was developed. This concept uses collimated QCMs to observe the plume backflow while avoiding any observations of the plume-wall backscatter. During the current Phase II, the design of these collimated QCMs was refined based on testing in the SEP facility, and an array of collimated QCMs was assembled and installed in the MOLSINK facility. Included in this installation was a series of QCMs mounted on the MOLSINK inner wall to observe the plume-wall backscatter. These observations were used to check the collimated QCM array measurements to insure that the backflow measurements were not compromised by contributions from this backscatter. The results of these measurements were analyzed extensively to account for various complicating design features of the experimental system and to determine the actual plume backflow levels at various radial and axial positions in the PPT nozzle vicinity. The results indicate that in a region between 30 and 86 cm from the thruster axis and from 11.1 cm upstream to 30.5 cm downstream of the nozzle exit plane, the plume backflow mass flux is of order

10^{-10} g-cm^{-2}-pulse^{-1}. Although the error bar on this flux is roughly a factor of two, an analysis of its radial dependence indicates an approximate inverse quadratic drop-off with distance from the thruster axis.

In order to place the magnitude of the measured PPT plume backflow in context with other types of thruster systems, a comparison can be made to the backflow flux from the plume of an 8 cm mercury ion thruster. This thruster has a nominal thrust level of one millipound as does the PPT; however, its specific impulse is approximately 60% higher and its mass flow rate is 40% lower than the PPT thruster. The 8 cm mercury ion thruster was developed for applications similar to those of the pulsed plasma thruster, including stationkeeping and attitude control. The total backflow from the plume of this ion thruster was estimated by summing the contributions from both the mercury propellant and molybdenum sputtered from the grids,[14] for locations identical to those where the PPT backflow measurements were made. The backflow flux from the PPT, as shown in Table VII, was corrected for the nominal pulse rate of 0.2 pps and was found to be identical, within experimental error, to that found for the ion thruster.

The investigation of the primary plume indicated that a significant fraction of the plume mass is relatively slow moving and at a low temperature. This suggests that the flow of this material is predominantly gasdynamic, and thus, dependent on the discharge nozzle design. Furthermore, since the higher energy plasma component of the plume is confined to the magnetic nozzle set up by the discharge, a large fraction of the measured backflow may arise from the gasdynamic flow around the nozzle lip of the lower energy fraction of the plume.

To test this possiblity, a new nozzle was designed for the PPT thruster with an expansion angle of 30^{o} and an exhaust plane area of roughly twice that of the original nozzle. Included in this design was a flat plate shield which extends outward, in the nozzle exit plane, to a size corresponding to the size of the thruster enclosure.

This new nozzle-shield combination was tested in the MOLSINK facility under conditions identical to those of the original nozzle backflow test. The results were analyzed and then compared to those of the original nozzle backflow levels. This comparison indicates that the nozzle itself makes little difference in the magnitude of the backflow, but the shield has a strong effect on reducing the backflow in regions upstream of the nozzle exit plane. This reduction is as much as a factor of three for close radii, while at larger radii, the backflow is not affected.

The major purpose of the plume characterization was to measure the backflow flux from the PPT plume in order to assist in determining the effect of its deposition on various spacecraft surfaces. The final assessment of the plume backflow must include considerations, not only of the total backflow flux, but of what fraction of this flux actually deposits and what actual effect does this deposit have on the various surfaces. These problems depend strongly on the type of surface (solar array, thermal radiator, spacecraft housing, observation ports, etc) and the surface temperature. For example, certain solar cell array designs use Teflon covers, and hence may be totally unaffected by the plume deposits[15]. At the other extreme sensitive optical

sensors with heavy plume deposits would have perturbed transmission or absorption characteristics, and thus, significantly degraded performance levels. Finally, continuing improvements in the thruster performance, including increasing specific impulse and thrust, imply a reduction of the backflow mass flux. With all of these factors in mind, the current measurements can only be used for rough estimates of what the ultimate effect of the PPT plume backflow will be.

7.0 REFERENCES

1. D. C. MacLellan, H. A. MacDonald, P. Waldon and H. Sherman, "Lincoln Experimental Satellites 5 and 6", AIAA Paper No. 70-494, AIAA Third Communications Satellite Systems Conference, Los Angeles, CA, April 6-8, 1970.

2. S. G. Rosen, "Colloid and Pulsed Plasma Thrusters for Spacecraft Propulsion", AIAA Paper No. 73-1254, AIAA/SAE 9th Propulsion Conference, Las Vegas NV, November 5-7, 1973.

3. W. J. Guman and D. J. Palumbo, "Pulsed Plasma Propulsion System for North-South Stationkeeping", AIAA Paper No. 76-999, AIAA International Electric Propulsion Conference, Key Biscayne FL, November 14-17, 1976.

4. W. C. Lyon, "Thruster Exhaust Effects Upon Spacecraft", AIAA Paper No. 70-1143, AIAA 8th Electric Propulsion Conference, Stanford CA, August 31 - September 2, 1970.

5. W. J. Guman and M. Begun, "Exhaust Plume Studies of a Pulsed Plasma Thruster", AIAA Paper No. 78-704, AIAA/DGLR 13th International Electric Propulsion Conference, San Diego CA, April 25-27, 1978.

6. L. C. Pless, L. K. Rudolph and D. J. Fitzgerald, "Plume Characteristics of a One-Millipound Solid Teflon Pulsed Plasma Thruster-Phase I Final Report", AFRPL-TR-78-63, Air Force Rocket Propulsion Laboratory, Edwards AFB CA, October 1978.

7. J. B. Stephens, "Space Molecular Sink Facility", 2nd Aerospace Mechanisms Symposium, May, 1967.

8. D. J. Palumbo and M. Begun, "Experimental and Theoretical Analysis of Pulsed Plasma Exhaust Plumes", AFOSR-TR-78-1242, Fairchild Industries, Inc., Farmingdale NY, July 1978.

9. S. Nakanishi, "Some Diagnostic Evaluations of a Beam-Shield 8-cm Mercury Ion Thruster", AIAA Paper No. 78-702, AIAA/DGLR 13th International Electric Propulsion Conference, San Diego CA, April 25-27, 1978.

10. R. J. Vondra, K. Thomassen and A. Solbes, "Analysis of a Solid Teflon Pulsed Plasma Thruster", AIAA Paper No. 70-179, 8th Aerospace Sciences Meeting, NY, January 19-21, 1970.

11. D. J. Palumbo and M. Begun, "Plasma Acceleration in Pulsed Ablative Arc Discharges", Interim Report for Period 15 March 1975 - 15 March 1976, AFOSR-TR-76-738, Fairchild Republic Co., Farmingdale NY.

12. L. K. Rudolph, R. G. Jahn, K. E. Clark and W. F. Von Jaskowsky, "Performance Characteristics of Quasi-steady MPD Discharges", AIAA Paper No. 76-1000, 12th International Electric Propulsion Conference, Key Biscayne FL, November 1976.

13. V. N. Benham, "Private Communication", Air Force Rocket Propulsion Laboratory, Edwards AFB CA.

14. "8 cm Mercury Ion Thruster Subsystem Users Manual", Space Propulsion and Power Division, NASA-Lewis Research Center, Cleveland OH.

15. L. G. Chidester, "Advanced Lightweight Solar Array Technology", AIAA Paper No. 78-533, AIAA Conference on Large Space Platforms: Future Needs and Capabilities, Los Angeles CA, September 27-29, 1978.

16. W. J. Guman and M. Begun, "Pulsed Plasma Plume Studies", Air Force Rocket Propulsion Laboratory TR-77-2, Final Report, Edwards AFB CA, March 1977.

17. W. C. Lyon, "A Study of the Effects of Teflon Thruster Exhaust Upon a Spacecraft", Goddard Space Flight Center Report No. HIT-443, April 1970.

18. R. W. Phillips, et al., "Spacecraft Contamination Under Simulated Orbital Environment", J. Spacecraft, Vol. 14, No. 8, p 501, August 1977.

APPENDIX 1

QCM ERROR ANALYSIS

As discussed in section 2.3, the primary PPT plume has a significant neutral component. From section 5.3, it is evident that the plume backflow has an even larger component (up to 95%), hence to study the PPT plume mass flow, a diagnostic system is needed which is sensitive to both charged and neutral particles. Quartz crystal microbalances (QCMs) were chosen for this study because of this requirement and because they provide in-situ measurements which do not require removal for analysis and subsequent danger of contamination. In addition, their relative compactness allows several to be used simultaneously without overcrowding the vacuum facility.

The accuracy of a particular QCM measurement depends on several factors which can be split into two broad areas. The first area includes factors which describe the relation between the mass flux at a certain location and the actual collected mass when a QCM is at this location. These factors include considerations of the particle optics to the sensing crystal (i.e., collimator design and leakage), spurious mass accumulation (due to the vacuum tank environmental pressure and the pulsed thruster operation), and the accommodation coefficient of the collecting surface. The second area includes factors which relate the accumulated mass to the measured output frequency shift. These factors include the QCM temperature sensitivity and electronic stability, the value of the calibration constant, and the calculation of the frequency shift versus time. These factors will be discussed individually in the following paragraphs and then used to calculate a total error estimate.

PARTICLE OPTICS The plume ion number density has been measured and estimated to be between 10^{9}-10^{11} cm^{-3} in the nozzle exit plane for distances of order 50 cm away from the thruster axis. Presuming that the total heavy particle number density is about 10 times the ion density gives 10^{10}-10^{12} cm^{-3}. Average heavy particle elastic collision cross sections are of order 10^{-13}-10^{-14} cm^{2}; hence, the particle mean free paths are around 10-10^{4} cm. For the collimator designs used in the plume study effort, the characteristic size is about 8 cm, which is less than the particle mean free path. Thus, it is consistent to use simple optics theory with its concepts of the illuminato, penumbra and umbra viewing regions for the collimator design and operation. Collisional effects which would smear the distinction between these viewing regions can be and are neglected in the data reduction of section 4.0.

The possibility of mass flux leaks around the collimator to the QCM crystal was guarded against by careful shielding of the QCMs with Kapton sheet around the back and sides of the QCM body. The shields combined with the long particle mean free paths effectively prevented any flux from impinging on the collecting surface except for that which entered via the collimator aperture.

SPURIOUS MASS ACCUMULATION The ultimate MOLSINK facility pressure is of order 10^{-12} torr, while the temperature is of order 25 K. Assuming the gas in the chamber has a molecular weight equal to the average molecular weight of Teflon (16.6 amu), and using the ideal gas law, the particle density can be estimated as approximately 10^{-17} $g\text{-}cm^{-3}$. From kinetic theory the average mass flux through a unit area in one direction in a volume of gas is the product of

the gas density and the sound speed divided by 4. Using 5/3 as the ratio of specific heats, the sound speed at 25 K is 1.44×10^{4} cm-sec^{-1}; thus the average mass flux is 3×10^{-14} g-cm^{-2}-sec^{-1}. This flux is far smaller than the measured QCM fluxes; hence the error introduced by this low pressure environmental flux is negligible.

During the actual test, with the thruster firing, the MOLSINK environmental pressure is not constant, but fluctuates up to values considerably larger than the ultimate low pressure of 10^{-12} torr. This fluctuation is due to the discharge pulse mass input into the tank, and thus, is of very short duration. This short duration, combined with the pulse rate of once every 20 seconds, prevents the available pressure measurement system from giving an accurate value of the pressure versus time, primarily because the gauge time constant is about 3 seconds, i.e., much longer than the discharge pulse time. Due to this lack of available experimental data, the effect of this pressure rise on the QCM measurement must be estimated analytically.

The PPT discharge mass is about 1.56 mg-pulse^{-1}. This mass leaves the thruster and travels to the MOLSINK wall, 1.5 m away, with an average sonic velocity of $\bar{c}$. During the time after this first wall interaction, the mass accumulated on the QCM surfaces represents an error on the desired signal. From the Phase I study, 94% of the discharge mass is absorbed by the wall while the remaining 6% is backscattered. The backscattered mass travels upstream to the opposite end of the MOLSINK, conservatively about 3 m away. The time required to do this is 3 meters divided by the sound speed: $3/\bar{c}$. Assuming that during this time, the mass density, ρ, is equal to the remaining 6% of the plume mass divided by the tank volume (6.28 m^{3}), then the net mass accumulated on the representative QCM surface is:

$$M_{1-2} = \frac{\rho \bar{c}}{4}\left(\frac{3}{\bar{c}}\right) = \frac{3\rho}{4}$$

This is the accumulated mass during the time between the first and second wall interactions. Assuming that all subsequent wall interactions reduce the net mass by 50%, then the total mass accumulated on the QCM after one discharge pulse is the sum of $M_{1-2} + M_{2-3} + M_{3-4} \ldots$, which is found to be 1.8×10^{-3} $\mu g\text{-}cm^{-2}$ - $pulse^{-1}$. This figure is independent of the mass velocity and temperature; however it depends critically on the assumption of uniform density over the tank volume between collisions. If this assumption is relaxed in favor of a more concentrated plume volume, then the total mass accumulated on the QCM would drop since the time of exposure of the QCM surface to this density drops. In addition, if more than 50% of the mass is absorbed during each wall interaction, the accumulated mass would drop. These assumptions could easily make an order of magnitude difference in the analysis.

The calculated environmental flux represents that flux which would be measured by an uncollimated QCM in the MOLSINK tank. Comparing this result with experimental data from collimated QCMs must be done after the collimated QCM data has been reduced to a total flux by having the collimator effect integrated out. This integration was done for the original PPT thruster and nozzle in section 4.2 and the overall results are shown in Table VII. As can be seen, the smallest integrated signal, which must be greater than the environmental flux since it includes the backflow flux as well, is about 10^{-5} $\mu g\text{-}cm^{-2}$ -$pulse^{-1}$ at a location of 2.5 cm downstream and 70 cm radius. Thus, the previous analytical result is roughly 180 times too large. As can be seen in Table VII, the majority of the data points are significantly

larger than 10^5 $\mu g\text{-}cm^{-2}\text{-}pulse^{-1}$ thus the error due to the environmental flux is usually small. At its largest this error is no more than a factor of two on the smallest backflow flux value.

QCM ACCOMMODATION COEFFICIENT The boiling points of the basic monomers of depolymerized Teflon are discussed in Reference 16. The lowest boiling point mentioned is for Hexafluoropropene (C_3F_6), which is 144 K. Furthermore, Reference 17 indicates that most chemical recombinations in the PPT plume occur within a few inches of the nozzle hence, the plume constituents are primarily these basic monomers. Since the QCMs of the current study were maintained at approximately 75 K, the accommodation coeffieient for these materials should be very close to 1.0; hence all the incoming mass to the QCM surface would be condensed on it. In any event, even if the accommodation coefficient is less than one, the QCM temperature is considerably lower than ordinary spacecraft surface temperatures. This indicates that any spacecraft surface would have a lower accommodation coefficient than the QCMs used here, and thus would collect less material than that collected on the QCMs of this study. In this respect, the measured QCM mass fluxes are conservative values of what would actually be affecting a spacecraft.

QCM TEMPERATURE AND ELECTRONIC STABILITY During the Phase I segment of the plume characterization study, a QCM design was developed which provided maximum electronic stability and minimum temperature variations in the output frequency. The use of a doublet temperature compensated design and AT cut quartz crystals provides a QCM which is virtually insensitive to temperature fluctuations in the range from -220 to -180 °C.

The thruster was floated with respect to the entire QCM system and the electronics support package for each QCM was modified to use bipolar transistors in order to eliminate the QCM sensitivity to thruster EMI. As discussed in section 3.3, the QCM stability was experimentally checked prior to the plume backflow measurement. The results demonstrated that the maximum drift in output frequency can be up to 2.9 Hz. To minimize the error induced by this drift, where practical, each experimental datum was determined by at least a 20 Hz shift, thus the maximum error is less than 10% for most of the data.

FREQUENCY SHIFT CALCULATION Each QCM output frequency was monitored versus time for test times of order 20-40 hours. The time was measured with a clock accurate to several minutes, and the frequency shift was measured with a counter accurate to 1 Hz. Measurements were made on the average of once per hour; thus a minimum of 20 data points were accumulated per QCM flux measurement. A linear regression analysis was used to calculate the slope of the frequency shift versus time, which is directly proportional to the accumulated mass flux. The error in the slope calculation is equal to $\pm\sqrt{1-\sigma^2}$, where σ is the linear regression correlation coefficient. These coefficients are tabulated with the backflow measurements in Tables IV and VIII. As can be seen, the usual correlation coefficient is about 0.95; thus the slope error is about $\pm$ 10%.

QCM CALIBRATION CONSTANT During the QCM development of the Phase I segment of this effort, the calibration constant was derived analytically and

measured experimentally. The calibration constant for an identical QCM was measured very accurately by Phillips[18] using sputtered aluminum as the deposit material. The calibration constant depends on the quartz crystal oscillation frequency, the cut angle, the quartz density and the uniformity of the deposit on the sensing surface. These quantities are all fixed once the particular QCM design is chosen except for the deposit uniformity. This uniformity was examined and is discussed in section 2.4, where it is shown that the PPT plume deposit is very smooth with relatively few point masses. Based upon this examination, it was concluded that the QCMs in use for this plume study effort are identical to that calibrated by Phillips. The final value of the calibration constant used in the Phase II effort is the one found by Phillips, which is 1.77×10^{-8} $\mu g\text{-}cm^{-2}\text{-}Hz^{-1}$ ± 5%.

SUMMARY The total error of the QCM flux measurement is just the root mean square sum of the errors discussed in the previous paragraphs. This error is on average about ± 20%; however, for a few selected data it can be as high as a factor of 2.5, due to the potential environmental flux. Once this data is used in the analysis of section 4.0, an additional uncertainty of about a factor of 2 is introduced due to the analytical assumptions and limitations. The final values of plume backflow mass flux have an uncertainty about a factor of 2, up to 5 for the worst case.

APPENDIX 2

COORDINATE TRANSFORMATIONS

A coordinate system $\vec{R}=(x,y,z)$ is attached to the thruster (see Figure 2-1). The axial distance down the plume from the nozzle exit plane is z; x and y are transverse coordinates with the QCM array holder located in the negative y-direction (x=0). The array holder slants down and away from the thruster exit at an angle of 12.7°. Four pairs of QCMs, labeled A, B, C, D are located on the holder at negative y-values of 38 cm, 54 cm, 70 cm and 86 cm, respectively. Since the y increment between pairs is 16cm, the corresponding z increment is 16 tan 12.7°=3.606 cm. Each pair has a QCM positioned at x=$\pm$ 7.9375 cm. A translation of $\vec{R}$ to coordinates $\vec{R}'_S = (x'_S, y'_S, z'_S)$ with origin at pair centers (see pair B in Figure 2-1) is accomplished as $\vec{R}'_S = \vec{R} - \vec{R}_t$, where $x_t = 0$; $y_t = -38,-54,-70,-86$; and $z_t = z_A, z_A + 3.606, z_A + 7.212, z_A + 10.818$ for pairs A, B, C, D, respectively. Pair A QCMs are labeled 1 and 2; pair B, 3 and 4, pair C, 5 and 6; pair D, 7 and 8. Odd number QCMs have a positive x position, even negative.

A second transformation of coordinates from $\vec{R}'_S$ to $\vec{R}_S = (x_S, y_S, z_S)$ consists of an x-translation $\Delta x = 7.9375$ to a particular QCM center plus a rotation about the x-axis of an angle α (right hand rotation, see QCM 2 in Figure 2-1):

$$x_S = x'_S \mp \Delta x$$

$$y_S = y'_S \cos\alpha + y'_S \sin\alpha$$

$$z_S = -y'_S \sin\alpha + z'_S \cos\alpha$$

The y_S axis is now the QCM collimator look direction for a dip angle α. The normal to the QCM crystal has a fixed dip angle of 22.5°; hence the collector angle relative to Z_S is $\iota = \alpha - 22.5°$. For $-8° \leq \alpha \leq 57°$, then

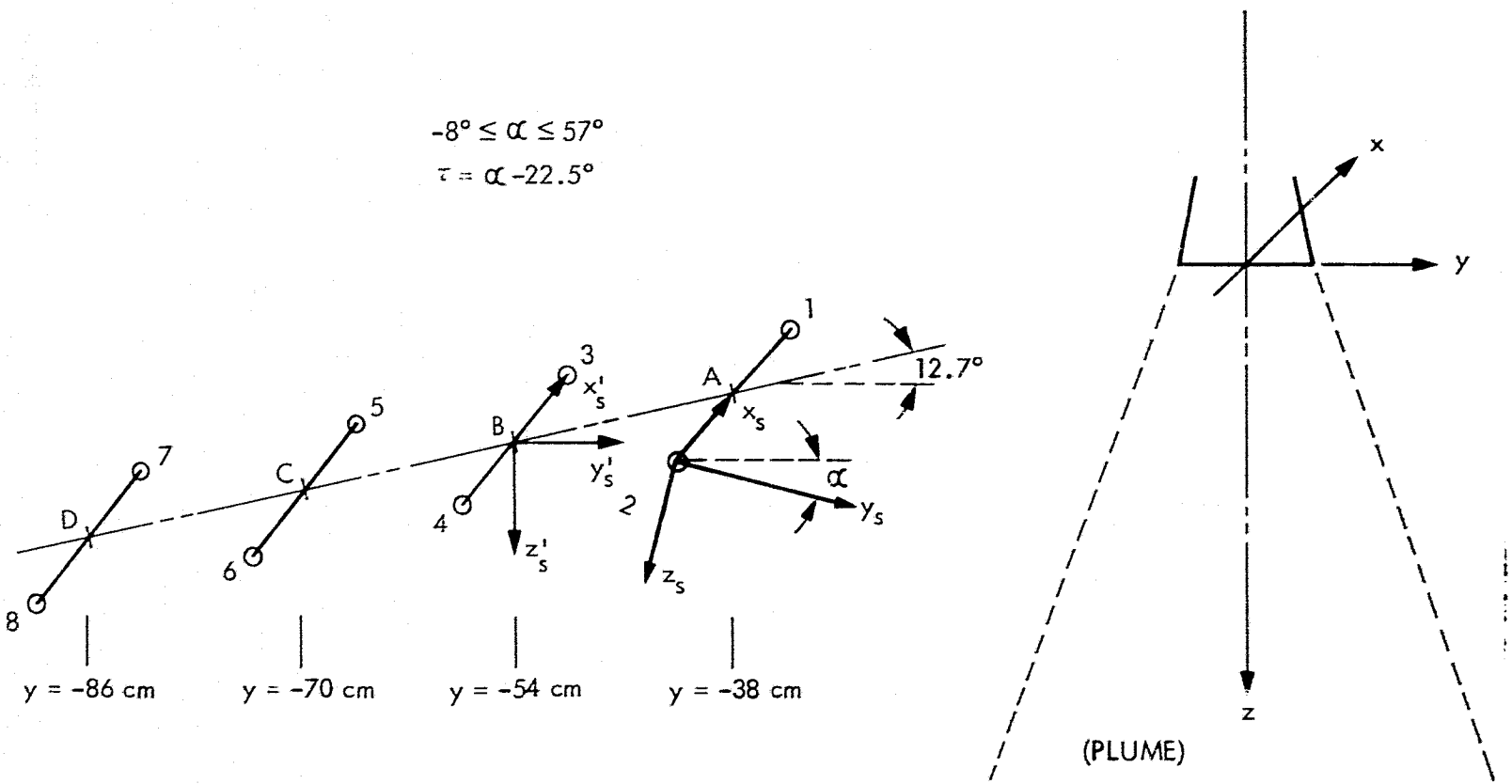

Figure 2-1. Coordinates Relative to QCMs and Plume

$-30.5^{o} \leq \tau \leq 34.5^{o}$.

If the plume is to be assumed axially symmetric, then more convenient coordinates are $\vec{R} = (r,\theta,z)$ where $x = r\cos\theta$, $y = r\sin\theta$. The transformation $(r,\theta,z) \rightarrow (x_s, y_s, z_s)$ is a three step process.

APPENDIX 3

SOLID ANGLE CALCULATION FOR WALL QCM

The solid angle of the QCMs used to measure backscatter from the wall is calculated neglecting wall curvature. The QCMs see the wall through a hole of radius R_o; their surface is a distance d from the wall and h from the cover plate front (see Figure 3-1). The equation of the sight cone of collector surface element dA_c located at $r = R, \theta = z = 0$ is

$$[r\cos\theta - R(1-z/h)]^2 + r^2\sin^2\theta = R_o^2\left(\frac{z}{h}\right)^2$$

The surface area seen by element dA_c is bound by the circle

$$[r\cos\theta - R(1-d/h)]^2 + r^2\sin^2\theta = (R_o\, d/h)^2 \equiv R_i^2$$

which is centered at $x = r\cos\theta = -R\left(\frac{d}{h} - 1\right)$. Coordinates relative to the circle center are denoted by a prime. Consider a wall element dA located at (r,θ), the angle γ between a line from dA_c to dA and the wall normal is given by

$$\cos\gamma = \frac{d}{\sqrt{(r'\cos\theta' - Rd/h)^2 + (r'\sin\theta')^2 + d^2}}$$

It is assumed that the wall backscatter intensity has the form $I = I_o\cos\gamma$. Also, the solid angle of dA_c as seen by the wall element is

$$d\Omega = \frac{\cos\gamma\, dA_c}{(r'\cos\theta' - Rd/h)^2 + (r'\sin\theta')^2 + d^2}$$

The total flux to the QCM surface is

$$F = \int I\, d\Omega\, dA = I_o d^2 \int dA_c \int_0^{2\pi}\int_0^{R_i} \frac{r'dr'd\theta'}{[(r'\cos\theta' - R\, d/h)^2 + (r'\sin\theta')^2 + d^2]^2}$$

where $dA_c = 2\pi RdR$, $0 \le R \le R_o$. Let $u \equiv \left(\frac{R}{R_o}\right)^2$, $v \equiv \left(\frac{r'}{R_i}\right)^2$, then integrating over θ' gives:

$$F = (\pi R_o)^2\, I_o\, S(a)$$

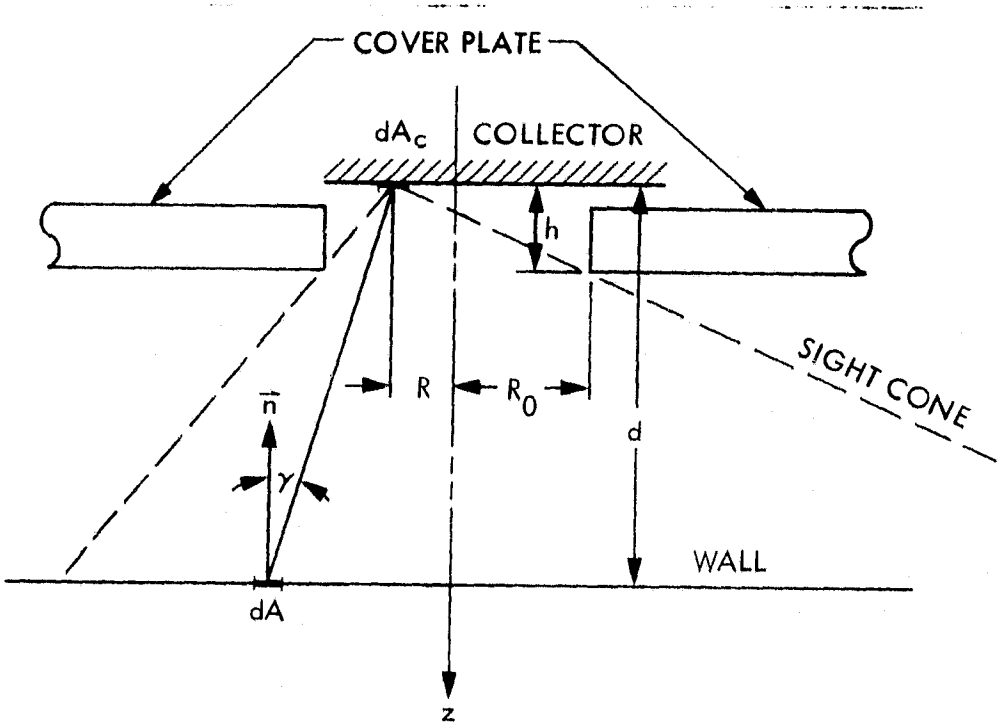

Figure 3-1. Wall QCM Geometry

for $a \equiv (h/R_o)^2$, with $S(a) \equiv a \int_0^1 \int_0^1 \frac{(u+v+a)\, dv\, du}{[(u+v+a)^2 - 4uv]^{3/2}}$

For the present geometry, a=1.96 and numerical evaluation gives S=0.2710823. Using R_o= 0.396875 cm, I_o ($\mu g\text{-pulse}^{-1}\text{-cm}^{-2}\text{-ster}^{-1}$) is given by a datum F($\mu$g/pulse) as $I_0 = 2.373F$.

APPENDIX 4

SLANTED COLLECTOR SOLID ANGLE CALCULATION

The QCM signal results from particles scattered in a plume slice defined by the collimator. For each volume element in a slice, the QCM collector opening presents a solid angle Ω to the scattering source; reduction of the QCM data to find the source distribution thus requires an expression for the source weighting factor $\Omega/4\pi$. An analysis of the collimator geometry follows, see Figure 4-1. In the figure, the source or scattering point is $\vec{R}_s = (x_s, y_s, z_s)$ in coordinates attached to the collimator. The collector is at an angle τ relative to the z-axis (Figure 4-2) and is defined by $|x| \leq h/2$, $|\zeta| \leq w/2$. The aperture slit of the collimator is defined by $r=r_c$, $|\theta| \leq \theta_a$, $|z| \leq a/2$ for $x=r\sin\theta$, $y=r\cos\theta$. The collector unit normal vector $\vec{n} = (0,\cos\tau,-\sin\tau)$ and a collector area element $dx\,d\zeta = dA$ is located at $\vec{R}_c=(x,\zeta\sin\tau\ ,\ \zeta\cos\tau)$. The corresponding solid angle differential is

$$d\Omega = \frac{\vec{n} \cdot \vec{R}}{R^3}\ dA$$

where $\vec{R} = \vec{R}_s - \vec{R}_c$. This is to be integrated over the intersection or overlap of the opening and the projection or mapping of the aperture slit from the source point to the plane of the collector. (The penumbra corresponds to a partial overlap, the umbra to a null overlap, and the illuminato to full overlap.) The mapping is given by

$$x = \frac{1}{D}\left[r_c\cos\tau\ (y_s\sin\theta - x_s\cos\theta) + \sin\tau\ (x_s\ z - r_c\ z_s\sin\theta)\right]$$

$$\zeta = \frac{1}{D}\ (y_s\ z - r_c\ z_s\ \cos\theta)$$

where $D = \cos\tau\ (y_s - r_c\cos\theta) - \sin\tau\ (z_s - z)$.

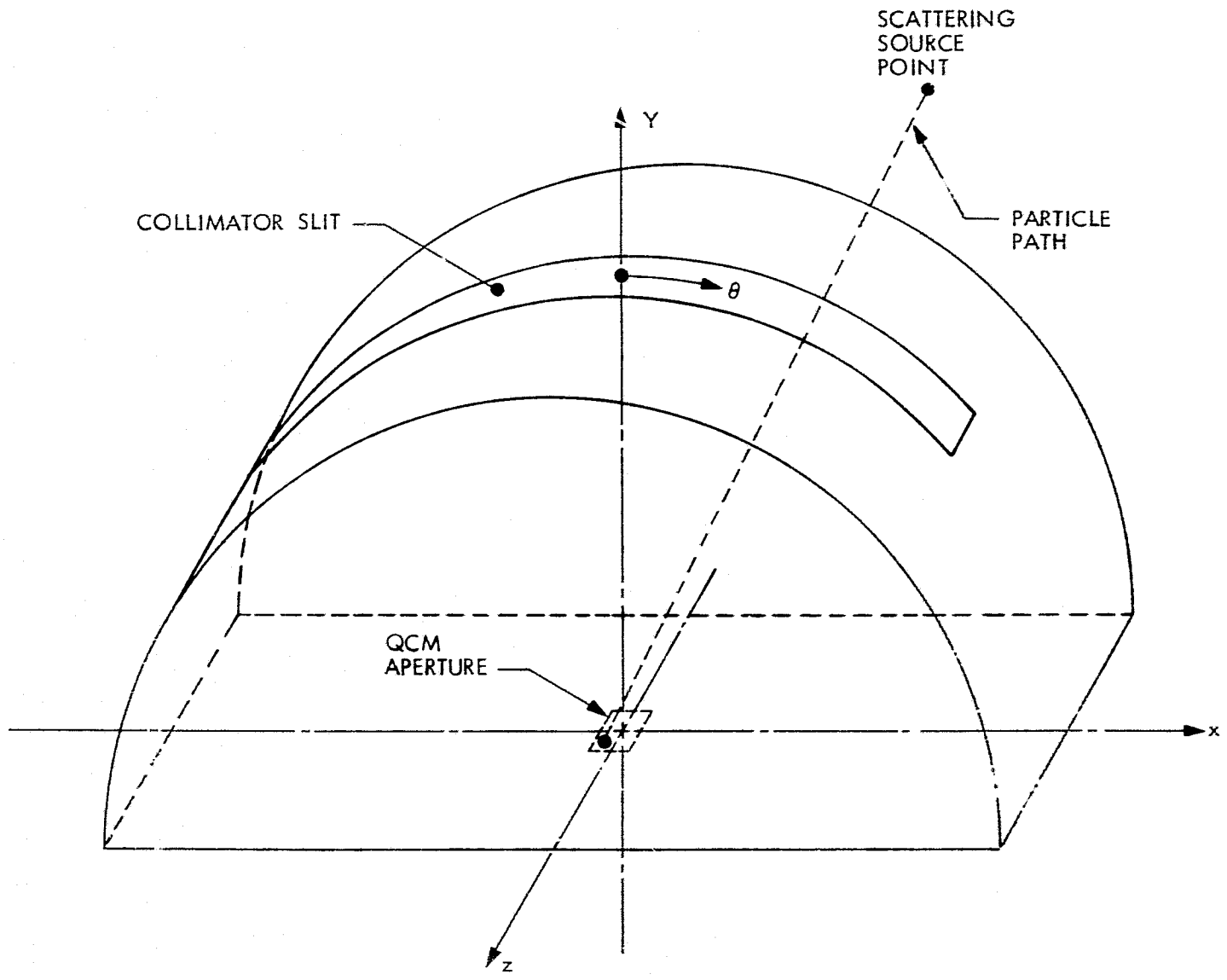

Figure 4-1. Collimator Perspective

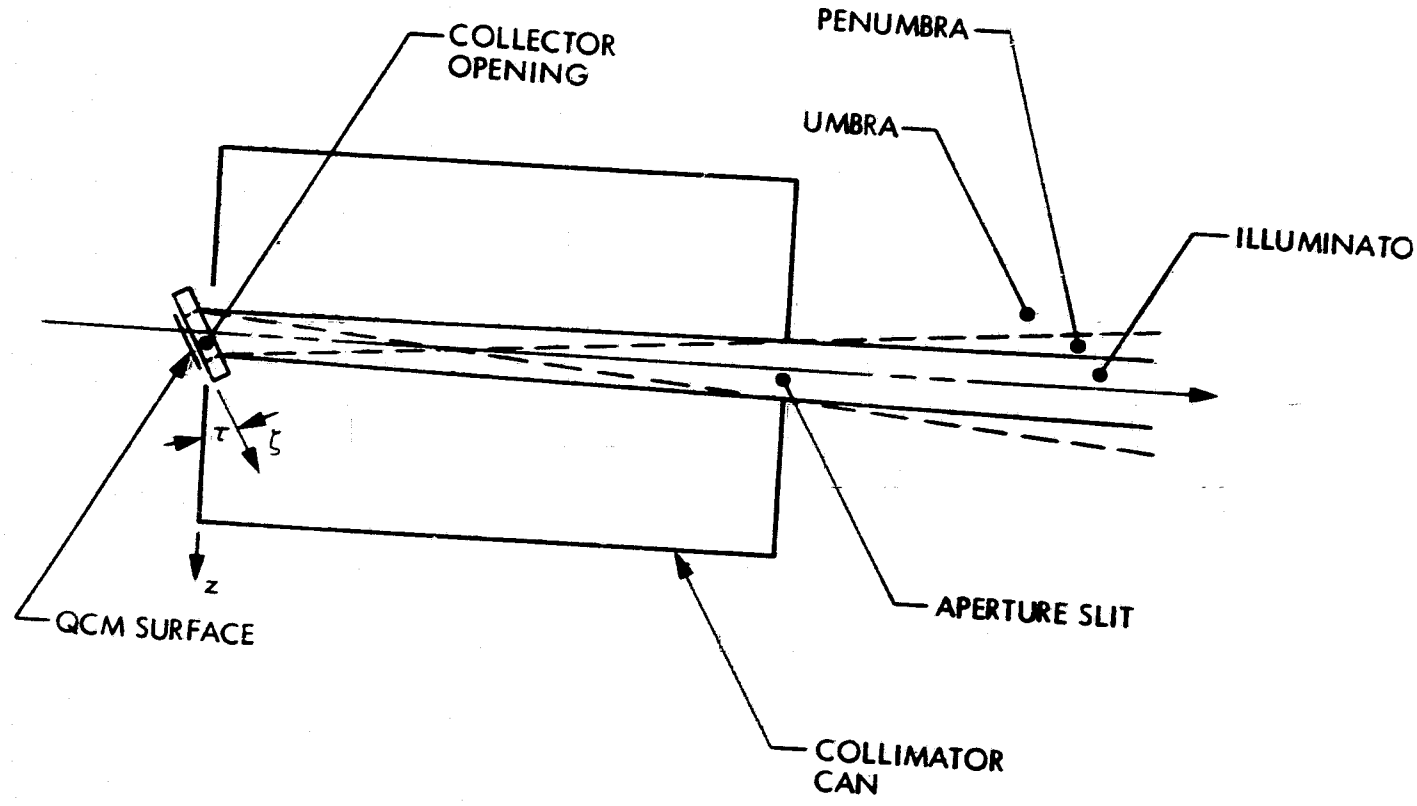

Figure 4-2. Collimator Section

The Jacobian is

$$\frac{\partial(x,\zeta)}{\partial(\theta,z)} = \frac{r_c}{D^3}\,(y_s\cos\tau - z_s\sin\tau)^2(x_s\sin\theta + y_s\cos\theta - r_c)$$

The mapping is nonsingular as long as $D>0$: only the region $y_s>r_c$ is (and need be) considered. Since $R_c << R_s$, the solid angle is approximately

$$\frac{d\omega}{dA} \approx \frac{(y_s\cos\tau - z_s\sin\tau)}{R_s^3}\left\{1 + \frac{3}{R_s^2}\left[x_s x + (y_s\sin\tau + z_s\cos\tau)\,\zeta\right]\right\}$$

with an error less than $\dfrac{h^2 + w^2}{3\,R_s^2}$, i.e., less than 1% for $R_s=r_c$. With $R_s >> r_c$ for most volume elements, this expression gives negligible error.

Let $\beta \equiv r_c/y_s < 1$ and $x_s \equiv \rho\sin\phi$, $y_s \equiv \rho\cos\phi$. The inverse mapping through order $\left(\frac{x}{r_c}\right)^2$, $\left(\frac{\zeta}{r_c}\right)^2$ is $\theta = \phi + (1-\beta\cos\phi)(1+\beta\cos\phi\,\xi)\eta$

$$Z = \beta\cos\phi\, z_s + \beta(1-\beta\cos\phi)\left[(1+\beta\cos\phi\,\xi)\left(\frac{\zeta}{r_c}y_s\cos\tau - \xi z_s\cos\phi\right) - \tfrac{1}{2}(1-\beta\cos\phi)\,\eta^2 z_s\cos\phi\right]$$

where $\xi \equiv \dfrac{x}{r_s}\sin\phi + \dfrac{\zeta}{r_c}\sin\tau\cos\phi$, $\eta \equiv \dfrac{x}{r_c}\cos\phi - \dfrac{\zeta}{r_c}\sin\tau\sin\phi$.

The penumbra region with respect to θ at $\theta\equiv\theta_a$ is for

$$\phi = \theta_a - (1-\beta\cos\theta_a)\left[\frac{x}{r_c}\cos\theta_a - \frac{\zeta}{r_c}\sin\tau\,\sin\theta + A\left(\frac{x}{r_c}\right)^2 + B\,\frac{x}{r_c}\,\frac{\zeta}{r_c}\sin\tau - C\left(\frac{\zeta}{r_c}\sin\tau\right)^2\right]$$

where

$$A = (1-\beta\cos\theta_a)\sin\theta_a\cos\theta_a$$

$$B = \cos^2\theta_a - \sin^2\theta_a + 2\beta\sin^2\theta_a\cos\theta_a$$

$$C = \sin\theta_a(\cos\theta_a + \beta\sin^2\theta_a)$$

Since Θ_a is relatively large and the region small, any variation in the presumed small source function is neglected and half the region is included in the illuminato, the other half in the umbra:

$$d\Omega = 0 \quad \text{if} \quad |\phi| > \phi^*$$

$$|x| \leq h/2 \quad \text{if} \quad |\phi| \leq \phi^*$$

where $\phi^* = \Theta_a + (1-\beta\cos\Theta_a)\left[\left(\frac{\zeta}{r_c}\sin\tau\right)\sin\Theta_a - A\left(\frac{h}{2r_c}\right)^2 + C\left(\frac{\zeta}{r_c}\sin\tau\right)^2\right]$

The problem of calculating Ω is now reduced to that of the penumbra region with respect to z (or ζ). Define $\zeta^{\pm} \equiv \zeta(z \equiv \pm \frac{a}{2})$ and $\zeta_1 \equiv \max(\zeta^-, -w/2)$, $\zeta_2 \equiv \min(\zeta^+, \frac{w}{2})$. Then $\Omega = 0$ if $\zeta_1 \geq \zeta_2$ and the combined penumbra-illuminato is for $\zeta_1 \leq \zeta \leq \zeta_2$:

$$\Omega = \frac{(y_s\cos\tau - z_s\sin\tau)}{R_s^3}\int_{-h/2}^{h/2} dx\ (\zeta_2-\zeta_1)\left[1 + \frac{3x_s}{R_s^2}x + \frac{3}{2R_s^2}(y_s\sin\tau + z_s\cos\tau)(\zeta_2+\zeta_1)\right]$$

The integration is to be done numerically. Angle ϕ^* is to be calculated with ζ replaced by $\frac{1}{2}(\zeta_1+\zeta_2)$. The equation for ζ can be put into an approximate quadratic form:

$$K_2\,\zeta^2 - K_1\,\zeta + K_o = 0$$

giving $\zeta \doteq \frac{K_o}{K_1}\left(1 + \frac{K_o K_2}{K_1^2}\right)$. Here $K_o = (z - \beta\cos\phi\ z_s p)y_s$

where

$$p(x)\ 1-(1-\beta\cos\phi)\frac{x}{r_c}\left|\sin\phi+\tfrac{1}{2}\cos\phi\ [\cos\phi+\beta\ (2-3\cos^2\phi)]\ \frac{x}{r_c}\right| ,$$

$$K_1 = y_s\cos\tau(1-\beta\cos\phi)+\sin\tau\ [z-z_s\cos\phi(\cos\phi+\beta\sin^2\phi)] + (1-\beta\cos\phi)\sin\phi\cos\phi$$

$$[r_c\cos\tau+(\cos\phi+\beta(1-3\cos^2\phi))\ z_s\sin\tau]\ \frac{x}{r_c}$$

$$K_2 = (1-\beta\cos\phi)\ \sin^2\phi\sin\tau\ [\cos\tau+(1-3\beta\cos\phi)\ \cos\phi\ \frac{z_s}{2r_c}\ \sin\tau]$$

Each source point has as its weighting factor the collector solid angle $\Omega/4\pi$ times the appropriate volume element size.

A similar formulation holds for a surface source function. In particular, the solid angle factor may be used when weighting wall backscatter if attenuation is neglected. Also needed in this particular situation is the additional factor of the cosine of the angle between the QCM solid angle direction and the wall normal. (The wall boundary is considered to be a smooth surface defined by the inner extremities of the anechoic chamber.) The wall is elliptic with its center located at $z_c = 4.445$ cm downstream of the PPT exit plane and with semimajor axis $a = 150$ cm and semiminor axis $b = 100$ cm. The wall is given as $r_w = b\left[1-\left(\frac{z-z_c}{a}\right)^2\right]^{\frac{1}{2}}$. The wall normal vector is proportional to $(r_w\cos\theta, r_w\sin\theta, -r_w \frac{dr_w}{dz})$ in plume based coordinates, where $-r_w \frac{dr_w}{dz} = \left(\frac{b}{a}\right)^2 (z-z_c)$. Also, the wall area element $dA_w = r_w \frac{dl}{dz}\, dz d\theta$, where l is the axial wall arc length, $r_w \frac{dl}{dz} = b\left[1-(1-(\frac{b}{a})^2)(\frac{z-z_c}{a})^2\right]^{\frac{1}{2}}$.

The solid angle direction is simply $(r_w\cos\theta, r_w\sin\theta, z)$ translated to QCM based coordinates (without rotation through dip angle, see Appendix 2). The cosine is calculated by taking the inner product of the normalized direction vectors. Total wall backscatter into a QCM can be easily found by summing $I_w \Omega \Delta A_w$ for small, discrete increments $\Delta z, \Delta\theta$.

Fortran Subroutine Listings

The subroutines used in the upper bound wall scattering correction estimates and source function analysis follow. Subroutine names, usages, and argument list definitions are:

NAME	USAGE	ARGUMENTS
(1) REFLC	Used to calculate corrections due to wall scattering	ALPHA - dip angle: ZA-axial position of QCM pair A: IQCM-QCM number: DT, DZ-intervals $\Delta\Theta$, ΔZ for integral sum
(2) WSF	Gives normal wall intensity	R,Z - coordinates r_w,^{z}
(3) MATRIX	Calculates influence matrix of volume source function	AM-array name: M,N-row and column size
(4) WFUN	Does coordinate transformations and calls solid angle subroutine	X,Y,Z or R, THETA, Z- source coordinates; WDR- $-r_w \frac{dr_w}{dz}$; ALPHA, ZA, IQCM-gives QCM position, see above; N-number of intervals for Simpson's integration for Ω; LGL-logical variable, if FALSE, then WFUN multiplies Ω by cosine factor
(5) OMEGA	Calculates Ω	XS, YS, ZS - source coordinates relative to collimator: TAU- collector slant angle; H,W- collector hole size; ATHETA, A- aperture opening angle and width; RC- collimator can radius; N- integration intervals
(6) COEFF	Calculates coefficients used to find $\zeta_{1,2}$	Q0, Q1, Q2, R0, R1, R2 coefficients; X- collector surface coordinates; Z- aperture edge position; YS-source coordinate

(7) LIMITS	Calculates $\zeta_2 \pm \zeta_1$	X-collector coordinate: ZL- aperture edge position; YS, ZS - source coordinates; W2- collector half-width; ERR- maximum quadratic term in calculations of $\zeta^{\pm}$; ZP, ZN- $(\zeta_2-\zeta_1)$, $(\zeta_2+\zeta_1)$
(8) RM	Calculates plume boundary radius (TPA=Tan of expansion angle)	THETA, Z- plume coordinates

```
      FUNCTION REFLC(ALPHA,ZA,IQCM,DT,DZ)
      DATA TINT,ZINT/360.0,154.445/R/100.0/
      X=0.0
      Y=0.0
      Z=R
      WDR=0
      A=WFUN(X,Y,Z,ALPHA,ZA,IQCM,6,.FALSE.)
      SUM=0.0
      IT=TINT/DT+0.5
      IF(IT.LT.1) IT=1
      A=FLOAT(IT)
      TS=TINT/A
      IZ=ZINT/DZ+0.5
      IF(IZ.LT.1) IZ=1
      A=FLOAT(IZ)
      ZS=ZINT/A
      Z=0.5*ZS
      DO 20 KZ=1,IZ
      WDR=0.44444*Z-1.97556
      R=1.0-1.25E-4*WDR*WDR
      IF(R.LE.0.0) GO TO 20
      SF=R*SQRT(R)
      R=1.R*R-0.8
      IF(R.LT.0.0) GO TO 20
      R=R*SQRT(R)
      SF=SF*WSF(R,Z)
      THETA=0.5*TS
      DO 10 KT=1,IT
      A=WF1(R,THETA,Z,WDR)
      IF(A.LE.0.0) GO TO 10
      SUM=SUM+A*SF
   10 THETA=THETA+TS
   20 Z=Z+ZS
      REFLC=1.7453293E-2*TS*ZS*SUM
      RETURN
      END
```

```
      FUNCTION WSF(R,Z)
      PHI=ATAN2(R,Z-4.445)
      WSF=4.82E-2*EXP(-3.37*PHI)
      RETURN
      END
```

```
      SUBROUTINE MATRIX(AM,M,N)
      PARAMETER NDP=40,NSP=3(
      REAL AM(NDP,NSP),ZV(NDP),ALPHV(NDP),R1(NSP),R2(NSP),
     C     T1(NSP),T2(NSP),Z1(NSP),Z2(NSP)
      INTEGER M,N,IQV(NDP),IR,IT,IZ
    1 FORMAT(2I3,1P3E12.5)
    2 FORMAT(1P2E12.5,I3)
    3 FORMAT(1P6E12.5)
    4 FORMAT(1H1,4X21HR,THETA,Z INCREMENTS=1P3E12.5)
    5 FORMAT(1H0,5X3SHDP       ZA          ALPHA        IQCM/
     C      (5XI3,1X1P2E12.5,5X12))
    6 FORMAT(1H0,5X2HSP,5X4HRMIN,8X4HRMAX,6X8HTHETAMIN,4X8HTHETAMAX,
     C      6X4HZMIN,8X4HZMAX/(5XI3,1X1P6E12.5))
      READ(5,1) M,N,DR,DT,DZ
      READ(5,2) (ZV(I),ALPHV(I),IQV(I),I=1,M)
      READ(5,3) (R1(I),R2(I),T1(I),T2(I),Z1(I),Z2(I),I=1,N)
      WRITE(6,4) DR,DT,DZ
      WRITE(6,5) (I,ZV(I),ALPHV(I),IQV(I),I=1,M)
      WRITE(6,6) (I,R1(I),R2(I),T1(I),T2(I),Z1(I),Z2(I),I=1,N)
      DO 100 I=1,M
      X=0.0
      Y=0.0
      Z=5(.
      A    =     WFUN(X,Y,Z,ALPHV(I),ZV(I),IQV(I),6,.TRUE.)
      DO 100 J=1,N
      SUM=0.0
      A=T2(J)-T1(J)
      IT=A/DT+0.5
      IF(IT.LT.1) IT=1
      B=FLOAT(IT)
      TS=A/B
      THETA=T1(J)+0.5*TS
      A=Z2(J)-Z1(J)
      IZ=A/DZ+(.5
      IF(IZ.LT.1) IZ=1
      B=FLOAT(IZ)
      ZS=A/B
      DO 50 KT=1,IT
      Z=Z1(J)+0.5*ZS
      DO 4  KZ=1,IZ
      A=RM(THETA,Z)
      A=AMIN1(A,R2(J))
      A=A-R1(J)
      IF(A.LE.0.0) GO TO 32
      IR=A/DR+0.5
      IF(IR.LT.1) IR=1
      B=FLOAT(IR)
      RS=A/B
```

```
      R=R1(J)+0.5*RS
      DO 32 KR=1,IR
      A=WF1(R,THETA,Z,55,0)
      A=A*R*RS
      SUM=SUM+A
      R=R+RS
   32 CONTINUE
      Z=Z+ZS
      THETA=THETA+TS
      A=1.7453293E-2*TS*ZS
      AM(I,J)=A*SUM
  100 CONTINUE
      RETURN
      END
```

/

```
      FUNCTION WFUN(X,Y,Z,ALPHA,ZA,IQCM,N,LGL)
      REAL X,Y,Z,ALPHA,ZA,SC
      INTEGER IQCM,N,J
      LOGICAL LGL
      DIMENSION SC(7),V(3)
      COMMON/SAC/SC
      DATA DA,DX,DZ,RC,A,H,W,RTD/22.5,7.9375,3.606,7.9375,0.79375,
     C     0.635,0.635,1.7453293E-2/
      X=X
      Y=Y
      Z=Z
      C=ALPHA-DA
      RL=OMEGA(RTD,DA,RTD,C,H,W,55.0,A,RC,N)
      J=IQCM+1
      J=J/2
      J=J-1
      FL=FLOAT(J)
      YT=38.0+16.0*RL
      ZT=ZA+DZ*RL
      ZT=-ZT
      J=IQCM/2
      J=IQCM-J-J
      C=RTD*ALPHA
      S=SIN(C)
      C=COS(C)
      GO TO 10
      ENTRY WF1(R,THETA,Z,WDR)
      WDR=WDR
      RL=RTD*THETA
      X= R*COS(RL)
      Y= R*SIN(RL)
```

```
      ENTRY WF2(X,Y,Z)
   10 XS=X
      YS=Y+YT
      ZS=Z+ZT
      RL=DX
      IF(J.EQ.1) RL=-DX
      XS=XS+RL
      AF=1.0
      IF(LGL) GO TO 20
      V(1)=XS
      V(2)=YS
      V(3)=ZS
      CALL SL2NRM(3,V,RL)
      V(1)=X
      V(2)=Y
      V(3)=WDR
      CALL SL2NRM(3,V,AF)
      AF=(X*XS+Y*YS+WDR*ZS)/(RL*AF)
   20 CONTINUE
      RL=YS
      YS=YS*C+ZS*S
      ZS=ZS*C-RL*S
      RL=OMEGA2(XS,YS,ZS)
      WFUN=7.9577472E-2*RL*AF
      RETURN
      END
```

```
      FUNCTION OMEGA(XS,YS,ZS,TAU,H,W,ATHETA,A,RC,N)
      REAL XS,YS,ZS,TAU,H,W,ATHETA,A,RC,S,X,A2,W2,ERR,ZD,ZA
      INTEGER N,J
      COMMON/SAC/RCP,SINTAU,COSTAU,BETA,SINPHI,COSPHI,CF
    1 FORMAT(4X5HBETA=1PE10.3,2X3HRS=1P3E10.3)
    2 FORMAT(4X4HERR=1PE10.3,2X3HRS=1P3E10.3)
    3 FORMAT(4X6HOMEGA=1PE10.3,2X3HRS=1P3E10.3)
      TAUR = 1.7453293E-2*TAU
      THETAR=1.7453293E-2*ATHETA
      SINTAU=SIN(TAUR)
      COSTAU=COS(TAUR)
      SINTHT=SIN(THETAR)
      COSTHT=COS(THETAR)
      A2=0.5*A
      H2=0.5*H
      W2=0.5*W
```

```
17*             RCP=RC
18*             N=N-N/2
19*             N=N+N
20*             S=FLOAT(N)
21*             ENTRY OMEGA2(XS,YS,ZS)
22*             OMEGA=0.0
23*             RS =XS*XS+YS*YS+ZS*ZS
24*             RS3=RS*SQRT(RS)
25*             PHI=ATAN2(XS,YS)
26*             SINPHI=SIN(PHI)
27*             COSPHI=COS(PHI)
28*             IF(YS.NE.0.0) BETA=RC/YS
29*             IF(0.0.LE.YS.AND.YS.LE.RC.AND.ABS(XS).LE.RC.AND.ABS(ZS).LE.A)
30*            C    WRITE(6,1) BETA,XS,YS,ZS
31*             IF(ABS(PHI).GE.1.0) RETURN
32*             IF(YS.LE.RC.OR.ABS(ZS*BETA*COSPHI).GT.(A2+W2)) RETURN
33*             CFA=1.0-BETA*COSTHT
34*             A=CFA*SINTHT*COSTHT
35*             C=SINTHT*(COSTHT+BETA*SINTHT*SINTHT)
36*             CF=1.0-BETA*COSPHI
37*             F1=YS*COSTAU-ZS*SINTAU
38*             F2=YS*SINTAU+ZS*COSTAU
39*         C SIMPSON'S RULE INTEGRATION
40*             X=-H2
41*             ERR=0.0
42*             CALL LIMITS(X,A2,YS,ZS,W2,ERR,ZD,ZA)
43*             E1=ZA
44*             E2=ZD
45*             E3=X*ZD
46*             E4=ZA*ZD
47*             DO 10 I=1,N
48*             J=I/2
49*             J=I-J-J
50*             X=X+H/S
51*             CALL LIMITS(X,A2,YS,ZS,W2,ERR,ZD,ZA)
52*             WF=2.0
53*             IF(J.EQ.1) WF=4.0
54*             IF(I.EQ.N) WF=1.0
55*             E1=E1+WF*ZA
56*             E2=E2+WF*ZD
57*             E3=E3+WF*X*ZD
58*             E4=E4+WF*ZA*ZD
59*          1  CONTINUE
60*             WF=3.0*S
61*             F1=E1/WF
62*             F2=E2/WF
63*             F3=E3/WF
64*             F4=E4/WF
```

```
      IF(ERR.GT.1.E-1) WRITE(6,2) ERR,XS,YS,ZS
    C
      X=H2/RC
      WF=0.5*F1*SINTAU/RC
      WF=THETAR+CFA*(SINTHT*WF+C*WF*WF-B*X*X)
      IF(ABS(PHI).GT.WF) RETURN
      WF=3.*PI/RS
      X=E2+WF*XS+E3+0.5*WF*F2+E4
      WF=F1*H*X/RS3
      IF(WF.LT.0.0) WRITE(6,3) WF,XS,YS,ZS
      OMEGA=AMAX1(WF,0.0)
      RETURN
      END
```

```
      SUBROUTINE COEFF(Q0,Q1,Q2,RC,R1,R2,X,Z,YS)
      REAL Q0,Q1,Q2,RC,R1,R2,X,Z,YS
      COMMON/SAC/RC,STAU,CTAU,BETA,SPHI,CPHI,CF
      Q0=YS*Z
      Q1=CF*CTAU*YS*(1.0+BETA*SPHI*CPHI*X/RC)+Z*STAU
      Q2=CF*STAU*CTAU*SPHI*SPHI
      R1 = RC-CF*X*(SPHI+0.5*CPHI*(CPHI+BETA*(2.0-3.0*CPHI*CPHI))*X/RC)
      R1= CPHI*R1
      R1=CPHI+BETA*SPHI*SPHI-CF*SPHI*(CPHI+BETA-3.0*BETA*CPHI*CPHI)*X/RC
      R1=CPHI*STAU*R1
      R2=CF*(0.5-1.5*BETA*CPHI)*SPHI*SPHI*CPHI*STAU*STAU/RC
      RETURN
      END
```



```
      FUNCTION RM(THETA,Z)
      REAL THETA,Z
      DATA RE,TPA/7.6,6.26794919/
      A =RE+TPA*Z
      B=6.666667E-3*Z-2.963333E-2
      B=1.0-B*B
      B=100.*SQRT(B)
      RM=AMIN1(A,B)
      RETURN
      END
```

```
1*          SUBROUTINE LIMITS(X,ZL,YS,ZS,W2,ERR,ZP,ZN)
2*          REAL X,ZL,YS,ZS,W2,ERR,ZP,ZN,S,Q0,Q1,Q2,R0,R1,R2
3*          DIMENSION S(7)
4*          COMMON/SAC/S
5*          CALL COEFF(Q0,Q1,Q2,R0,R1,R2,X,ZL,YS)
6*          Q0=Q0-R0*ZS
7*          Q1=Q1-R1*ZS
8*          Q2=Q2+R2*ZS
9*          ZP=Q0*Q2/(Q1*Q1)
1.*         IF(ABS(ZP).GT.ERR) ERR=ABS(ZP)
11*         ZP=Q0*(1.0+ZP)/Q1
12*         CALL COEFF(Q0,Q1,Q2,R0,R1,R2,X,-ZL,YS)
13*         Q0=Q0-R0*ZS
14*         Q1=Q1-R1*ZS
15*         Q2=Q2+R2*ZS
16*         ZN=Q0*Q2/(Q1*Q1)
17*         IF(ABS(ZN).GT.ERR) ERR=ABS(ZN)
18*         ZN=Q0*(1.0+ZN)/Q1
19*         Q2=ZP+ZN
2.*         W=W2+W2
21*         IF(ABS(Q2).GT.W) Q2=SIGN(W,Q2)
22*         ZP=AMIN1(ZP,W2)
23*         ZN=AMAX1(ZN,-W2)
24*         ZP=ZP-ZN
25*         ZP=AMAX1(ZP,0.0)
26*         IF(ZP.GT.0.0) Q2=ZN+ZN
27*         ZN=ZP+Q2
28*         RETURN
29*         END
```

APPENDIX 5

EFFECTIVE QCM SLIT ANGLE

It is desired to reduce the QCM data (in μg/pulse) of plume backscatter to a local intensity value. To do this, the effective collecting area-solid angle product needs to be calculated. For a given element of area on the QCM surface, the solid angle is defined by the aperture slit area. Coordinates relative to the collector have the x-axis as the tilt axis and y-axis as the look direction (see Figure 4-2, Appendix 4). The aperture slit is $r=r_c$, $|\theta| \leq \theta_a = 50^\circ$, $|z| \leq a/2$ for $x = r\sin\theta$, $y = r\cos\theta$. Since the QCM surface normal is at an angle τ to the look direction, (see Figure 4-1, Appendix 4), on the collection surface $y_c=\zeta\sin\tau$, $z_c=\zeta\cos\tau$ and the area element $dA_c = dxd\zeta$. The effective collection area is $\cos\theta\cos\tau\, dA_c$. For given x, ζ, let $\vec{R} = \vec{R}_{aperture} - \vec{R}_{collector}$ then $d\omega = R^{-3}(\vec{R}\cdot\vec{n})\, r_c\, d\theta dz$ where $R^2 = r_c^2+x^2+\zeta^2+z^2 - 2z\zeta\cos\tau - 2r_c(x\sin\theta+\zeta\sin\tau\cos\theta)$ and $(\vec{R}\cdot\vec{n})^2 = R^2-v^2$, $v^2 = (x\cos\theta-\zeta\sin\tau\sin\theta)^2+(z-\zeta\cos\tau)^2$. Integrating over z from -a/2 to a/2:

$$\int\cos\theta d\omega = r_c\int_{-\theta_a}^{\theta_a}\cos\theta\, d\theta\left\{\frac{1}{u}\tan^{-1}\left[\frac{ua}{u^2+\zeta^2\cos^2\tau-a^2/4}\right] - \int_{-a/2}^{a/2}\frac{wdz}{R^2}\right\}$$

where $u^2 = r_c^2+x^2+\zeta^2\sin^2\tau - 2r_c(x\sin\theta+\zeta\sin\tau\cos\theta)$ and $w = 1-(1-v^2/R^2)^{1/2}$. The argument of the inverse tangent is small; the function is replaced by the first two terms of its Taylor series. Within an error of order $(\frac{a}{r_c})^4 = 10^{-4}$:

$$\frac{w}{R^2} = \frac{v^2}{2r_c^4} \quad \text{and}$$

$$\int\cos\theta d\omega = ar_c\int_{-\theta_a}^{\theta_a}\cos\theta d\theta\left[\frac{1}{u^2+\zeta^2\cos^2\tau-a^2/4} - \frac{1}{2r_c^4}\left(v^2\big|_{z=0^+}\frac{3}{4}a^2\right)\right]$$

(Second term has been reduced to lowest order.) The first term can be expanded for large r_c and rearranged by

$$\left[1+\frac{2}{r_c}(x\sin\theta+\zeta\sin\tau\cos\theta)+\frac{4}{r_c^2}(x\sin\theta+\zeta\sin\tau\cos\theta)^2-\frac{1}{r_c^2}\left(x^2+\zeta^2-\frac{a^2}{4}\right)\right]r_c^{-2}$$

Integrating over x from $-\frac{h}{2}$ to $\frac{h}{2}$ and over ζ from -w/2 to w/2,

$\int\cos\theta d\zeta dA_c = 2hw\,(1+C)\,\frac{a}{r_c}\sin\theta_a$, the small factor

$$C = -\frac{1}{8}\left(\frac{h}{r_c}\right)^2\cos^2\theta_a+\frac{1}{8}\left(\frac{w}{r_c}\right)^2\left[(2+\cos^2\theta_a)\sin^2\tau-1\right]-\frac{1}{8}\left(\frac{a}{r_c}\right)^2$$

Since C is of order 10^{-3}, it may be neglected. The effective slit angle is simply $\frac{a}{r_c}$ = 0.1 radian = 5.73°.

Intensity variations with respect to θ(plume transverse direction) will be neglected and a mean intensity as a function of the dip angle only is calculated. This intensity is the datum divided by $A_c\frac{a}{r_c}\cos\tau$ cm^2-rad, A_c = hw. Numerically, the divisor is 4.03225 x 10^{-2} cm^2-rad $\cos\tau$ or 2.31 cm^2-deg $\cos\tau$.